# An analysis of a deep-sea nodule mining system

## Vertical transportation by means of mechanical lifting

D.S. Kusters

8-5-2020

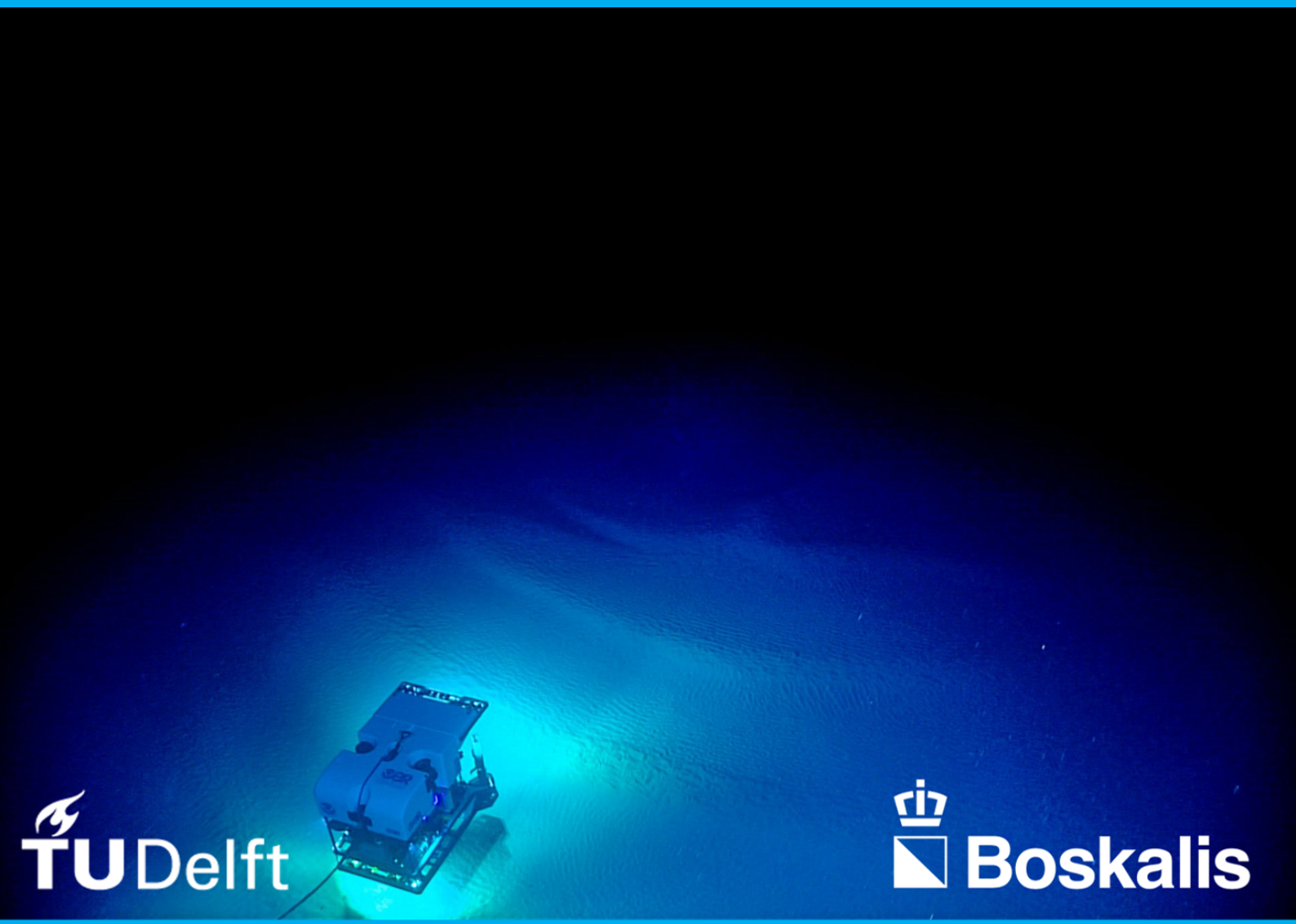

TU Delft

Boskalis

# An analysis of a deep-sea nodule mining system

## Vertical transportation by means of mechanical lifting

**by**

D.S. Kusters

in partial fulfilment of the requirements for the degree of

**Master of Science**
in Offshore and Dredging Engineering

at the Delft University of Technology,


| | | |
|---|---|---|
| Studentnumber: | 4245172 | |
| Date of publishment: | May 14, 2020 | |
| Thesis Committee: | Prof. dr. A. Metrikine | TU Delft, Chairman |
| | Ir. P.G.F. Sliggers | TU Delft, supervisor |
| | Dr. Ir. H. Hendrikse | TU Delft, supervisor |
| | Ir. R. van der Wal, | Boskalis, supervisor |


*This thesis is confidential and cannot be made public until December 31, 2025.*

TU Delft Delft University of Technology

# Abstract

Deep sea minerals can offer an additional resource to meet the increasing mineral demands, instigated by population growth and technological advancements. Deep sea minerals exist in various forms at the bottom of the ocean. In this research, polymetallic or manganese nodules are the kind that are of interest. The nodules are 1 to 12 cm large and contain a variety of minerals like copper, nickel and cobalt, but owe their name to its main component manganese. The region with the highest approximated resource of polymetallic nodules is the Clarion-Clipperton Zone (CCZ), situated in the Pacific Ocean between Hawaii and Mexico. The CCZ has water depth reaching 6000 meters, which is a significantly larger working depth than state-of-the-art deep sea projects within the offshore industry. These depths are accompanied by challenging environmental conditions exerted on the deep sea mining system.

A deep sea mining system typically consists out of three components: 1) Production Support Vessel (PSV), 2) Vertical Transport System (VTS) and 3) Seafloor Production Tool (SPT). The SPT harvests the nodules from the seabed, the VTS transports the mined nodules through the water column to the surface where they are transferred to the PSV. The focus in this thesis will be on the Vertical Transport System. Where most deep-sea mining developments are considering hydraulic vertical transport with a riser, Boskalis introduces a concept that utilizes mechanical lifting for the vertical transport. This allows for energy efficient transport, relative simplicity of concept and a maximization of the amount of power units above water.

The objective of this thesis is captured in the following research question: *What is the behaviour of the combined mining system (ropes, skip and SPT) during vertical transportation by means of mechanical lifting?* To answer this question, a wide overview is given of the deep-sea minerals that exist on the seafloor and the existing technologies to harvest them. Whilst the system is in principle relatively simple (just two containers (skips) that are alternatingly filled, hoisted to the surface, emptied and lowered again) many challenges arise. To identify these challenges, the system and the production cycle are discussed in detail. Literature research has been done to ensure realistic modelling of characteristics like structural damping of the rope, drag forces and added mass. The safe working load of steel wires is mostly consumed by its self-weight at a length of 4000 meters, making them unsuitable for deep-sea mining. Instead, the less common but naturally buoyant synthetic fibre rope is envisioned.

Many of the challenges in this deep-sea mining system originate from the environment as the system is subject to wave action and currents. Therefore, the current profile and wave spectrum typical for the Clarion-Clipperton Zone are obtained to serve as input for further investigation in the hydrodynamic analysis software Orcaflex. The system will be deployed over the entire 6000 m water column, causing the current but also the forward velocity of the system to possibly lead to high drag forces. A reduction of the forward velocity by introducing a new harvesting method is implemented, resulting in a large reduction of the drag forces and offset. The system consists of at least eight ropes, with two moving skips. Combined with the current and vessel motion, rope entanglement is a risk. A solution to prevent the rope entanglement is presented in this thesis. Possible occurrence of vortex-induced-vibrations (VIV) is identified and future research is recommended. The offset analysis shows that a large offset (500m) between the PSV and SPT results in relatively low horizontal forces on the harvester. The system is connected to the PSV, which is subjected to the Pierson-Moskowitz wave spectrum environment it is situated in, resulting in vessel motions. These motions will govern the dynamic behaviour of the system. The skips with attached fibre ropes have different eigenfrequencies on different water depths, as a longer rope will make for a softer system. This causes both skips, full and empty, to resonate in some regions. Consequently, the dynamic tension in the ropes is higher than the static tension, although it does not come forward as problematic. However, undesired slack rope conditions can occur when lowering the empty skip.

To conclude, an analysis of the deep-sea mining system has been done in which the eventual design has been modelled to the best extent currently possible. This research underlines the technical feasibility of this deep-sea mining concept. This research also evaluates the questions that have not been answered yet and recommends a variety of interesting research topics for the future.

# Preface

Doing a research project within the Research and Development department of a renowned company as Boskalis has been a very educational and interesting opportunity. Being able to do a research on the subject of deep-sea mining is a great finale of my Offshore and Dredging Engineering master. Therefore I would like to thank everyone within the Research and Development department, but special thanks goes out to Remmelt van der Wal for guiding me along this journey and providing me with insight, feedback and motivation. I would also like to thank Gertjan Grundlehner for letting me in on his concept. The weekly meetings with these two gentlemen were stimulating and enjoyable.
I would like to express my gratitude to my TU Delft supervisors Ir. Frank Sliggers and Dr. Ir. Hayo Hendrikse for being part of my graduation committee and for their helpful insights throughout this research. I would also like to thank them for their flexibility and solution-oriented mindset during these times that we are unable to meet in person.
I would like to thank my parents and Frank, Caroline & Joop for their hospitality during the last bits of my research. Last but not least, I would like to thank them, my girlfriend and my friends for the support, motivation and feedback I received during this project.

*D. S. Kusters*
*Oosterbeek, May 2020*

# Contents

# 1 Introduction

The global population is growing quickly with an estimated population of approximately ten billion by 2050[2]. This equals nearly 30 percent increase over the next 30 years. Moreover, technological advancements instigate a soaring mineral demand, as minerals are omnipresent in this developed world. Driven by these technological advances as well as demographic and economic growth the annual extraction of minerals and ores grew with a factor of 27 in the past century [75], as can be seen in Figure 1.1. This growth is expected to continue over the coming decades as the shift towards renewable low-carbon energy infrastructure puts even more pressure on mineral supply as solar panels, wind turbines and batteries all require high grade minerals[32]. Minerals are of great importance for our future civilization but as the rate of new discoveries is slowing down, mining them in an affordable way will soon be impossible. Each day extraction becomes more difficult and more expensive [66]. Terrestrial mining companies have to dig much deeper to obtain less and lower grade minerals, so yields plunge while waste increases. This puts a huge pressure on our communities and our environment [75]. We are in a situation that urges us to start considering viable alternatives. We are rapidly running out of affordable minerals while demand continues to grow exponentially and this scarcity leads to higher prices, leaving us with a huge challenge for the future [14]. How can the world meet an increasing metal demand in the most environmentally sustainable manner?

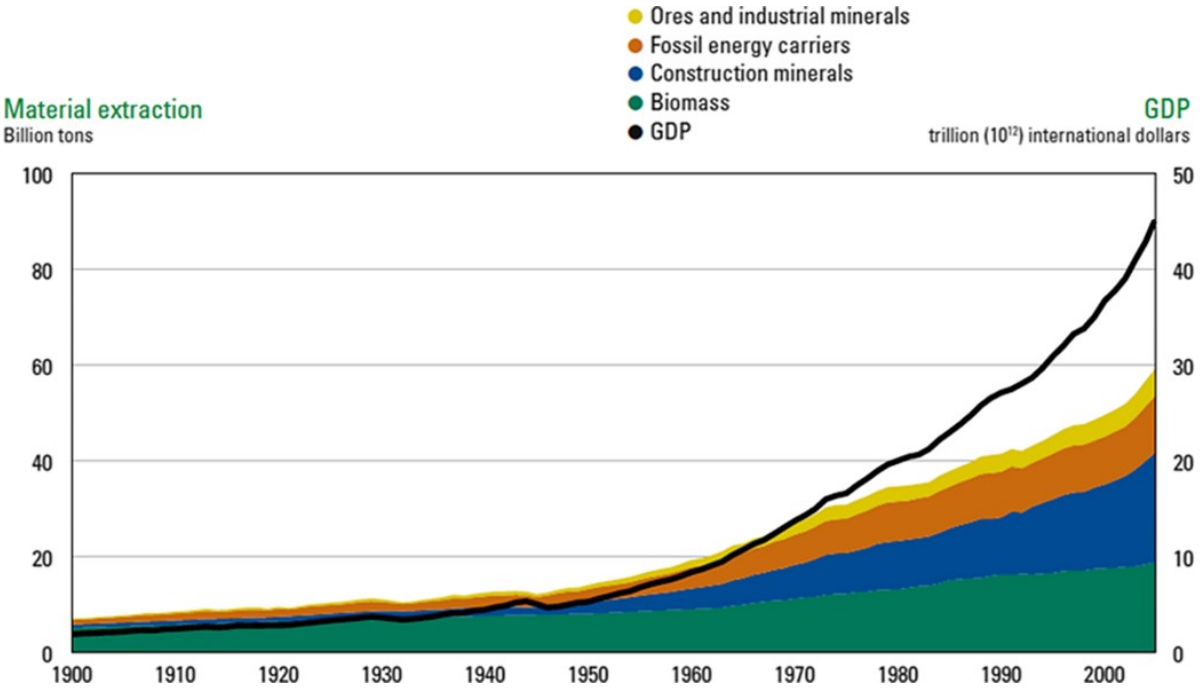


Figure 1.1: Global material extraction in billion tons, 1900–2005 [75]

## 1.1. Company Information

Boskalis has over 100 years of experience in hydraulic engineering, land reclamation and coastal protection. While the company roots are in the Netherlands, they operate in 90 countries and across six continents, with a fleet of more than 700 vessels and floating equipment. Dredging has traditionally been Boskalis' core activity, but today also a wide variety of maritime services and contracting to the offshore energy sector is offered. That includes the development, construction, transport, installation, repair, maintenance and decommissioning of oil and LNG import/export facilities, offshore platforms, pipelines, cables and offshore wind parks. In 2010 SMIT joined Boskalis, including towage services, emergency response and salvage in Boskalis' operations. Their widespread knowledge in combination with their innovative mindset makes that they can and will look into new markets.


## 1.2. Deep-Sea Mining

One of these new markets that Boskalis is looking into is deep-sea mining. The rich presence of resources at the bottom of the sea are known for more than a century, due to an expedition of the *HMS Challenger* between 1872 and 1876 [54]. During this expedition, vast volumes of nodules were recovered from the Pacific, Indian an Atlantic Oceans. A chemist that was present at the expedition noted correctly that the nodules were composed of mostly manganese, explaining the common name *manganese nodules*. The results from the HMS expedition remained the most significant research in the deep-sea resources field for many years. When the metals prices rose in the 1960's, interest sparked and systematic studies of not only the manganese nodules, but also the other deep-sea resources as crusts and seafloor massive sulfides, commenced. John Mero predicted large resources of nodules containing economical interesting minerals. This encouraged several private and government efforts to explore the most promising area, the Clarion-Clipperton zone in the Pacific Ocean. Some of these efforts successfully tested small-scale deep-sea mining systems, but none of them resulted in economical favourable mining operations. Figure 1.2 gives an overview of the different deep-sea resources; (1) Cobalt crusts, (2) Seafloor massive sulfides, (3) Polymetallic (or manganese) nodules. These will be discussed in more detail in Chapter 2. For now, Boskalis' focus is solely on the recovery of polymetallic nodules and therefore the cobalt crust and seafloor massive sulfides recovery will not be within the scope of this thesis. Contemporary terrestrial mining is under pressure due to depleting reserves, an increasing demand due to population growth and technological advancement and harsh working conditions in the mines. This initiated a renewed interest in deep-sea mining by several governments, companies and research institutes. Up to this date no ongoing operations are present, but there is ongoing research and developments [31] [13], from which this thesis is an example.

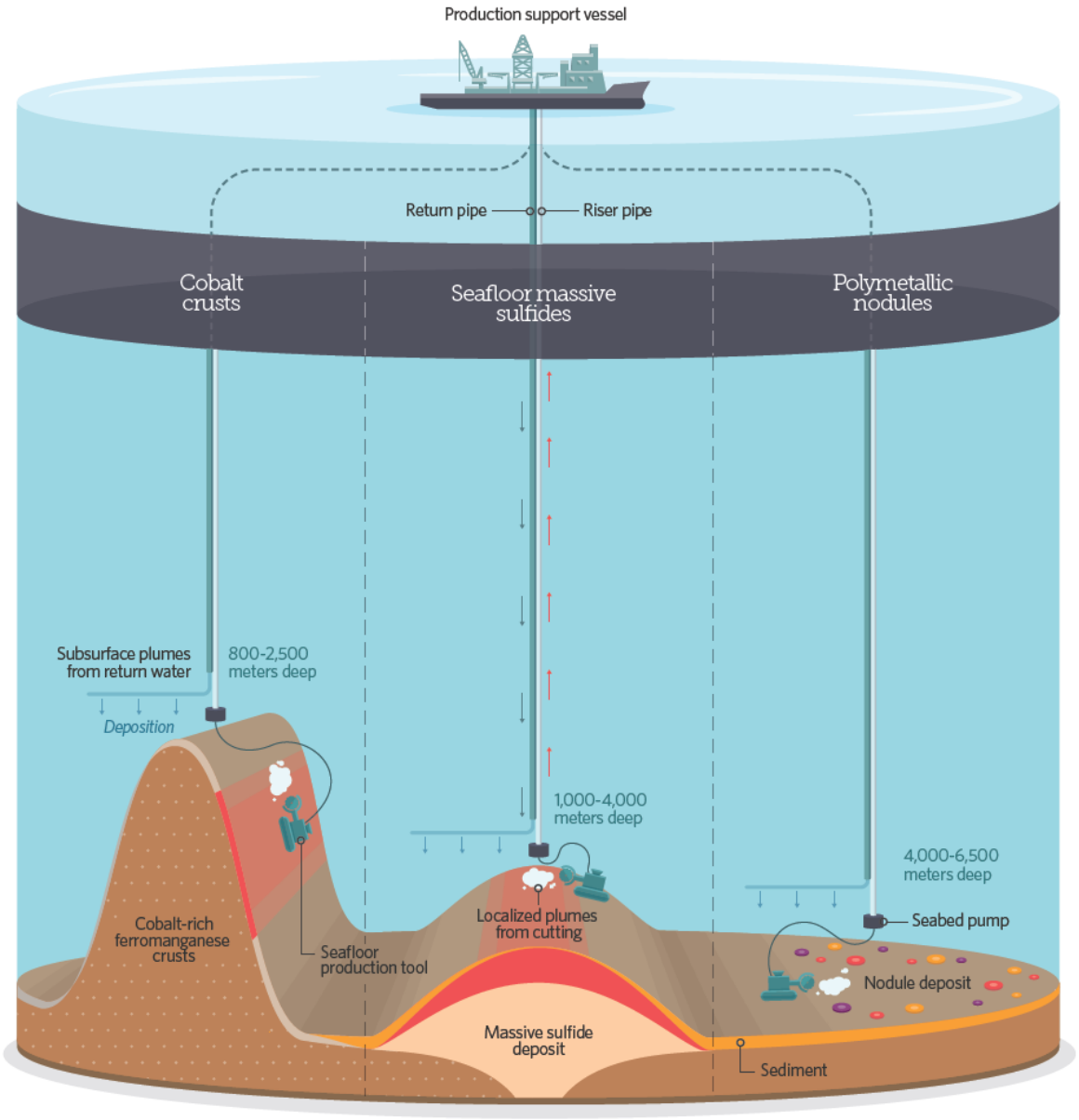


Figure 1.2: Types of Deep Sea Mining [4]

## 1.3. Problem definition

The deep-sea resource of interest, the polymetallic nodules, are located at the seabed at a depth of 4000 - 6000 meters. These are extremely deep waters, which results in challenging conditions with regards to the collection of the nodules and especially the vertical transportation of the collected resources. This thesis focuses on the vertical transportation by means of mechanical lifting. Boskalis has come up with a concept around its ideas for the recovery of the nodules, which is driven by proven concepts, energy efficiency and simplicity. Vertical transportation by means of mechanical lifting has the advantage of the crucial (power) components being at the vessel instead of subsurface. The concept consists of a Production Support Vessel (PSV) which lowers the Vertical Transport System (VTS) and the Seafloor Production Tool (SPT) when arriving at the mining location. The SPT is responsible for the collection of the nodules and the VTS transport the collected nodules to the PSV. The VTS consists of two skips, that are each lifted by two hoisting wires. The skips will have guiding structures attached, through which the guidance wires run. These guidance wires are used to lift the docking unit (which is part of the SPT) above the seabed. The skips alternatively make a round trip to the PSV. While one skip is being filled, the other is lifted to the surface to be emptied at the vessel, where after

the empty skip travels back down to be filled again. The extreme depth and the environmental loads acting on the system will raise challenges. The expected load mechanisms are shown in Figure 1.3(b). The loading of the VTS is divided into dynamic and static loading. The static loading is due to the mining equipment that is suspended from the vessel by the VTS. The relative current is the velocity of the seawater with respect to the ropes, divided in current and forward velocity of the system. As the system will be deployed over the entire 6000 meter depth, the relative current is expected to significantly influence the system. The drag force on the system can result in high horizontal forces on the harvester, resulting in the loss of traction of the harvester. Offset is the horizontal position difference between the suspension points of the top of the ropes and at the docking unit. Changing the offset will have consequences for the loading of the system. In Figure 1.3(b) this is identified as static loading, whereas the loading due to changing offset can also become dynamic. The dynamic loading occurs due to the motion of the vessel in the waves and the transportation of the skip. The vessel motions will results in a heave motion of the top of the ropes, which can lead to high excitations of the skip while being transported or when it is at the seabed. Besides the skips, the SPT is also connected to the vessel and subjected to its motions. Consequently, undesired motions of the SPT can occur. The vertical transportation of the skips will cause interaction forces between the eyelets of the skips and the guidance wires. This might results in wear of the ropes and fatigue damage. Vortex Induced Vibration (VIV) can occur if the system meets the right requirements. They can lead to fatigue damage and an increase in the drag coefficient. The objective of this thesis is to analyse the these static and dynamic configurations, the interaction between the PSV, VTS and the SPT, the design criteria for the ropes and potential showstoppers. To be able to adequately model the sytem, the correct characteristics need to be determined.

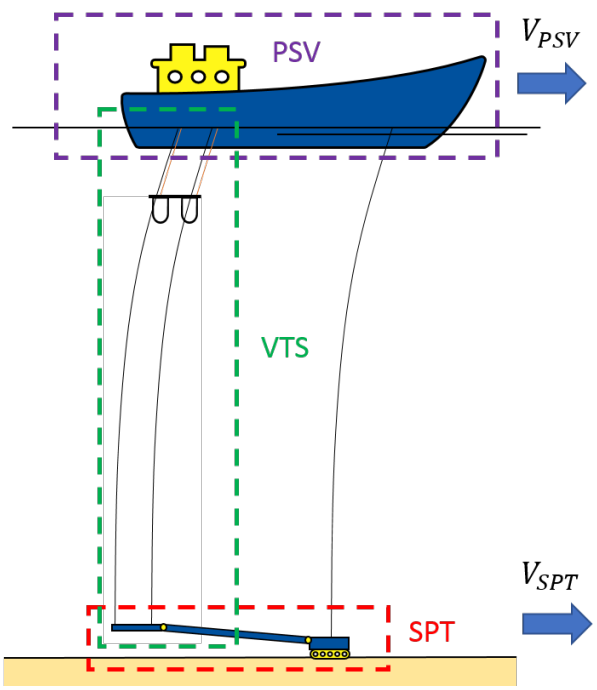


(a) Subsystems of the deep-sea mining concept

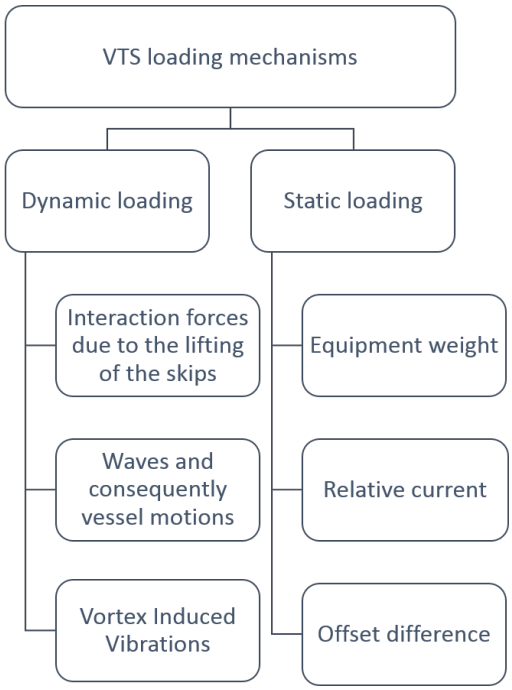


(b) VTS Loading Mechanisms

## 1.4. Research questions

The thesis addresses the following main research question which is supported by the sub-questions given below.

### Main research question

*What is the behaviour of the combined mining system (ropes, skip and collector) during vertical transportation by means of mechanical lifting?*

**Sub-questions**

The main research question is supported by the following sub-questions:

- How sensitive is the system to currents?
- What will be the horizontal force on the guidance wire by the eye of skid due to the difference in offset of the skid relative to the support frame during the vertical transport?
- Will the hoisting and guidance wires clash at any point in the lifting cycle?
- What will be the required resistance of the collector to maintain it's position, due to forces on the whole system?
- What are the boundary conditions for using synthetic wires instead of steel wires?
- What is the result of lowering the forward velocity from 1 m/s to 0.1 m/s?
- To what extent will the vessel motion influence the nodule collection and transportation?

## 1.5. Scope of Work

Deep-sea nodule mining by means of mechanical lifting is a broad subject, where many different problems arise. The main focus of the study is concentrated on the Vertical Transport System. An attempt will be made to give a broad overview of this system and a more detailed look into the behaviour of the ropes, skips and the docking unit. The CCZ where operations will take place has a water depth up t o6000 meters. Current and the forward velocity of the system will exert drag forces on the system. Vessel motion will introduce dynamics to the system. The characteristics of the components of the system, such as damping, (added) mass and the drag coefficient have an influence of the behaviour due to these environmental forces. A good understanding of these characteristics is relevant to realistically simulate the system in Orcaflex. The desired outcome of this thesis is a preliminary look into the behaviour of the system and the expected forces that will be exerted on it.

## 1.6. Report Structure

In order to structure the problem multiple objectives have been set up. These objectives are captured in the chapters of this report, as can be seen below.

- **Chapter 2:** *Describe the currently known deep-sea resources and deep-sea mining technology*
  In chapter 2, a general introduction is given to the subject of deep-sea mining, the resources, the possible environmental consequences etc. in order to give the reader the necessary background knowledge. Also, an insight is given in the existing technologies.
- **Chapter 3:** *Introduces the vertical transport by means of mechanical lifting system*
  The proposed technology is introduced, combined with the production cycle and a general overview of the deep-sea mining system.
- **Chapter 4:** *Assess the main parameters of the deep-sea mining system*
  The environmental data is analysed in chapter 4 and a more detailed assessment of the deep-sea mining system in done in chapter 5. All the important parameters are discussed. Necessary theory is elaborated to support the choices that are made.
- **Chapter 5:** *Provide the theoretical background of the system characteristics*
  To correctly model the deep-sea mining system the realistic characteristics need to be determined. These characteristics are for example the drag coefficient, added mass, submerged weight, damping parameters, synthetic fibre rope specifications etc.
- **Chapter 6:** *Introduce Orcaflex and discuss how the different components are modelled*
  The obtained parameters of the mining system are used as input for an Orcaflex model. Orcaflex is a widely used hydrodynamic analysis of offshore marine systems software and is a suitable tool to model motions and forces in this deep-sea mining system.
- **Chapter 7:** *Model the system and analyze the behaviour and the loads*
  Separate components are modelled and investigated to give more insight in individual aspects, but also the whole system is modelled together to assess the interaction between different components. The results of the model are studied and analysed. The outcome of the analysis is discussed in this section and forms the foundation for the conclusions drawn.
- **Chapter 8:** *Conclusions and recommendations*

# 2
# Deep-Sea minerals

The deep sea is considered to start at the shelf break at a depth of about 200 m, where an obvious change of fauna is noticed[67]. This part of the ocean is the single largest ecosystem on the planet. The surface of the sea covers 70 % of the earth's surface. Moreover, 50% of the earth's surface is occupied by ocean with depths over 3000 m, having a mean depth of 3800 m and a maximum depth of 10,924 m in the Mariana Trench. This vast remoteness and the challenges that accompany this have resulted in the deep sea being one of the least studied and therefore understood environment on earth. Sparked by the debate whether life occurred below depths of 300 m, the exploration of the deep-sea started a little over 150 years ago [67]. Already in 1873 the HMS Challenger discovered the existence of valuable resources in these waters, as their dredge hauled up "several peculiar black oval bodies which were composed of almost pure manganese oxide". The real research of the possibility of economical feasibility of deep-sea mining started after J.L. Mero published his book *Mineral Resources of the Sea* [48] in 1965. In his book, he described a nearly inexhaustible resource of minerals such as manganese, copper, nickle and cobalt lying on the bottom of the Pacific Ocean. This, and the prognosis that the global mineral stock would be exhausted, spiked the interested in deep-sea mining in the 80's and many research cruises were performed in these years. Eventually none of which resulted in a return of investment that would make the deep-sea mining business one to stay. This research provided us better insight into the amount and characteristics of the marine mineral resources. In recent years the interest to explore the deep sea has accelerated and this thesis is an example of this matter. In this chapter it is discussed what kind of deep-sea minerals there are, where they can be found, who owns them and what should be taken into consideration when mining it.

## 2.1. Types of marine minerals resources

There are various types of marine mineral resources, which differ in habitat type and composition. The three main types that are of commercial interest are ferromanganese (FeMn) or cobalt-rich crusts that are found on the sides and summits of seamounts (underwater mountains), seafloor massive sulfides (SMS) which arise around hydrothermal vents and manganese nodules on the vast abyssal plains. These different types of marine mineral resources can be seen with some of their different characteristics in Figure 1.2.

**Ferromanganese crusts**

Ferromanganese crusts are formed by the precipitation of iron-manganese oxides from seawater onto the surface of nearly all rock surfaces in the deep-sea, under the condition that they are kept free from sediment, due to currents, for millions of years. Crusts have a very slow growth rate of between 1 and 10 mm per a million years. Eventually this leads to a crust between 1 and 25 cm thick, covering the rock. The harvesting of the crust would involve separating the cobalt-rich layer of the less valuable rock beneath it [60]. The ferromanganese crusts are typically found between 400-7000 m water depth, but with the richest deposits found at depths of 800 - 2500 m, mostly as crusts of seamounts in the west Pacific[63]. A location has to meet the following requirements to be prospective of formation of ferromanganese crusts: Presence of seamounts with peaks between the 800-2500 m in an area that is older than 10 million years old. The sediment rates must be lower than 2 cm per 1000 years. The locations that meet these requirements are shown in Figure 2.1 A. These requirements are mostly met in the "Prime Crust Zone" (PCZ), which is shown in Figure 2.1 B, making this the location with the greatest economical potential. The International Seabed Authority has a database of ferromanganese samples from different locations, as shown in Figure 2.1 C. The resources that are estimated to be available in the PCZ are shown in Figure 2.6.

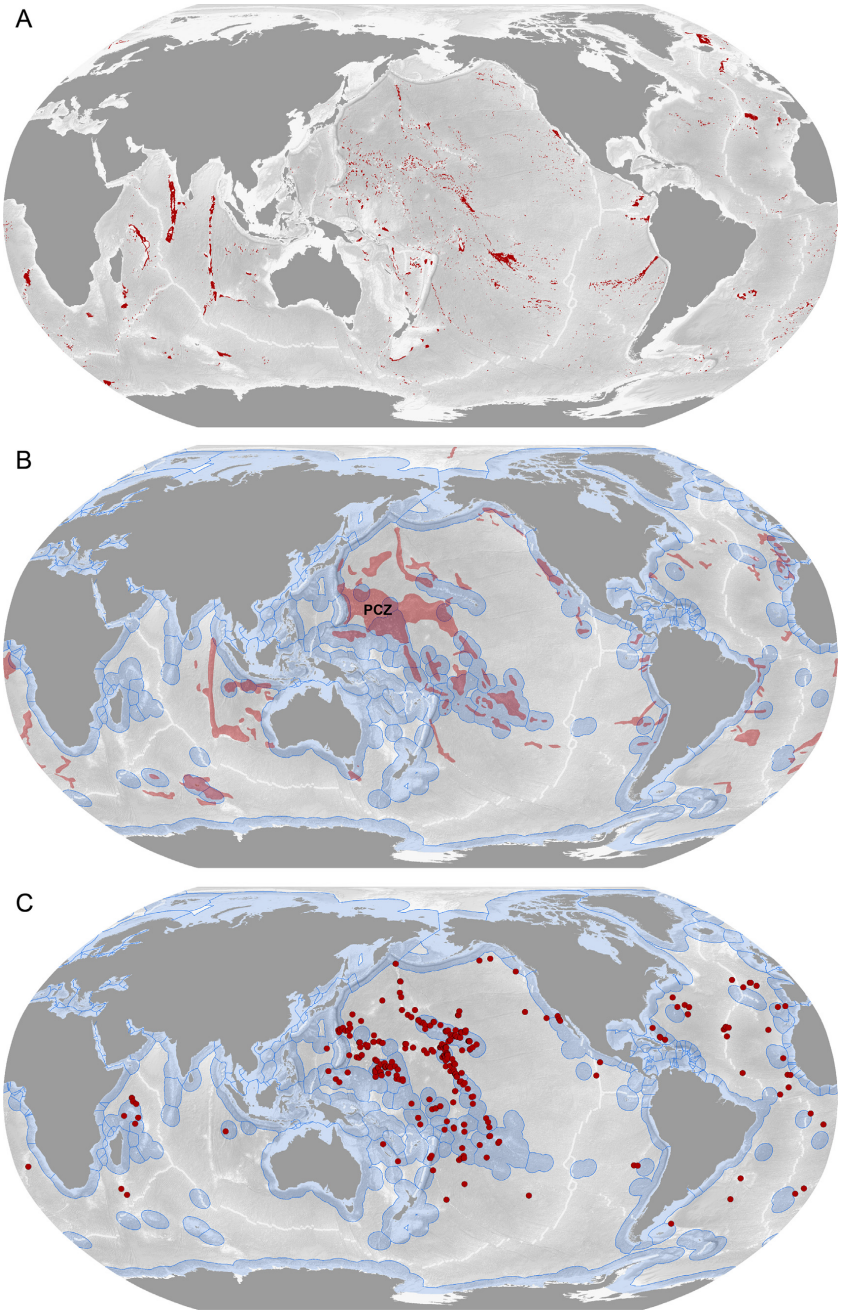


Figure 2.1: Ferromanganese crusts locations of interest [63]

### Seafloor Massive Sulfides

Polymetallic sulfides or seafloor massive sulfides (SMS) deposits are formed by mineral-rich, high-temperature hydrothermal fluids emitted by underwater volcanoes, mostly around tectonic plate boundaries. The deposits form due to this super heated solution cooling down because of the interaction with the surrounding seawater. The cold seawater will flow in cracks that can reach depths of several kilometers into the seafloor. In these cracks, the water is heated to temperatures up to 400 degrees Celsius. This high temperatures instigate chemical reactions, causing the fluid to be enriched with dissolved metal and sulfur from the surrounding rock. This hot, mineral-rich mixture has a lower density causing it to rapidly rise to the seafloor. Here it "erupts" out of the seafloor, creating chimney-like vents, were the cooled mineral precipitate at the vent site. Precipitating minerals creating a black "smoke" cause the common name "black smokers". These eruptions form very rich, but very local deposits. Figure 2.2 A shows the tectonic plate boundaries that are important for the formation of seafloor massive sulfides. The colors of the boundaries denote the rate at which the

segments spread, which ranges from < 20mm/yr for the dark blue to > 140mm/yr for red. Figure 2.2 B shows the locations of high-temperature hydrothermal systems that are responsible for the mineral deposition on the seabed. Despite the harsh conditions the hydrothermal vents are located at, high pressure due to depths between 1000-4000 m, temperatures up to 400°C and high acidity (Ph 2-3), they accommodate vast communities of organisms. They adapted to these conditions and can be found nowhere else on Earth. It is even believed by some researches that life on Earth originated at the hydrothermal vents [44]. The harvesting of the seafloor massive sulfides chimneys could require the breakdown of these extraordinary habitats. There are many people and organisations that urge the industry to take responsibility to take the time to do sufficient research [5] [19]. The environmental impact will be further discussed in Section 2.3.

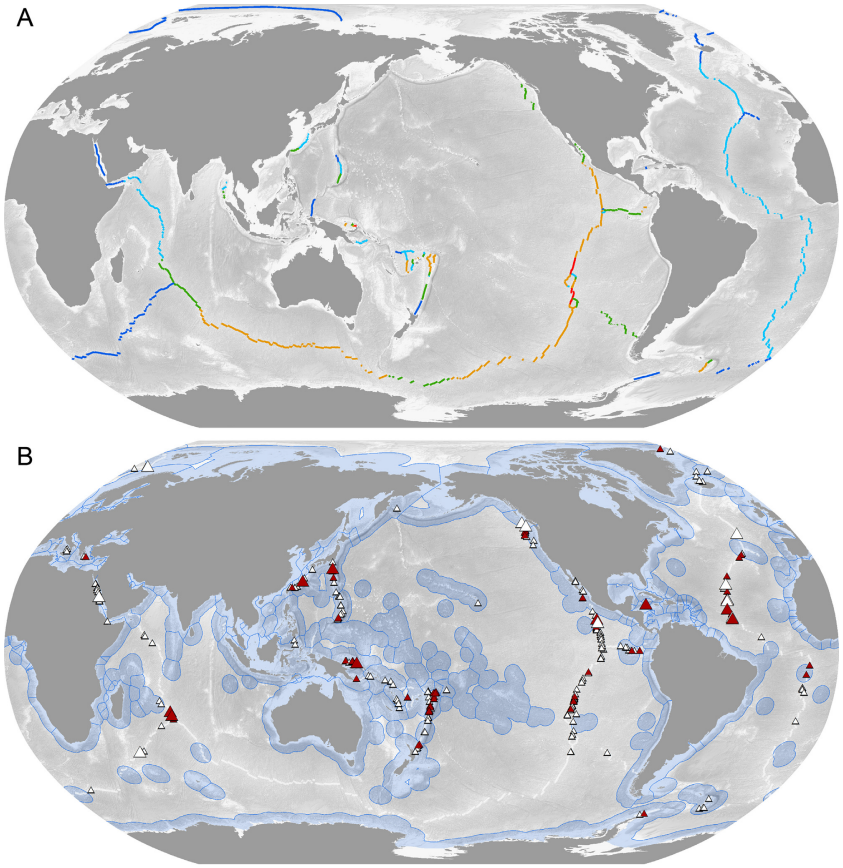


Figure 2.2: Seafloor Massive Sulfides locations of interest [63]

### Polymetallic nodules

The last resource of marine minerals that is discussed in this chapter is the polymetallic or manganese nodule (named after its main constituent). Compared to the other two, this resource is relatively "up for grabs", except from the fact that they occur at depths of approximately 3500 m to 6000 m, mostly on the surface of sediment-covered abyssal plains. A picture of a Clarion-Clipperton zone' seabed littered with nodules is shown in Figure 2.3(a). The nodules are "potato-sized", ranging from a diameter of 1 cm to 12 cm and can be seen in Figure 2.3(b). As stated, their main constituent is the metal manganese (and also iron), but the main metals of economic interest are their other components like nickel, copper, titanium and cobalt. The partition of the components in recovered nodules can be found in table 2.1.

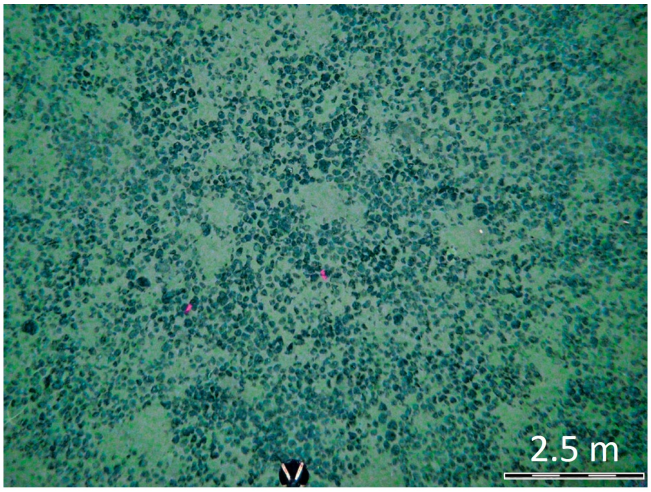


(a) Nodules on the Clarion-Clipperton sea floor

(b) Polymetallic nodule, Charles D. Winters/NatureSource/Agentur Focus

Figure 2.3: Polymetallic Nodules

The polymetallic nodules form, as illustrated in Figure 2.4, in two different ways [33]:

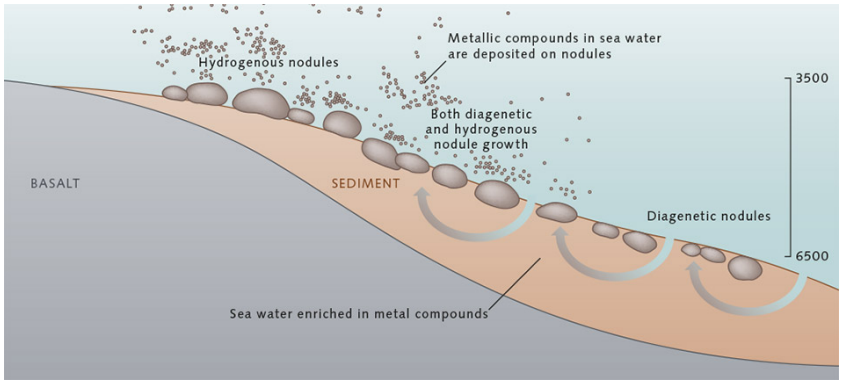


Figure 2.4: Formation of polymetallic nodules by hydrogenetic and diagenetic growth [2]

- Hydrogenetic growth: minerals participate from the ambient seawater. The metals are concentrated in the water column by adsorption to Fe and Mn-oxides due to differences in surfaces charge. Mn-oxide particles, having a negative surface charge, attract positively charged ions such as Cu, Ni and Co. On the other hand, the slightly positively surface charged Fe-oxide particles attract other, negatively charged, ions such as Mo, V, As. This is an extremely slow growth rate of about 1-10 mm per million years.
- Diagenetic growth: a process were the minerals precipitate from pore waters within the sediment. The seawater penetrates these pores and is modified by chemical reactions within the sediment, only to become enriched with metal compounds. These metal compounds are then precipitated on the the nodules. Diagenetic growth rate is low, but faster than hydrogenetic growth with 10 - 100 mm per million years.

Almost all nodules form by a combination of hydrogenetic and diagenetic growth, whereby the influence of each process is different depending on the marine environment. The extremely slow growth rate means that the polymetallic nodules can only grow in areas where the environmental conditions are stable long enough for it to grow a couple of centimeters (which is several million years for an averaged sized polymetallic nodule). Due to this the formation of the nodules is affected by the following environmental factors:

- Slow sedimentation rates. The nodules would be covered if the sedimentation rate is too high. Areas with

sedimentation rate of more than 1 cm per a thousand years are excluded from exploration with regards to deep-sea mining.

- Constant flow of water over the seabed. It should remove sedimentation that would cover the forming nodules over time, but leave behind sufficient materials to act as nuclei for new nodules. It should also provide a sufficient amount of oxygen, which is requisite for the formation of manganese oxide compounds.
- The presence of ground-dwelling organisms is also said to be of importance[63]. They make sure the nodules are constantly pushed up to the seabed surface and create enough movement in the soil to make the diagenetic growth possible.
- A semi-liquid (aqueous) sediment bottom layer. For diagenetic growth, plentiful pore water must be present in the soil.

The factors are met at many places on the seafloor. Figure 2.5 A shows the locations that posses the properties to form polymetallic nodules as stated above. The locations that posses these properties do not automatically enlist as a promising location. The areas with the highest potential are shown in Figure 2.5 B. One of these areas is the Clarion-Clipperton Zone (CCZ), the location of interest of this concept and further introduced in Section 2.2. In this figure the light blue areas highlight the Exclusive Economic Zones (EEZ's). On different places samples have been taken. Figure 2.5 C shows the locations from which the samples had a cobalt weight percentage of 0.5 or more.

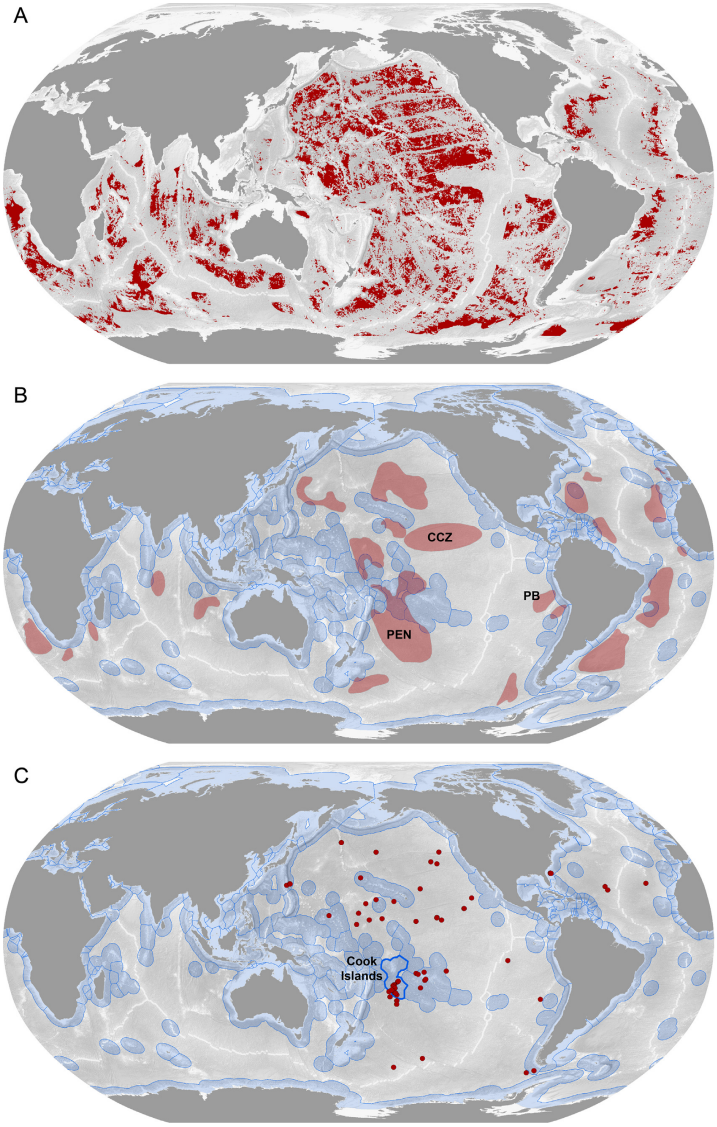


Figure 2.5: Polymetallic nodules locations of interest [63]

## 2.2. Location of interest

The requirements as stated in Section 2.1 are met in several places in the world, but the greatest concentrations of polymetallic nodules have been discovered in the Clarion-Clipperton Zone (CCZ), stretching from Hawaii to the west coast of Mexico, bordered by the Clarion fracture in the north and by the Clipperton fracture in the south, as can be seen in Figure 2.5. In the CCZ, the Antarctic Bottom Water is flowing over the seabed, provides the needed oxygen and the sufficient removal of the sediment.
The CCZ includes an area of 4.2 million $km^2$ of economic interest, with an (conservative) estimated total mass of polymetallic nodules of 21 billion tonnes [38], which yields nearly 6000 million tonnes of manganese. This means that there is more manganese on the seafloor of the CCZ, than on the entire known land-based reserves. This doesn't only hold for the manganese, but also the amount of nickel and cobalt in the nodules is bigger than their related land-based reserve. A comparison of more elements, present in the nodules, with their land-based reserves can be seen in 2.6.

Contained metal tonnages ($\times 10^6$ tonnes).[a]

| | Clarion-Clipperton Zone Nodules [b] | Global Terrestrial Reserve Base [c] | Global Terrestrial Reserves [c] | Prime Crust Zone [b] |
|---|---|---|---|---|
| Manganese | 5,992 | 5,200 | 630 | 1714 |
| Copper | 226 | 1,000+ | 690 | 7.4 |
| Titanium | 67 | 899 | 414 | 88 |
| TREO [d] | 15 | 150 | 110 | 16 |
| Nickel | 274 | 150 | 80 | 32 |
| Vanadium | 9.4 | 38 | 14 | 4.8 |
| Molybdenum | 12 | 19 | 10 | 3.5 |
| Lithium | 2.8 | 14 | 13 | 0.02 |
| Cobalt | 44 | 13 | 7.5 | 50 |
| Tungsten | 1.3 | 6.3 | 3.1 | 0.67 |
| Niobium | 0.46 | 3.0 | 3.0 | 0.40 |
| Arsenic | 1.4 | 1.6 | 1.0 | 2.9 |
| Thorium | 0.32 | 1.2 | 1.2 | 0.09 |
| Bismuth | 0.18 | 0.7 | 0.3 | 0.32 |
| Yttrium | 2.0 | 0.5 | 0.5 | 1.7 |
| PGM [e] | 0.003 | 0.08 | 0.07 | 0.004 |
| Tellurium | 0.08 | 0.05 | 0.02 | 0.45 |
| Thallium | 4.2 | 0.0007 | 0.0004 | 1.2 |

[a] Metals highlighted in red are those with greater tonnages than terrestrial reserves or terrestrial reserve bases.
[b] Nodule tonnage used is 21,100 million dry tonnes and crust tonnage used is 7533 million dry tonnes (from Hein and Koschinsky, 2013).
[c] USGS 2009 reserve base & 2012 reserves (reserve base includes those resources that are currently economic (reserves), marginally economic, and subeconomic).
[d] Total Rare Earth Elements as Oxides.
[e] Total Platinum Group Metals.

Figure 2.6: Deep sea resource comparison with the land-based resource [32]

| **Parameters** | **Small (2-4 cm)** | **Medium (4-6 cm)** | **Large (6-8 cm)** | **Very large (>8 cm)** |
|---|---|---|---|---|
| **Wet density (te / m^3)** | 2.04 | 1.98 | 1.90 | 1.84 |
| **Dry density (te / m^3)** | 1.41 | 1.35 | 1.28 | 1.26 |
| **Porosity (%)** | 63.03 | 63.01 | 61.50 | 57.90 |
| **Mn (%)** | 22.94 | 23.97 | 23.82 | 29.63 |
| **Fe (%)** | 9.33 | 8.59 | 9.10 | 6.65 |
| **Ni (%)** | 0.86 | 1.22 | 0.99 | 0.53 |
| **Cu (%)** | 0.87 | 1.06 | 0.90 | 1.27 |

Table 2.1: Variation in physical and chemical properties of nodules with size [52]

In research from 2000, when 6706 nodules were recovered and researched [20], the median min-

imum, middle and maximum nodule dimensions were found to be 4, 6 and 8 cm respectively. However, polymetallic nodules smaller than 2 cm were not taken into account for this research. The density of the nodules in this area can be as much as 75 kg per $m^2$, but is more commonly around the 15 kg per $m^2$. The different sized nodules have been investigated in another research [52]. The dry and wet densities, the porosity and its components are stated in table 2.1

### Seabed Characteristics

The seabed can be divided into multiple layers. The top layer (that is about 10 cm thick) is a semi-liquid sediment type (almost as thin as water). As stated in 2.1 this semi-liquid sediment is of importance for the diagenetic growth of the nodules. However, below this top layer, a sediment type of cohesive soil with a constant strength can be found [6]. Research with regards to the specific density has been done in 2009 in the IOM exploration zone within the Clarion-Clipperton Zone [26]. On board of the ship laboratory the characteristics of the sediment have been determined. The specific density of the different encountered sediment types have been researched and computed. It showed that the density of the top layer is around the density of seawater. A seabed sample can be found in Figure 2.7, showing the semi-liquid top layer (1) and the cohesive soil layer (2) underneath. From research [6] it has been suggested that the shear strength ranges between the 0 and 7.4 kPa with an optimal design parameter of about 2.5 kPa.

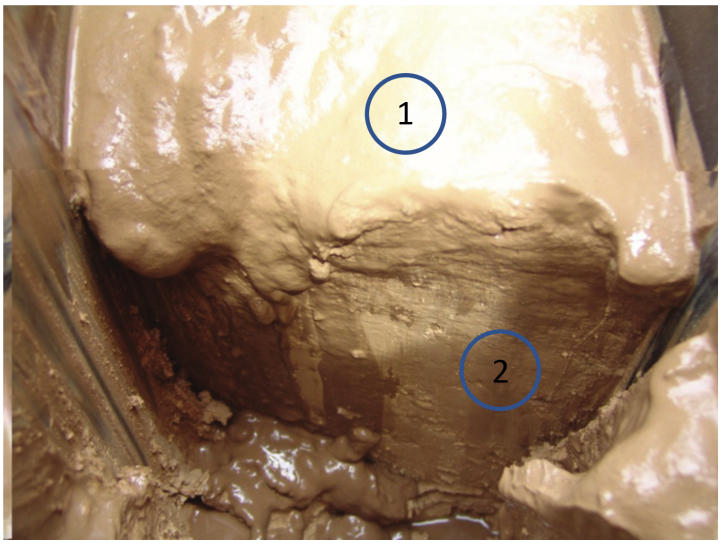


Figure 2.7: Deep-sea sediment with liquid consistencies at the top layer [26]

### International Seabed Authority

The sea and who it belongs to has been a subject of discussion for many of years. One year after Christopher Columbus set foot in America, on the 4th of May 1493, Pope Alexander VI divided the Atlantic Ocean between Spain and Portugal, the two maritime superpowers of the era, with the papal bull *Inter caetera* [65]. Everything west of the pole-to-pole line 100 leagues west belonged to Spain and the east belonged to Portugal.

Since then organizations and governments have consistently implemented laws regulating the use of the sea and everything in and underneath it. From 1973 to 1982, the *United Nations Convention on the Law of the Sea*, was held in New York and Geneva. Representatives of more than 160 sovereign states sat down and discussed the challenges that arose around the looming conflict that could devastate the oceans, urged on this subject by Malta's Ambassador to the United Nations, Arvid Pardo [76]. After the convention, a treaty was signed to ban all nuclear weapons on the seabed, it was determined that all resources behind the national borders are common heritage on mankind and the Exclusive Economical Zones (EEZ) were brought to life. The EEZ determines that coastal countries have the jurisdiction over all the resources; oil, gas, fish, sand and also deep-sea minerals, found in the waters, on or in the seabed within 200 nautical miles from its shore. The different maritime zones can be seen in Figure 2.2.

| Maritime Zones | Distance from Coast (nm) | Complete Rights for Resources by Country |
|---|---|---|
| Coastal water | 0-3 | Airspace, water column, seabed, subseabed |
| Territorial sea | 3-12 | Airspace, water column, seabed, subseabed |
| Contiguous zone | 12-24 | Airspace, water column, seabed, subseabed |
| Exclusive economic zone | 24-200 | Water column, seabed, subseabed |
| Extended continental shelf | 200 - maximum 350 | Seabed, subseabed |
| International Water | >200 and 350 | No rights |

Table 2.2: Maritime Zones - Rights and Responsibilities [53]

Following the need *"To address certain difficulties with the seabed mining provisions contained in Part XI of the Convention"*, the International Seabed Authority (ISA) was established in 1994 [76], after some years of preparatory meetings. It is an autonomous intergovernmental body with 167 members, that organizes and controls the activities in the regions that are outside of the Exclusive Economical Zones and therefore are beyond national jurisdiction. The ISA has approved thirty 15-years exploration contracts, where of sixteen for the exploration of polymetallic nodules in the CCZ. The Clarion-Clipperton Zone and the exploration area's for polymetallic nodules as determined by the ISA can be seen in Figure 2.8.

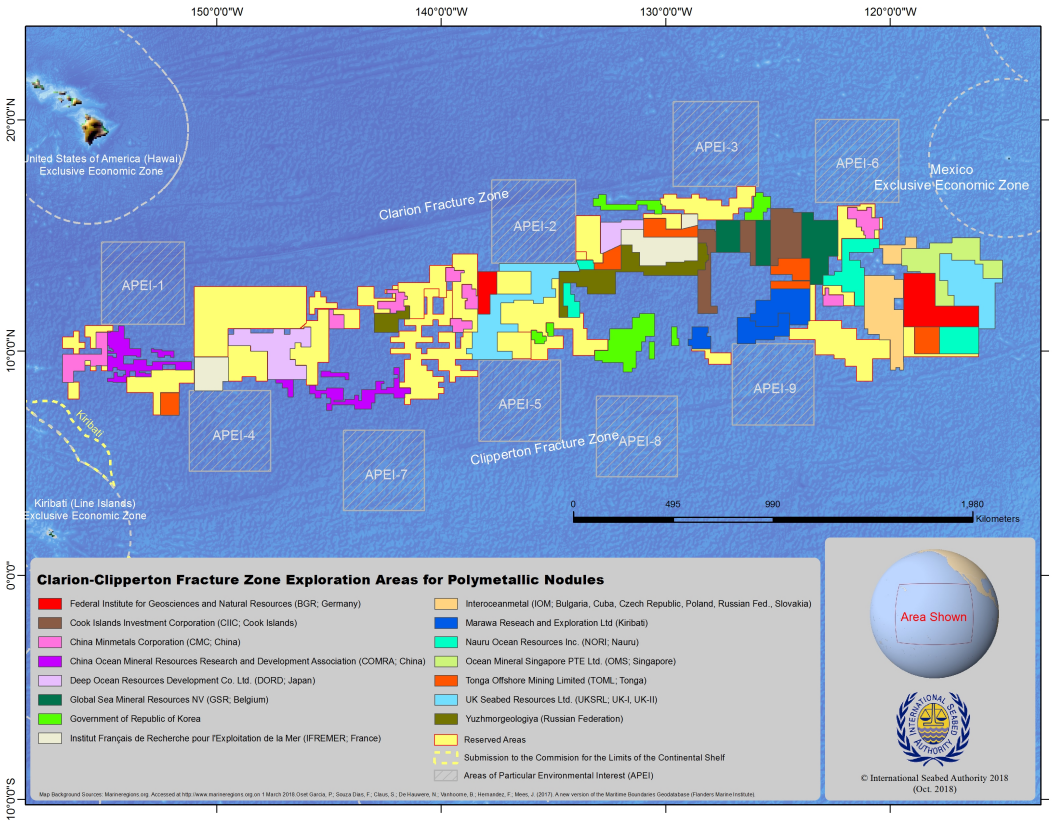


Figure 2.8: Clarion-Clipperton Zone [37]

## 2.3. Deep-Sea Mining and the Environment

*"While we can predict some of the environmental impacts of seabed mining, much remains unknown and untested. We remain largely ignorant of how deep-ocean ecosystems change in response to human activities and natural variations, and of the consequences of these changes. It is reasonable to assume that recovery periods are likely to be decades long, and that at least in localized areas, these ecosystems may never recover."*
– Then ISA Deputy Secretary-General Michael Lodge[49]

When touching upon the subject of deep-sea mining, it would be troublesome if one did not mention the environmental impact it might possibly have. This section will discuss the possible damage that will be done to the deep-sea environment, the lack of knowledge and the APEI's, ISA's way to mitigate the risks.

### Environmental Impact

As stated before, polymetallic nodules take millions of years to form. When the nodules are removed, it is unknown if the corresponding marine fauna will return. Several experiments have been done regarding the impact of deep-sea nodule mining on the CCZ environment [51], showing highly variable results. In 2004, for example, an experimental nodule extraction site was visited after 26 years, to assess the recovery of the area [50]. The tracks of the mining vehicle were still very well visible and, compared to the neighbouring, undisturbed areas, there was less diversity and biomass of nematode worms. The almost unchanged imprint of the mining vehicle is expected due to the same requirement needed for the formation of the polymetallic nodules, which is a low sedimentation rate.
Other experiments [73] investigated the biodiversity of megafauna associated with the polymetallic nodules in the CCZ by studying more than 50 hours of video footage and 200,000 photographs. They concluded that the polymetallic nodule ecosystem is an unique environment and habitat. Some examples of the fascinating animals that live at the CCZ seabed can be seen in Figure 2.9


(a) Glass sponge (b) Psychropotes Semperiana

Figure 2.9: Clarion-Clipperton benthopelagic fauna, with the polymetallic nodules in the background [71]

The marine life can be separated into two groups, the pelagic and benthopelagic biota [15]. Benthopelagic biota are the bottom-dependent animals living in the water layer just above the sea floor, like the earlier described nematode worms. This group is directly impacted by deep-sea mining activity, as their natural habitat will be disturbed and doesn't have the short term capability to restore [50] [71]. The pelagic biota consists of all living in the water column and will also be impacted due to the discharge of surplus sediment and by the generation of operational sediment plumes [51]. The understanding, forecasting and modelling of the behaviour of these plumes is a different subject on its own and their influence must be researched further before commercial mining will be possible [42].

Deep-sea mining will include remotely operated machinery on the seabed, increasing the underwater ambient noise. The offshore wind sector has done research on the underwater noise level due to the installation of wind turbines and the effect on marine mammals [10]. Following this research, governments require a maximum noise level induced during installation. The same can be expected for the deep-sea mining industry. Deep-sea mining is expected to operate continuously and it is certain that this will add up to the ambient noise. But, as with many possible impacts of deep-sea mining, precise noise characteristics are unknown.

Other possible consequences from deep-sea mining from which the impact is unknown are for

example light pollution (artificial light will probably be used to be able to get footage from the sea bottom), release of toxins and contamination from the seabed during the mining processes and temperature increase of the water due to vehicle operation. It must be noted that further research on environmental impact is necessary before deep-sea mining can take off.

**Areas of Particular Environmental Interest**

In order to mitigate the environmental impact, the International Seabed Authority has adopted an environmental management plan for the CCZ, based on the work of a group of multidisciplinary experts that discussed this matter at the University of Hawaii in October 2007[71]. Based on their recommendations, the APEI (Areas of Particular Environmental Interest) have been invoked in the Clarion-Clipperton Zone. These APEI are based on the following rationales:

- Divide the CCZ in 9 ecological subregions, each with its own Area of Particular Environmental Interest (APEI), which are excluded from all possible mining
- The APEI should be integrated into the current exploration areas framework
- Make sure that with these APEI's 30% of the area is protected
- Each APEI should contain the full range of habitat types found within this subregion, consisting of abyssal hills and plains, seamounts and fracture zones.

These recommendations were based on estimations regarding the impacts on the seafloor due to deep-sea mining as simulated and investigated in previous research[61] and on guidelines provided by ISA [39] and conservation biology. It was estimated that the mining will affect large areas of seafloor due to sediment plumes (reaching tens of kilometers from site) and direct disturbance (affecting 300-600 $km^2$ $y^{-1}$). The size of the APEI is aimed for to be bigger than the distance of movement of the animals. The APEI's core have a 100 kilometer wide buffer zone, to protect the benthic life in this core from the mining plumes. These two recommendations have lead to the 400 x 400 kilometers dimension of each APEI. In Figure 2.8 it is seen that these area's of particular environmental interest are implemented in the exploration areas framework and are indeed kept free from any mining contracts.

# 3

# Deep-Sea Nodule Mining Technology

To recover the deep sea minerals from the seafloor, different technologies have been studied throughout the years. The mining can be divided in different stages, from which a part takes places subsea and the other part takes place at the surface, as can be seen in Figure 3.1. From these stages the first two are the most technological challenging, as this in subsea (waterdepth between 4000 m and 6000 m, high pressures) and therefore different techniques are needed with regards to terrestrial mining.

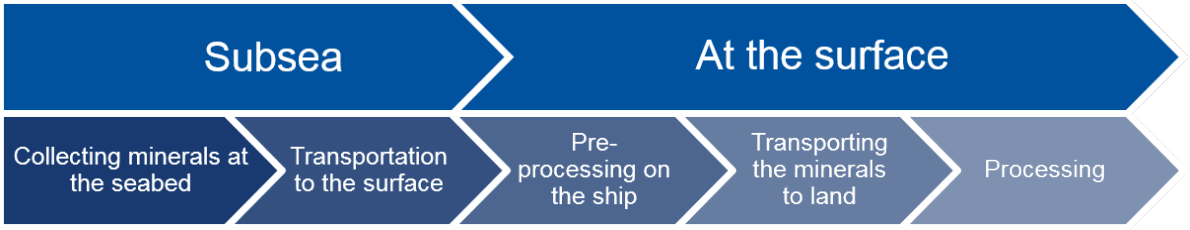


Figure 3.1: Different stages of deep-sea mining

Generally spoken, a collector-lift deep-sea mining system consists of three main subsystems.

- **Seafloor Production Tool** is the equipment that is collecting the deep-sea minerals.
- **Vertical Transport System** is used to transport the collected mineral from seabed to the surface.
- **Production Support Vessel** is used to store all the mined minerals, will contain most of the power units and machinery needed to mine. Transport vessels can be used to unload this PSV to sustain a continuous production. These vessels will transport the minerals to land where it will be processed.

A composition of a conventional deep-sea polymetallic nodule mining system using a flexible riser is shown in Figure 3.2. The three mentioned subsystems of a deep-sea mining system are visualized and will be further elaborated in the following section.

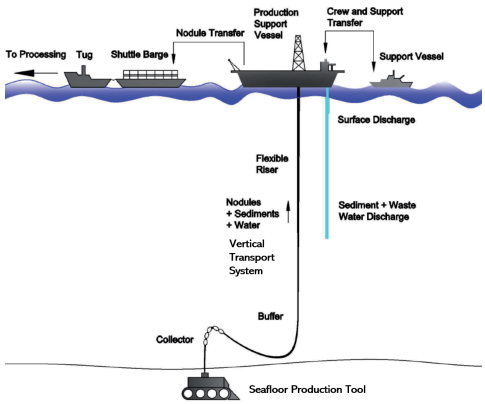


Figure 3.2: A conventional deep-sea mining system using a flexible riser as Vertical Transport system

The state-of-the-art technology for the mining of polymetallic will be discussed in this chapter. More information about the mining of other minerals can be found in other research [56],[40] & [6]

## 3.1. Polymetallic Nodule Mining Method

For the mining of polymetallic nodules, three different methods have been used till this date. The two pioneering technologies were the Continuous Line Bucket system (CLB) and secondly the use of Autonomous Underwater Vehicles (AUV's). The third method is a hydraulic mining system. This hydraulic system is an example of a collector-lift system, which has a range of technical solutions that will be discussed further in this section .

### Continuous Line Bucket System

The Continuous Line Bucket system was tested in 1970 by Yoshoi Masuda under charter of Japan Ocean Resources Association aboard the vessel "Chiyoda Maru No. 2" [46] in a depth of 3755m. In this concept, only one vessel was used. A long continuous line is hung over the side of the vessel, to which the buckets that collect the nodules are connected. As the ships moves sideways, as can be seen in Figure 3.3, the line is being hauled in on one side while being payed out on the other side. This way a path along the seafloor is swept. In CLB, the Seafloor Production Tool and Vertical Transport System are combined into one system. More tests have been caried out by Japanese researchers in 1972, 1975 and 1987 [45]. Rich deposits of polymetallic nodules have been retrieved from the bottom of the Clarion-Clipperton Zone during these tests. The main disadvantages are the lack of maneuverability, therefore lack of production control and heavy plume formation [6]. Eventually the Continuous Line Bucket system was abandoned due to entanglement of the wires [27] and it was proven to be hazardous [56].

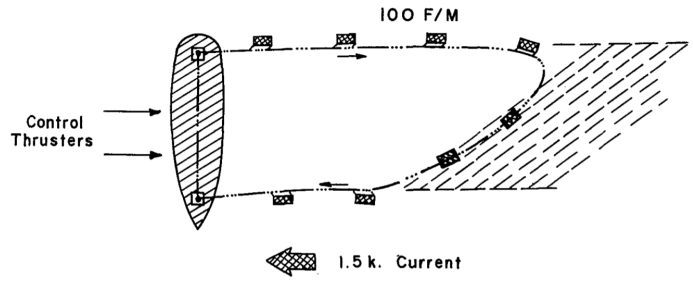


Figure 3.3: Continuous Line Bucket system as tested by Yoshoi Masuda [46]

### Autonomous Underwater Vehicles

With this concept, independent vehicles drop down to the seabed, collect the nodules and "swim" back to the PSV. Also in this concept a combined SPT and VTS system is used. When using many AUV's that are simple and cheap that create enough production a economically viable solution could be met. No harvesting of the seabed is necessary with the AUV system, as the nodules would be individually picked from the seabed. This will decrease the environmental issues of deep sea mining significantly, as less disturbing of the seabed and less turbidity takes place. The disadvantages of this system are the energy use, the high costs of research and development (due to its low level of technology readiness) and the chance of losing a shuttle.

### Collector-Lift System

An example of the collector-lift system was designed in 1988 by the French group Gemonod in the form of a hydraulic mining system. It consisted of a semi-submersible platform with an almost 5 kilometer long steel rigid pipe, combined with a 600 m long, 38 cm diameter flexible hose that connected the end of the tube to a collector on the seafloor [56]. In the following sections the different options and challenges are stated for the three main subsystems.

#### Seafloor Production Tool

The main function of the SPT is the collection of nodules from the seafloor and supply them to the Vertical Transport System. To do so, the SPT needs a collector (to collect the nodules) and propulsion (to

enable the SPT to manoeuvre over the seafloor). The SPT is remotely-operated from the vessel. The collection efficiency combines different components such as swept area, propulsion speed, ratio between encountered nodules and actually collected nodules and the downtime of the SPT. With regards to the environmental issues, the area of disturbed seabed, the severity of disturbing and the associated turbidity are important.

### Vertical Transport System

Multiple technologies to transport the nodules from the seabed to the surface have been developed and tested. Here an overview of the different vertical transport systems are given, which generally can be divided in three groups: Hydraulic lift, airlift and mechanical lift.

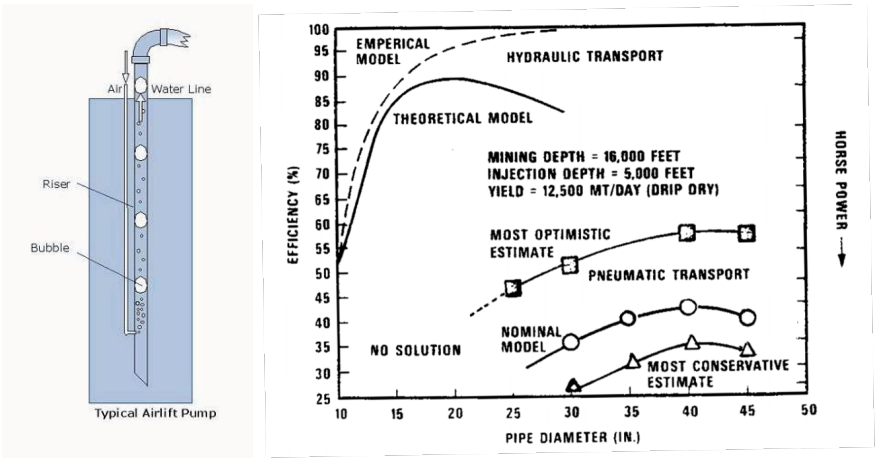


(a) Typical airlift system [27] (b) Performance estimate of nodule lift by hydraulic and pneumatic (airlift) systems[16]

Figure 3.4: CMEMS daily mean currents from a two year record post-processed with Matlab

- **Hydraulic Lift System** The hydraulic lift system is a proven system from the oil- and gasindustry, as the same hydraulic pumps are currently used in deep-ocean drilling operations. They drill cuttings and drill-fluids are transported in the form of slurry to the surface, whereas in the deep-sea mining operations the slurry will consists of the collected nodules. The nodules will form a less uniform slurry, which can have a more wearing effect on the riser pipe [27]. Another difference with the oil and gas industry is the increased depth. Pumping the nodules over a distance of 4.000 m to 6000 m will require booster stations (additional pumps) along the riser. A disadvantage of this system, as this means that a lot of vital components are beneath the surface.
- **Airlift System** A schematic of a typical airlift pump can be seen in Figure 3.4(a). The principle of an airlift pump is as following: Air is injected into the riser to reduce the density of the slurry. Due to the injected air the density in the riser will become lower than the hydrostatic pressure on the outside. Two upward forces now work to transport the slurry to the PSV, the interaction force between the nodules and the rising air bubbles and the upward flow due to the pressure difference [40]. The principle of the airlift system is relatively simple, but it has several disadvantages. High power is required to pump the air several kilometers down. Besides that, the system is vulnerable to frequent clogging. As can be seen in Figure 3.4(b), airlift (pneumatic lifting) has a much lower efficiency than hydraulic lifting [16].
- **Mechanical Lift System** Instead of converting mechanical energy in a flow of water to pump up the nodules, the mechanical energy itself can be used to vertically transport the nodules using buckets. The buckets are filled at the seabed and lifted by a hoisting winch to the PSV. The Continuous Line Bucket is an example of a mechanical lift system, but this is also possible with a single or double bucket lifting system. An advantage of this system is that most of the vital parts of the deep sea mining system are located above the waterline, which makes maintenance or incidents easier to cope with. Very little research has been done about the vertical transport by means of mechanical lifting. Siemag, a company that specializes

in hoisting ore in terrestrial mining, proposed a system to Nautilus Minerals Limited that was able to hoist 100 tonnes kibbles with a speed of 1.8 meters per second [34]. Unfortunately, no experiments or research can be found in the technical literature.

#### Production Support Vessel

The PSV will contain everything to support the deep-sea mining operations. It will sail to the mining location with all the equipment and be its connection with the surface the whole time during operation. The nodules are transported to the PSV, where they can be processed, stored and investigated. The PSV will separate the nodules from the slurry and discharge the excess water. The PSV will contain all the power supply, the control mechanisms and machinery to be able to transfer the nodules to other vessels. It also needs to have all the facilities to support and house the crew.

### Environmental challenges

As mentioned in Section 2.3 there are several challenges to be faced with regards to mitigating the environmental impact of deep-sea mining. This needs to be accounted for in the technical design of the deep-sea mining system and will influence engineering choices. Sediment plumes are an example of an environmental consequence that needs to be accounted for in the design[51]. Sediment plumes will be created while harvesting the nodules as the ground is disturbed and as the separated sediment (from the nodules) is discharged as waste-water by the production support vessel [30]. Discharge water and released sediments are thought to be the main residuals during the deep-sea mining process. This turbulent water may contain fine sediments and heavy metals, that will be released in the water column. Figure 3.2 shows a technology where the discharged sediment and water is pumped back at about half the water depth. For the Solwara 1 project by Nautilus Minerals it was proposed (Nautilus went bankrupt in 2019, before they started the project) that the discharged sediment and water would be returned to 25-50 m above the seabed [55]. As already stated in 2.3, the sediment plumes (turbidity) is a research topic of its own and must be investigated further. However, it must be accounted for in the design as it is clear that it can be a showstopper.

## 3.2. Boskalis' Deep-Sea Mining Method

In Section 3.1 the different parts of a deep-sea mining system have been elaborated. In this section, Boskalis' approach to deep-sea mining technology is discussed, again by using the three subsystems mentioned in the previous section. The main focus in the concept and in this thesis is the Vertical Transport System, which consists out of mechanically lifted skips that are filled with the mined minerals. An overview of the system is given in Figure 3.5 and the three subsystems are discussed in the following sections. The dimensions and detailed characteristics are given in Chapter 5.

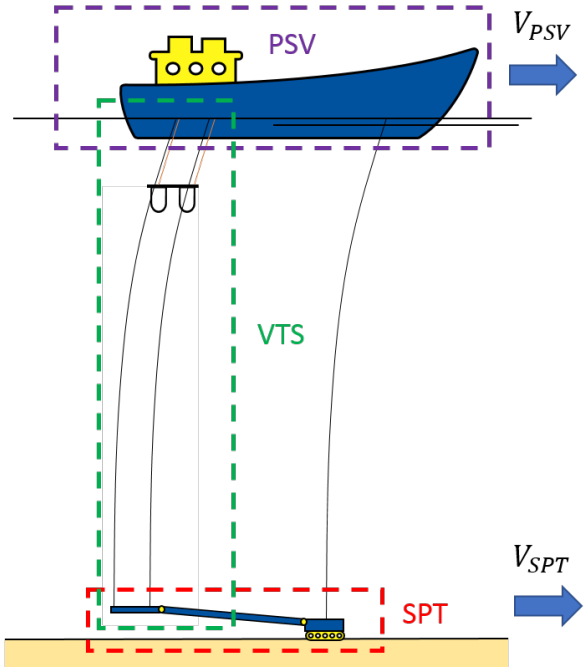


Figure 3.5: Subsystems of the deep-sea mining concept

### Seafloor Production Tool

As stated, the SPT is responsible for the collection of the nodules from the seabed. As can be seen in Figure 3.6 the SPT consists out of four subsystems. In this section more information is given about these subsystems, following the direction that the nodules will travel during mining.

- **Harvester** As discussed in Section 2.1 the polymetallic nodules are "up for graps", which means that the harvester must be able to scrape off the upper layer (about 10 cm) of the soil. This mixture of seabed sediment and nodules is pumped up while the harvester proceeds over the seabed. As stated in Section 2.2, this upper layer of the seabed consists of a very soft, semi-liquid sediment. It is expected that the harvester will experience negligible bearing capacity from this layer. The second layer, despite composed of a more cohesive layer with constant strength, also has a low bearing capacity. The method of propulsion on the harvester are Archimedes screws (or wormwheels) as they provide good traction and stability in these soft soils. The harvester is connected to the PSV with an umbilical for power and a harvester lifting wire to deploy or hoist the system.
- **Ladder** When the nodule-sediment slurry is harvested, it needs to be transported to the docking unit. The ladder takes care of this transportation. It is connected to the docking unit and the harvester by joints that allow the different parts to rotate relative to each other. This is desirable to be able to manoeuvre over the changing slopes of the seabed while keeping the docking unit horizontal.
- **Docking Unit** The slurry is pumped up to the docking unit, where the skips are "docked". At the docking unit, the nodules are separated from the sediment. The nodules with as less sediment as possible are loaded into the skips. The docking unit is hanged off and kept horizontal by four wires that are connected to the PSV at about 30 meters above the seabed.
- **Slurry Discharge** The slurry discharge, or water return system, returns the excess sediment that has been

separated from the slurry by the docking unit to the seabed. This way no energy is used to hoist or pump up (as would be done in hydraulic or airlift ) the sediment. With regards to the importance of minimalizing the sediment plumes and turbidity, this way the sediment is returned to the path is was harvested from and turbidity due to water discharge is kept at a minimum.

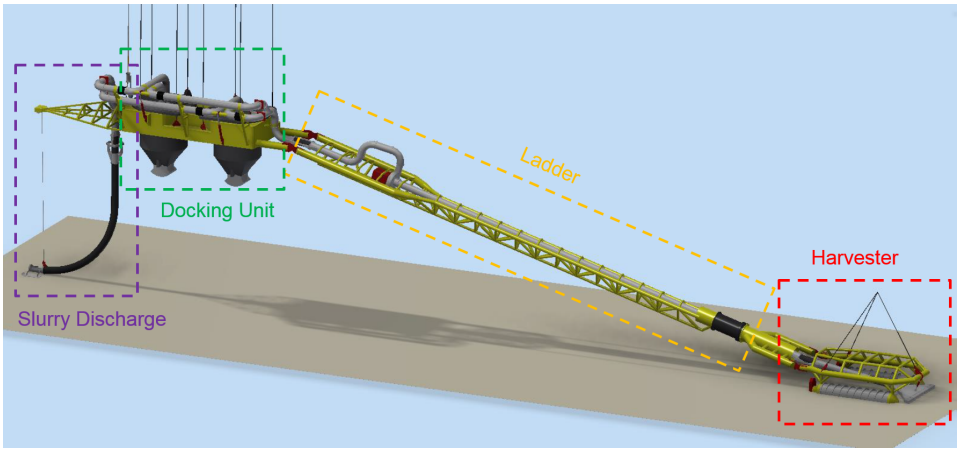


Figure 3.6: The Seafloor Production Tool with all its different subsystems highlighted

### Vertical Transport System

In this concept the vertical transport is done by means of mechanical lifting. The systems consists of two skips that travel up and down, from the PSV to the docking unit, alternatively to ensure a continuous production. The hoisting and lowering of the skips is done by means of winches on board of the PSV. While one skip is being filled at the bottom, the other skip is making the round trip to the vessel. Each skip is attached to two winch wires and has two guidance eyelet, through which the wires run that are attached to the docking unit. As these are used by the skips as guidance, they are referred to as guidance wires. An overview of the mining system with all the components is shown in Figure 3.7.

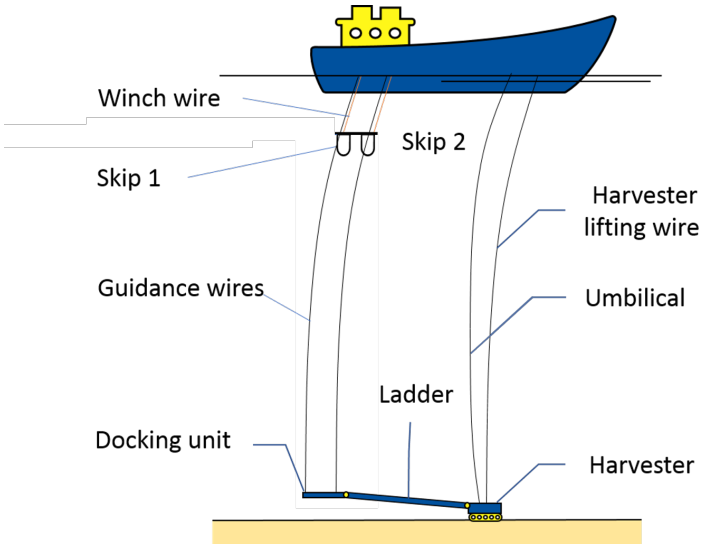


Figure 3.7: Overview of the conceptual mining system with the different components

### Production Support Vessel

The main difference with a general Production Support Vessel as described earlier is the adjustment to fit the mechanical Vertical Transport System that is adopted. Four guidance wires, four winch wires, one umbilical and one harvester lifting wire are needed to operate the system. As the system will need to be able to operate in 6000 meters, every wire needs to be at least a bit more than 6000 meter. Every wire needs a winch installation and a drum that can fit the required length of wire. These rope installations must be able to keep a constant

tension and possibly account for tension fluctuations by means of active heave compensation. Besides capacity for 60 kilometers of wire, the vessel will act as the power source, housing facility and will need sufficient storage capacity. It will need to be able to keep its position and follow the harvester securely, so a dynamic positioning system is required. An artist impression of the production support vessel is shown in figure 3.8.

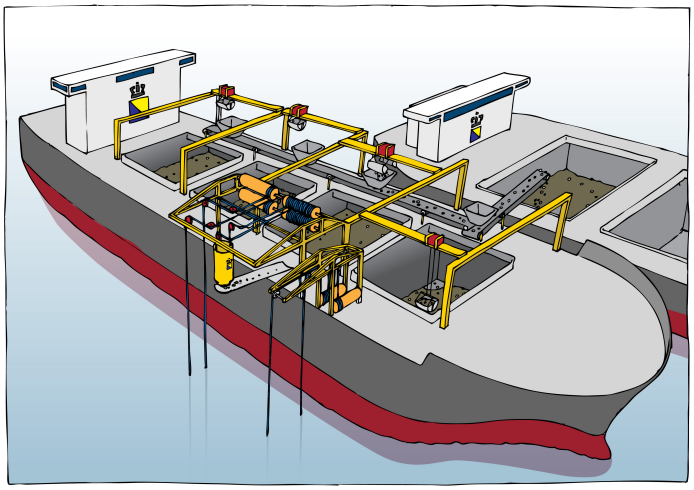

Figure 3.8: Production Support Vessel

## 3.3. Production Cycle

With a continuous production as goal, two skips are alternately filled, hoisted, emptied and lowered. The production cycle is based on a desired production rate. The production rate determines how fast the skips are loaded, which determines how fast the other skip needs to travel to the surface, unload and descend to the SPT. The production characteristics are given in table 3.3.

| **Characteristic** | **Value** | **Unit** |
|---|---|---|
| Seafloor abundance | 10 | [kg/$m^2$] |
| Mining head effective width | 8 | [m] |
| Progress velocity | 0.1 | [m/s] |
| Collecting efficiency | 85 | [%] |
| Lifting speed | 2 | [m/s] |
| Lowering speed | 2 | [m/s] |

Table 3.1: Characteristics that govern the production cycle

The production can be divided into three main phases:

- **Startup phase** The PSV arrives at the location that will be mined. The SPT is lowered to the seabed.
- **Production phase** Once the SPT is on the seabed, the mining will commence. As stated, the two skips will alternatively been filled to ensure continuous production. Based on the characteristics in table 3.3 the production cycle as presented in Figure 3.2 is composed. Here 2 cycles are shown, but this process will continue as long as weather/abundance of nodules/integrity of machinery will allow. During the production phase, vessels are needed to transport the nodules from the PSV to land to be processed.
- **End of work phase** Once the work will stop due to reasons that were mentioned in the previous item, the SPT needs to be lifted back to the PSV. Now the equipment is harbored in case of bad weather, a new location can be visited or maintenance can be done.

| **Component** | **Cycle 1** | | | **Cycle 2** | | |
|---|---|---|---|---|---|---|
| **Skip 1** | Fill with nodules | | | Hoist | Empty | Lower |
| **Skip 2** | Hoist | Empty | Lower | Fill with nodules | | |
| **Time [min]** | 60 | 30 | 60 | 60 | 30 | 60 |
| **Total time [min]** | 150 | | | 150 | | |

Table 3.2: Production cycle that is continuously repeated

### Production phases

The following figures illustrate the different production phases. The next section will discuss the problem identification and will also identify the problems expected in each production phase.

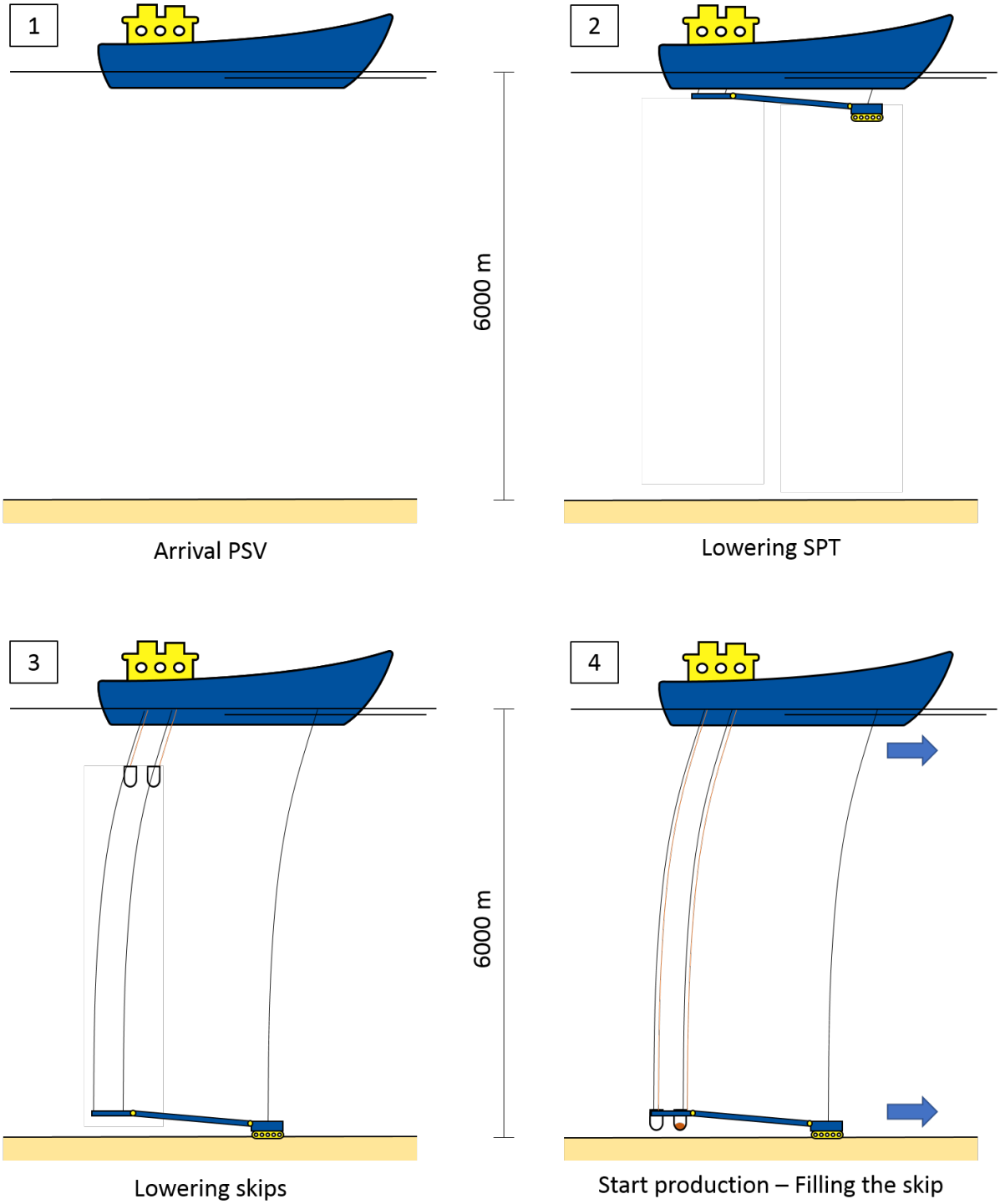

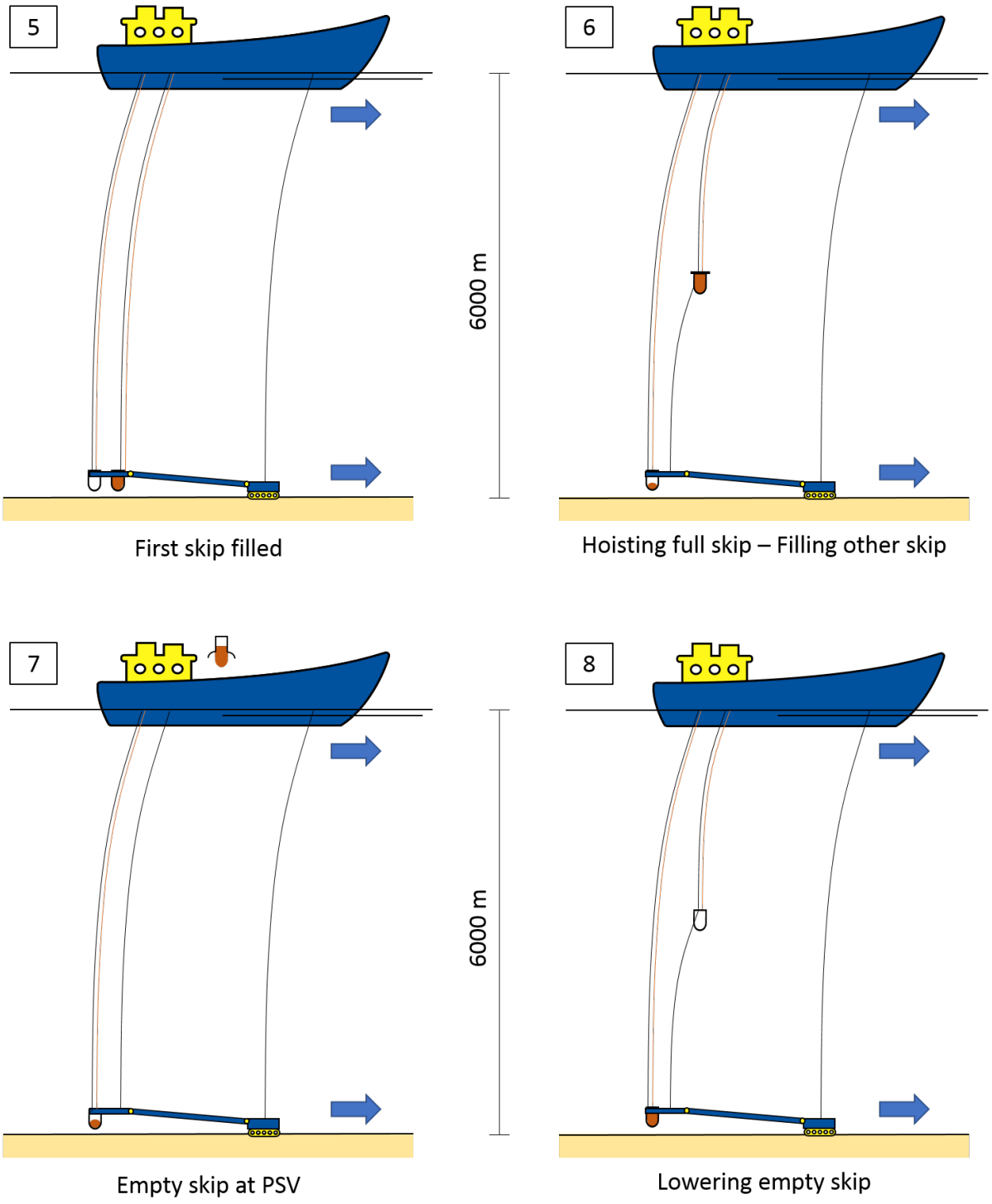


- **Phase 1 - Arrival PSV**
  The PSV arrives at the mining location, carrying the SPT and other needed equipment for the operations. The dynamic positioning system is activated.
- **Phase 2 - Lowering SPT**
  The SPT is lifted over the side of the vessel, through the splash zone and lowered onto the seabed. This will be a critical situation, as the SPT will experience drag due to current. The behaviour of the freehanging SPT in the current is not discussed in this thesis, but needs to be investigated in the future. The harvester must be put on the ground with ease, whilst the docking unit should never touch the seabed.

- **Phase 3 - Lowering skips**
  After the SPT is put on the seabed, the empty skips will follow. As the guidance wires are in place, the skips will be lowered along these wires. The guidance wires will run through eyelets attached to the skips. The skips are lowered with a velocity of 2 m/s. The arrival of the skips in the docking unit is important, as the skips must be lowered in with ease.
- **Phase 4 - Start Production**
  All the equipment is now at the seabed and production will start. This results in a forward velocity of the SPT of 0.1m/s. The PSV will follow with the same speed, to enable a constant distance between the PSV and SPT. While filling the skips with the collected nodules, the skip will gain mass. To ensure constant tension in the guidance wires, this increased mass will be taken by the winch wires.
- **Phase 5 - First skip filled**
  When one skip is full, the production flow must be transferred to the other skip, so a continuous production can be sustained. The full skip will than be lifted to the PSV to be emptied.
- **Phase 6 - Hoisting full skip**
  The release out of the docking unit is important, as dynamic movement of the skip relative to the docking unit can be expected. The full skip will travel through the water column, where it is subjected to the natural current and the current due to the forward velocity and experiences a drag force due to its hoisting velocity. To be emptied at the PSV, the skip must be hoisted through the splash-zone and above the waterline, where it loses its buoyancy. This leads to rapid differences in tension in the wires. Due to the vessel motion the top of the ropes will experience heave motions. This results in skip motions and dynamic tensions.
- **Phase 7 - Empty skip at PSV**
  At the PSV the content of the skip needs to be transferred to the storage. The skip is lifted over the cargo holds and the valve on the bottom is opened to drop the mined nodules in.
- **Phase 8 - Lowering empty skip**
  The skip is lowered to the seabed again. It needs to go through the splash-zone and below the waterline. During the lowering, the hoist wires must remain under tension at all times, so no slack situation will occur. This means that the winch pay-out should not be higher than the maximum velocity of the skip when free-falling in water. The arrival of the skip in the docking unit is again important.

## 3.4. Problem identification

In this chapter the deep-sea mining system has been elaborated. Now the main challenges and problems of this system will be identified and elaborated. Many of the challenges are the same as with deepwater operations.

### Lifting and lowering technology

#### Selection of wire material

Steel wires would be favourable to use in this system, as they are very well understood from years of use in the offshore oil industry and durable. Unfortunately they are not suitable for deep-sea mining activities, as at 6000m the safe working load is entirely used up by the self weight of the steel wire. Fibre ropes with HPME fibres however are neutrally buoyant (their density is about the same as the density of seawater) and therefore their payload is independent of the rope length when lifting below the waterline. This makes synthetic rope the potential answer to the self-weight problems [70]. Other advantages are the small bend radii and the possibility to be repaired. The SIRIUS (Safe Installation with Ropes In Ultradeep SEA) JIP full scale testing program [74] showed that where steel wire ropes tend to fail from the inside and not much visual signs can be found when the steel wire rope is nearing the end of its lifetime. Fibre ropes however have very clear visual indications that the rope needs repairing to continue safe work. This visual inspection can be done every lifting cycle for the hoisting wires. The guidance wires can be inspected every time the SPT is lifted, which happens if an area is mined or work must be stopped due to the weather.
Definitely compared to steel wire, there is little synthetic fibre rope track record. There are potential problems related to creep, stretch and a relatively low melting point. Repetitive tasks, like the hoisting and lowering

in this system, is still a relative unknown field and more research is needed on the durability and life time of synthetic fibre rope [70]. The fibre rope characteristics will be discussed in further detail in Section 5.2.

#### Dynamic effects

Dynamic effects can be very significant when lowering heavy weight on long ropes. As the depth of the weight increases, the length of the rope will increase and the stiffness of the rope will decrease. Due to this varying stiffness during lowering/hoisting, it is expected that there will nearly always be a depth at which resonant response will occur. This can lead to great excitations of subsea equipment and high dynamic tensions in the rope.

#### Splash zone

The skip need to be lifted above or lowered through the splashzone. In this zone, varying forces will act on the skips, due to the waves, changing buoyancy, slamming forces and changing added mass.

#### Drum winches

Drum winches are not suitable for synthetic ropes. The tensioned synthetic ropes have the tendency to get embedded in the underlying layers when spooled upon a drum winch. Therefore a mechanically more complex system is needed for the handling of the synthetic ropes, with tensioners and traction winches.

### Currents

Current, both due to the production velocity of the system and the naturally occurring current, will have influence on the system. Deepwater is often characterised by complex currents, changing over depth, with relatively strong surface currents and low benthic current. The current is discussed in more depth in Chapter 4.1.

#### Drag

Due to the current, a drag force will be exerted on the system. As the system exists over a depth of 6000m drag is expected to be of significance in the design. Drag converted into horizontal force needs to be accounted for by the ship, the harvester or both, for reliable station keeping.

#### Vortex Induced Vibrations(VIV)

Another effect of fluid flow around submerged bodies is vortex shedding. On the downstream side of the body, low-pressure vortices will alternatively detach periodically from each side of the body. The body will tend to move towards this low-pressure zone. This behaviour is especially known to long cylinders and has been topic of research for many years within the offshore industry [7]. Vortex induced vibrations can lead to fatigue damage and increased drag on the ropes.

### System control and positioning

#### Seafloor Production Tool

The harvester is positioned on the seafloor, 6 kilometer below the PSV, from where it needs to be controlled. The control on board of the ship needs visuals of the seafloor, to avoid cliffs or seamounts that are too steep, delivered by camera's on the SPT or ROV's. The position reference of the harvester with respect to the PSV is important, as they are physically connected by the guidance wires. The SPT will be connected to the vessel with an umbilical, to provide the information from the seabed to the surface. It is expected that the SPT

needs its own positioning reference system, as position reference through conventional acoustic systems is a challenge in these great depths [70].
The docking unit is designed to be lifted up and kept horizontally with the four guidance wires about 30 meters above the seabed. Its position is controlled through its connection with the harvester and the position of the ship. The inclination of the docking unit is controlled by the guidance wires and must be kept within working range. The vertical position of the docking unit is controlled by the guidance wires and as these are connected to the vessel they are subjected to movement of the vessel. The communication with the PSV may be lagging due to the great depth, which will make the control unreliable. There is a hazard of grounding the docking unit.

#### Vertical Transport System

Besides the lifting of the docking unit, the guidance wires role is to guide the skips. They prevent the skips to rotate and guide them into the docking unit. Even though the guidance wires are in place, the skips arrival at the docking unit could still be critical.
Having many wires in the water column, each with a different tension, passing skips and changing currents, there is a risk of entanglement. Entanglement could lead to great damages and downtime and in severe cases even to the snapping of cables.

#### Production Support Vessel

As stated earlier, the position of the PSV with regards to the SPT (or vice versa) is important for the control of the system. The mining activities will take place in water that is to deep for acoustic position reference of the PSV. A sufficient dynamic positioning system should be in place at the PSV.

### Metocean effects and weather window requirements

For every deep-sea mining concept a continuous production is desirable. The hoisting of the SPT in case of unworkable weather takes long and so does the lowering when work can continue. To assure a high workability, this deep-sea mining concept must be tested and designed for high sea-states, so the longest weather windows can be worked in. As will be discussed in Section 4.3, the aimed for workability is 99%. The hoist and lowering speed is adjustable, so it is desirable to evaluate the maximum allowable values, so the shortest down time can be achieved.

# 4
# Environmental Data

As deep-sea mining will take place on the open ocean, current, wind and waves will work upon the system. The environmental data will affect the system and needs to be accounted for. For different types of loading a realistic data set must be gathered:

- **Current:** The deep-sea mining system will be working in great depths and the current will exert drag on the wires, subsea equipment and the vessel. VIV could also occur due to the current. A uni-directional current is created based on a combination of modeldata and in-situ measurements. This current is later used as input in simulations.
- **Waves:** The waves will bring the vessel into motion. The deep-sea mining system is connect to the vessel, therefore this motion and forces are passed on to the wires and subsea equipment. If this motion happens to be with a frequency that equals or approaches the eigenperiod of the subsea equipment, excitations and forces will be magnified. Consequently, undesirable situations can occur.
- **Wind:** Forces will be exerted on the vessel due to the wind, but no wind forces are exerted on the subsea equipment. The wind force on the vessel is assumed to be accounted for by the dynamic positioning system. All the waves are generated by the wind, but this energy is captured in the wave data. It is assumed that the wind won't have a lot of influence on the deep-sea mining operations and therefore it is not taken into account in the simulations.

## 4.1. Current

As the system is present in the entire water column up to a depth of 6000m, the current possibly has a large influence on the design criteria. Ocean currents can broadly be divided in two sorts of currents, surface currents and bottom currents [3]. Surface currents are dominated by the global oceanic system, which consists out of five major sea current gyres[1], which can be seen in Figure 4.1. These gyres are also correlated with the global dominant wind directions, both rotating clockwise in the Northern Hemisphere and counterclockwise in the Southern Hemisphere due to the Coriolis Force.
The bottom currents are mostly present due to differences in density caused by changes in temperature and salinity [68]. This can cause bottom currents up to 10 cm/s in the CCZ [3].

| **Physical properties** | **Descriptions** |
|---|---|
| Seafloor topography | Mostly between 4,000 and 6,000 m water depth; a large number of abyssal plains, separated by irregular, often discontinuous ridges. |
| Ocean circulation | Dominated by the North Equatorial Current; average speed of about 10 cm/sec |
| Benthic current | Calm period (0 – 3 cm/s), tidal period (0 – 6 cm/s), and benthic storm (8 cm/s, 24-h Ave.) |

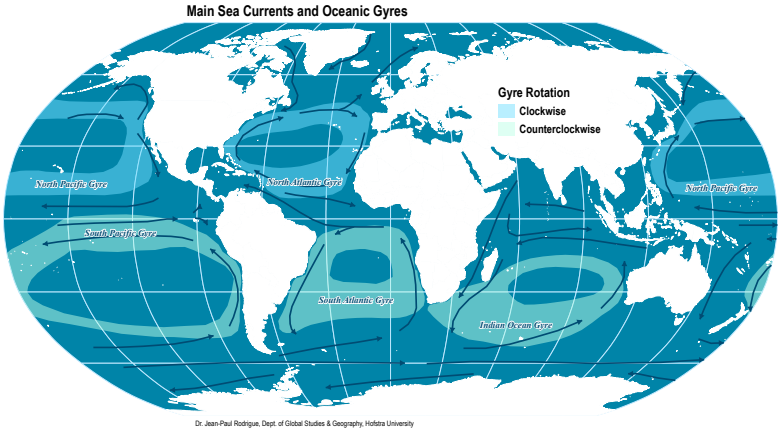


Figure 4.1: World Ocean Gyres [1]

## Modelling current

Unfortunately, there are only a few in situ measurements at great depths in these deep seas. Most of the measurements are from the surface and only sporadically a measurement from a certain depth can be found, as can be seen in the next section. Current measurements over the whole depth profile are not available. Therefore so-called re-analysis is a good option to investigate the currents at the CCZ and form them into a representative sheared current profile which will be used for calculations. Re-analysis are model simulations over a period of time, constantly adjusted by real-time measurements. The file-format is NetCDF (Network Common Data Form), which is an array-oriented scientific data software library. The used model is the NetCDF CMEMS (Copernicus - Marine Environment Monitoring Service) global ocean eddy-resolving re-analysis, based on the real-time global current forecasting CMEMS system. The model has a grid of 1/12°(which is approximately nine kilometers) and delivers daily and monthly mean files of currents, temperature, salinity etc from the surface to the seabed.
The NetCDF data file is post-processed using MATLAB. The extracted information is given as a daily mean north- and eastward velocity over 50 depth levels, for each specific set of coordinates, over a period of two years. From these north- and eastward velocity a total current velocity is derived using equation 4.1.

$$U_{current}(z) = \sqrt{u^2_{currentnorth} + u^2_{currenteast}} \tag{4.1}$$

This means a unidirectional current is formed, whereas in real life this is not always the case. As an unidirectional current will exert the most drag on the system, this case is of most interest. Later on the influence of a non uni-directional current will be assessed. The total current for each depth is calculated and combined to a daily mean current profile, as can be seen in Figure 4.2(a). The minimum, maximum and mean current profile can be seen in Figure 4.2(b). From this data, the current profile that will be used in the simulations is composed. It can be seen that the current profile accounts for relatively high surface current of 1 m/s for the upper 200 meters. It then weakens to a constant 0.1 m/s till the seabed. The depth at this location (chosen as it can be compared to in-situ measurements) is about 4000 meters, therefore the current profile is extrapolated to 6000 meters. This current profile represents an extreme current profile, resulting in the most drag exerted on the system.

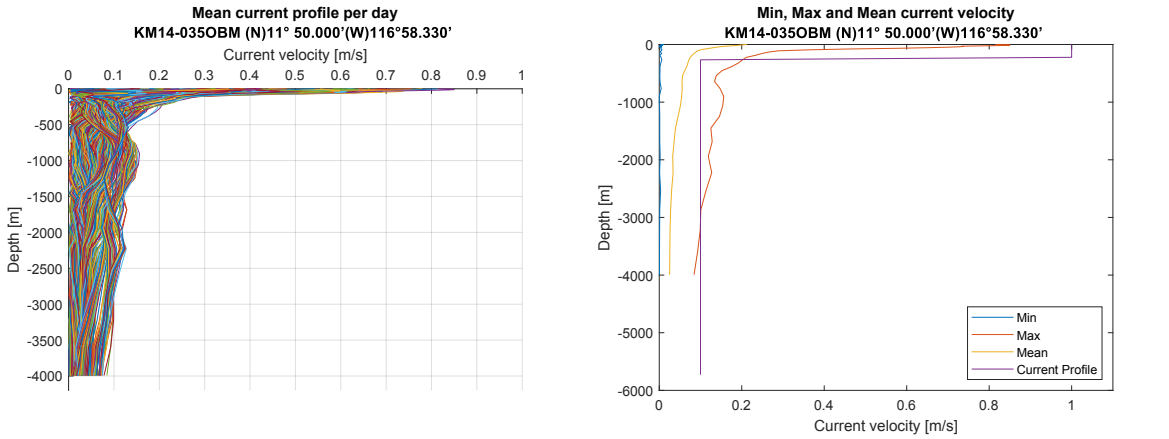


(a) Daily mean current profiles

(b) Minimum, maximum, mean and simulation current profile

Figure 4.2: CMEMS daily mean currents from a two year record post-processed with Matlab

## Data

In 2015, the research cruise SO-240 investigated the benthic seawater circulation within the eastern part of the German license area of the CCZ. During this cruise, three Ocean Bottom Moorings (OBMs) were recovered after two years of deployment[41]. The OBMs had been measuring current velocities from April 2013 till June 2015 at three different locations as described in table 4.1 and shown in Figure 4.3. The measured current velocities are shown in Figure 4.4
The CCZ is an enormous area and with CMEMS a huge amount of current profiles from the last 28 years can be derived. It has been chosen to use the locations closest to the OBM's as a reference location. This way the benthic current data at depth can be verified.

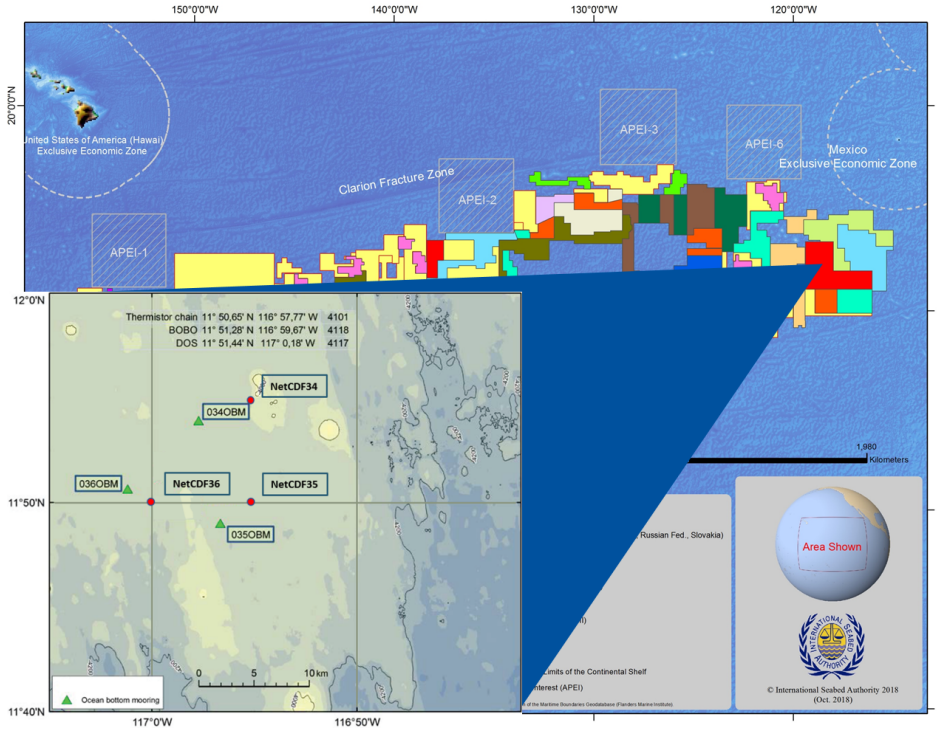


Figure 4.3: Measurement and NetCDF locations within the CCZ [41]

| Ocean Bottom Mooring | KM14-034OBM | KM14-035OBM | KM14-036OBM |
|---|---|---|---|
| **Water depth [m]** | 4108 | 4120 | 4122 |
| **Position latitude [N]** | 11°53.915‘N | 11°48.987‘N | 11°50.619‘N |
| **Position longitude [W]** | 116°57.733‘W | 116°56.669‘W | 117°01.184‘W |
| **Closest NetCDF file location [N]** | 11° 58.330’N | 11° 50.000’N | 11° 50.000’N |
| **Closest NetCDF file location [W]** | 116° 58.330’W | 116° 58.330’W | 117°00.000’W |

Table 4.1: The position and water depth of the three Ocean Bottom Moorings and their closest NetCDF location, used to compare the data.

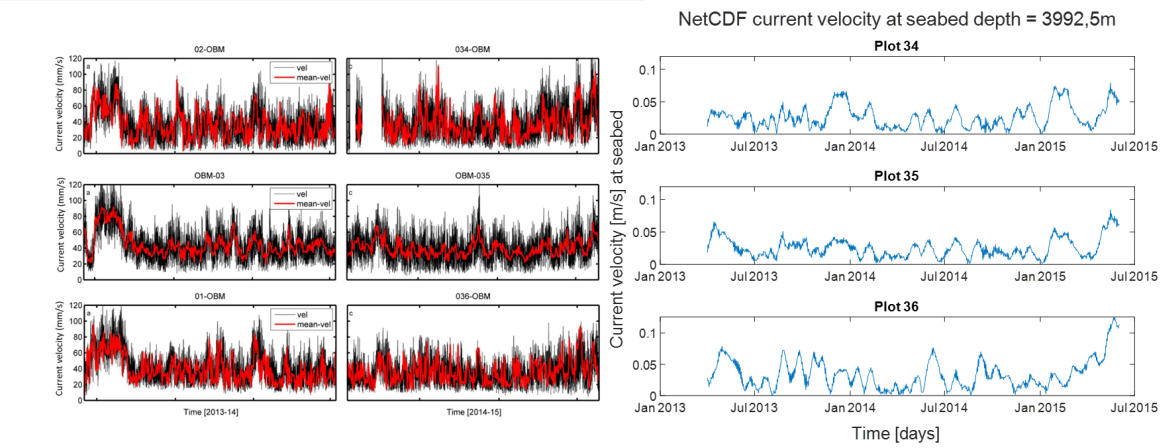


Figure 4.4: Comparison between the in situ measurements and the re-analysis data [41]

In Figure 4.4, the data from the OBM’s at a depth of about 4100 meter is compared with the data from the CMEMS re-analysis at a depth of 3992.5 meter. The in-situ data shows that the maximum measured benthic current velocity is around the 0.12 m/s, but it only reaches this velocity sporadically. The data from the CMEMS re-analysis shows the same maximum benthic current velocity, which are both a daily average. They are not in phase, so the CMEMS model is not validated. However, the maximum values are similar and as a time independent current profile is being composed, this is sufficient.

### Direction

For the current profile that will be used as default in the simulations it is assumed that the current is uni-directional. In practice, this situation will (almost) never occur, as the current direction differs over depth. Where the surface current is mostly dominated by the wind, the bottom current is mostly influenced by differences in density caused by changes in temperature and salinity. From the CMEMS data, which breaks the current velocity down in a north and east velocity, the direction of the current can be derived. To illustrate that the current is not uni-directional, the mean current directions of 75 days are plotted in 4.5. The influence of a non uni-directional current will be simulated in Section 7.1. A uni-directional current 180 degrees relative to the heading of the ship will result in the maximum drag which, but transverse current due to a non uni-directional current can result in a transverse forces which are less easy to account for.

### Discussion

Do to the lack of measurements spread over the whole depth (surface to seabed) it is impossible to verify the current profile. These deep seas sure are unexplored terrain. Although the current profile derived from the model is the most reliable, in situ measurements should be done to get a good overview of the current velocity, direction and change in direction over time at greater depths.

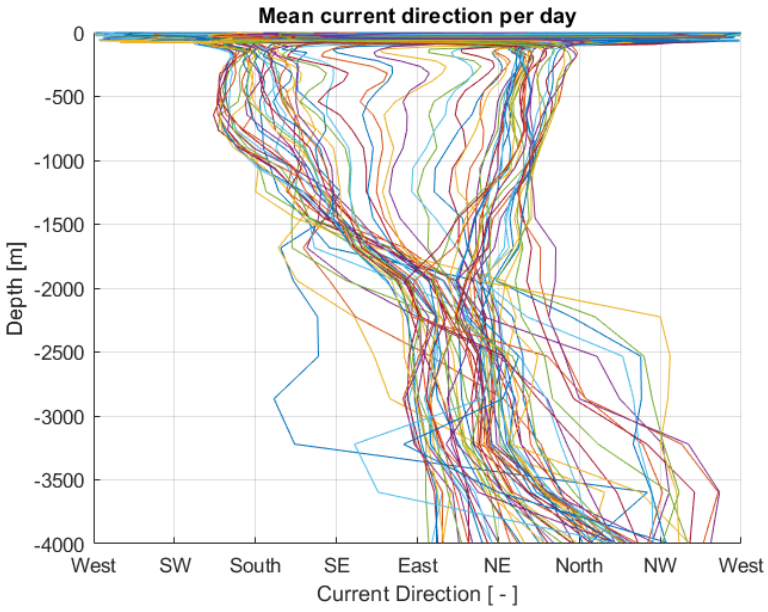


Figure 4.5: Mean current direction over depth, where every line represents a daily average

## 4.2. Salinity and temperature

During the SO-240 research cruise the vertical distribution of sea water properties has been obtained in the same area in the CCZ as the benthic current data discussed earlier. The vertical distribution of the salinity and the temperature are shown in figure 4.6. The salinity shows an increase over the first 170 meters of about 0.8 psu. Below this transition layer, the salinity shows no significant changes. The vertical temperature distribution shows a thermocline layer at a depth of 70 meters. This extends to 150 meters water depth, below which the seawater gradually decreases to 1-4 $^{o}$.

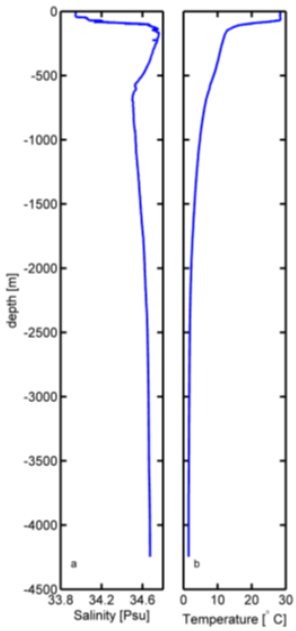


Figure 4.6: CCZ seawater salinity and temperature distribution

## 4.3. Waves

For the closest available location as the benthic current data was subtracted, the metocean data is investigated, 12.0°N 117.00°W. A complex wave system with both wind and swell waves is present at this location. Wind waves mostly occur from a 60-90∘N, while there are two swell systems, one coming from 170-200°N and the other one from 290-310°N, as can be seen in Figure 4.7. In Figure 4.9 the offshore wave roses and workability for total wave height are given. As a year-round production is desirable, the highest possible workability is pursued. A deep-sea mining system that can withstand a 3.5 meter significant wave height ($H_{m0}$), will be able to work almost year-round (a workability of 99%), as can be seen in 4.9. The mean peak period ($T_p$) is about 13 seconds, as can be seen in Figure 4.7 and in the boxplot in Figure 4.8. The environmental data is received from the Boskalis database. The data belongs to a location in the Clarion-Clipperton Zone (12.0°N 117.00°W). This is the same location that was used for the derivation of the current profile.
It is assumed that a fully developed sea state is present at this location in the Clarion-Clipperton zone, as the nearest land is more than thousand kilometers away. Such an idealized wave spectrum is captured by Pierson and Moskowitz in 1964 [64]. The spectrum is based on their assumption that the waves reach an equilibrium with the wind if it had been blowing for a long time over a large area. The Pierson-Moskowitz (PM) spectrum is an emprical relation that they developed from measurements from British ships in 1964 and showed the relationship between the wind and the wave energy distribution. They found that these spectra could be captured in the following form 4.2. Combined with the significant wave height ($H_{m0}$) and the peak period $T_p$ the spectrum can be composed and used as input.

$$S_{PM}(\omega) = \frac{5}{16} \cdot H_S^2 \omega_p^4 \cdot \omega^{-5} \exp\left(-\frac{5}{4}\left(\frac{\omega}{\omega_p}\right)^{-4}\right) \tag{4.2}$$

where

- $H_S$ is the significant wave height
- $\omega$ is the frequency
- $\omega_P$ is the peak frequency

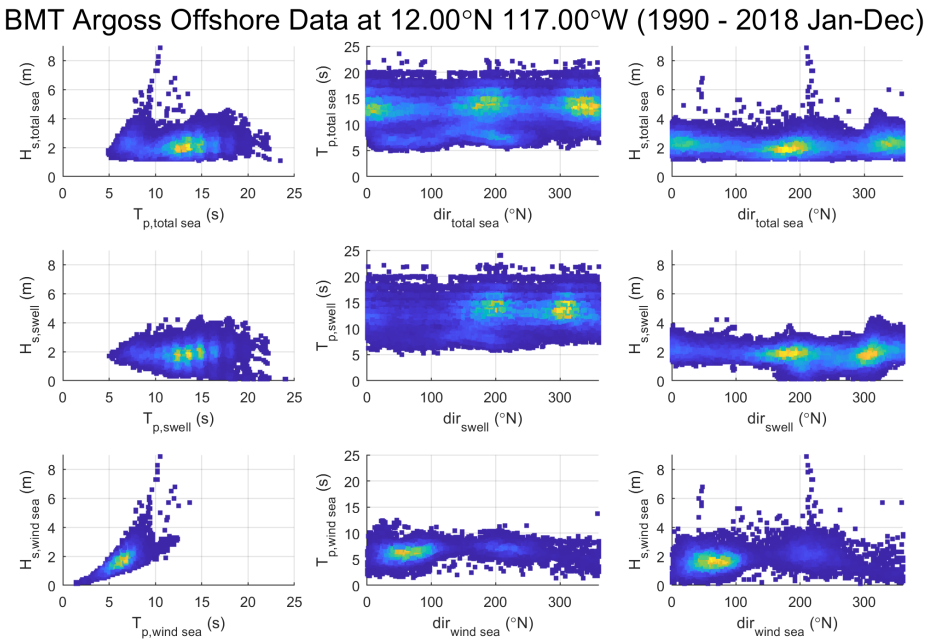


Figure 4.7: BMT Argoss Offshore Data - significant wave height, period and direction

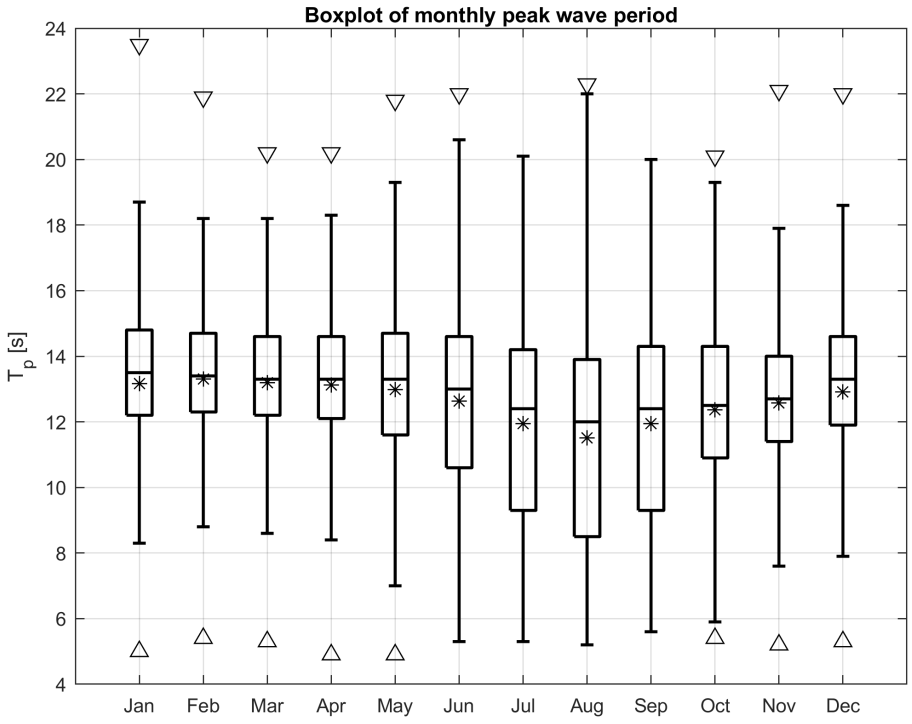


Figure 4.8: Boxplot of monthly peak wave period

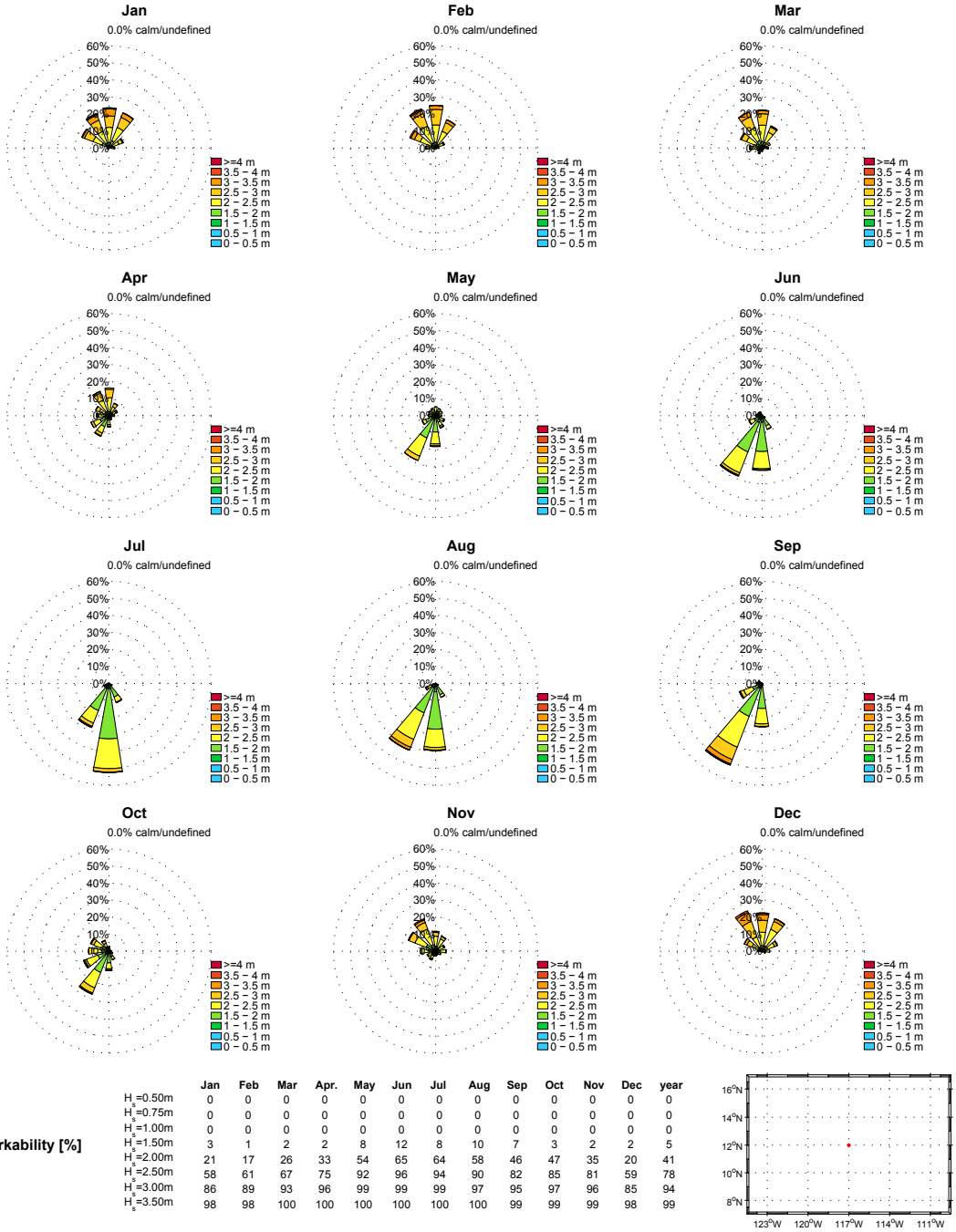


**Workability [%]**

| | Jan | Feb | Mar | Apr. | May | Jun | Jul | Aug | Sep | Oct | Nov | Dec | year |
|---|---|---|---|---|---|---|---|---|---|---|---|---|---|
| $H_s$=0.50m | 0 | 0 | 0 | 0 | 0 | 0 | 0 | 0 | 0 | 0 | 0 | 0 | 0 |
| $H_s$=0.75m | 0 | 0 | 0 | 0 | 0 | 0 | 0 | 0 | 0 | 0 | 0 | 0 | 0 |
| $H_s$=1.00m | 0 | 0 | 0 | 0 | 0 | 0 | 0 | 0 | 0 | 0 | 0 | 0 | 0 |
| $H_s$=1.50m | 3 | 1 | 2 | 2 | 8 | 12 | 8 | 10 | 7 | 3 | 2 | 2 | 5 |
| $H_s$=2.00m | 21 | 17 | 26 | 33 | 54 | 65 | 64 | 58 | 46 | 47 | 35 | 20 | 41 |
| $H_s$=2.50m | 58 | 61 | 67 | 75 | 92 | 96 | 94 | 90 | 82 | 85 | 81 | 59 | 78 |
| $H_s$=3.00m | 86 | 89 | 93 | 96 | 99 | 99 | 99 | 97 | 95 | 97 | 96 | 85 | 94 |
| $H_s$=3.50m | 98 | 98 | 100 | 100 | 100 | 100 | 100 | 100 | 99 | 99 | 99 | 98 | 99 |




Figure 4.9: Offshore wave roses and workability for total wave height (sea and swell)

# 5
# Theoretical background

The mining system and its components have been briefly introduced. The goal of this chapter is the introduction of all the characteristics of the individual components that will later on be used to describe the behaviour of the system when in operation. To do so, first the components of the mining system with their corresponding characteristics are described, where after the details of synthetic fibre rope will be discussed. To conclude hydrodynamic interaction theory will be introduced. The characteristics of the components required for the hydrodynamic interaction simulations are derived.

## 5.1. Concept components

In this section all main dimensions of the individual components are given. These are used as an input in the Orcaflex model.

### Harvester

The harvester is designed for a desired production, which leads to a length of the suction head, an therefore the harvester, of 10 m. The weight of the SPT is shared by the guidance wires lifting it at the docking unit and the ground interaction of the harvester. This weight of the harvester and part of SPT is important for traction of the harvester but also forms a challenge as the soil bearing capacity is expected to be low. Also, more propulsion power is required when more weight needs to be moved.

| **Characteristic** | | **Value** | **Unit** |
|---|---|---|---|
| Length | x | 10 | [$m$] |
| Width | y | 8 | [$m$] |
| Height | z | 3 | [$m$] |

Table 5.1: Harvester main dimensions

### Ladder

The ladder is a rigid, slender structure, that holds all the pipelines responsible for the transportation of the nodule slurry from the harvester to the skip in the docking unit. It is connected with two hinges at both ends. This ensures that the SPT has good maneuverability over the sloping seabed, as it is desired to have a horizontal docking unit. The way in which this is modelled is further discussed in Section 6.1. The main dimensions of the ladder are found in table 5.2.

| **Characteristic** | | **Value** | **Unit** |
|---|---|---|---|
| Length | x | 100 | [m] |
| Width | y | 2 | [m] |
| Height | z | 2 | [m] |

Table 5.2: Ladder main dimensions

### Docking Unit

The docking unit is designed to fit in the two skips and transfer the mined nodules from the ladder to the skips. The weight of the SPT is partly supported by the guidance wires connected to the docking unit and partly resting on the seabed. The attachments points of the guidance wires (G in the figure) and the lifting

point on the skip when they are docked (W in the figure) can be seen in Figure 5.1. The main dimensions of the docking unit can be found in table 5.4.

| **Guidance wires** | **x** | **y** |
|---|---|---|
| 1.1 | -10 | 0 |
| 1.2 | -13 | 6 |
| 2.1 | -2 | 6 |
| 2.2 | -5 | 0 |
| **Winch Wires** | **x** | **y** |
| 1.1 | -13.12 | 0.88 |
| 1.2 | -8.88 | 5.12 |
| 2.1 | -6.12 | 5.12 |
| 2.2 | -1.88 | 0.88 |

Table 5.3: Connection coordinates

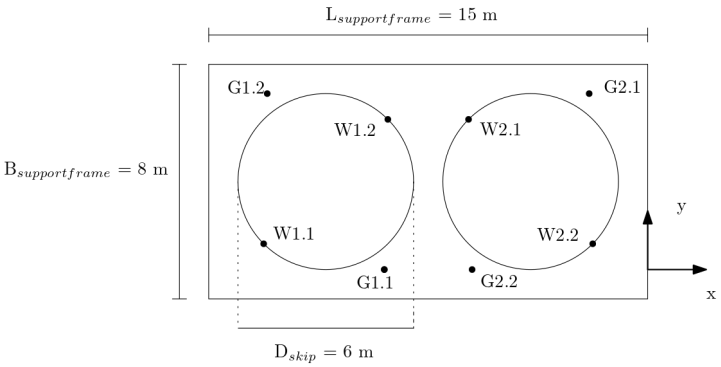


Figure 5.1: Docking Unit topview

| **Characteristic** | | **Value** | **Unit** |
|---|---|---|---|
| Length | x | 15 | [m] |
| Width | y | 8 | [m] |
| Height | z | 0.4 | [m] |

Table 5.4: Docking Unit main dimensions

## Skips

The skips are the containers of the nodules when transported from the seabed to the PSV. The VTS consists out of two skips. The volume of the skips is based on the production and hoisting speed. The volume needs to be big enough to sustain the production for a significant amount of time, so that there is sufficient time to make the round-trip with the other skip. For the simulations the shape of the skip is simplified and approximated by a cylinder with a curved bottom plate. To account for attachments such as the guidance and hoisting eyelet an additional weight factor is added. This results in the following main dimensions:

| **Characteristic** | **Value** | **Unit** |
|---|---|---|
| Skip diameter | 6.00 | [m] |
| Skip height | 10.00 | [m] |
| Cross section | 28.27 | [$m^2$] |
| Content volume | 282.74 | [$m^3$] |
| Average wall thickness | 0.025 | [m] |
| Addition factor for eyelets, etc | 0.10 | [-] |
| Steel density | 7.85 | [$t/m^3$] |
| Steel volume | 5.89 | [$m^3$] |
| Mass of empty skip in air | 46.24 | [t] |

Table 5.5: Main dimensions of the skip

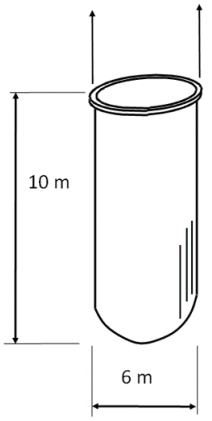


Figure 5.2: Sketch of the skip

The weight of the full skip depends on the mass of the load. The load in this case are the nodules, which have a high porosity. This means that they are filled with water, which also needs to be lifted to the surface. Also, there is water between the nodules, as they are potato shaped and won't neatly sit together in the skip. The void ratio between the nodules is around 0.3.
In German research [61] they assumed a wet density of the nodules of 2 t/m$^3$. This is the density of nodules filled with water, but no water in the voids between the nodules, as seen in Figure 5.3(a) This is supported by nodules samples taken in 1988 in the Indian Ocean, where they researched the acoustic properties of

manganese nodules [52].

The skip, with a volume of 282.72 $m^3$, is fully loaded when it is lifted and it will be empty when lowered again. A full skip will consist of nodules with seawater within the space between them (void ratio = 0.3). These nodules have a wet density of 2 $t/m^3$ (Figure 5.3(a)), but only account for 70% of the volume. The rest will be filled with seawater (Figure 5.3(b)). With these values, the mass of a full skip is calculated. Due to time limitations, the situation where the skip is above the waterline is not taken into account in this thesis. Therefore only the submerged weight is important, but the mass in air of a full skip is also presented in table 5.1. This emphasizes the significant increase in weight when lifting the skip through the splashzone and above the waterline.

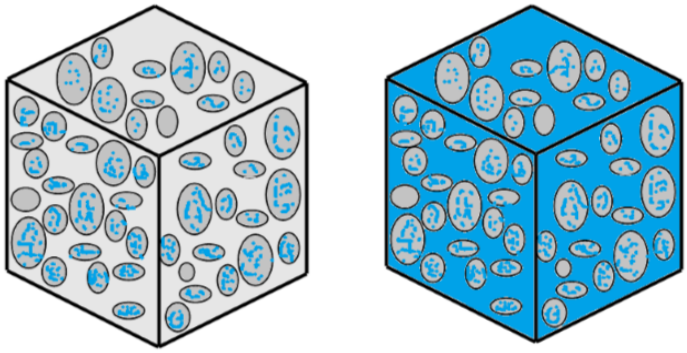

(a) Wet nodules
Internally filled with seawater

(b) Wet nodules + seawater
70% nodules and 30 % seawater

Figure 5.3: Visualization of the wet nodules

| **Characteristic** | **Value** | **Unit** |
|---|---|---|
| Volume Skip | 282.74 | $[m^3]$ |
| Nodules wet density | 2.00 | $[t/m^3]$ |
| Seawater density | 1.025 | $[t/m^3]$ |
| Void ratio | 0.3 | [-] |
| Total wet nodule + seawater mass | 472.73 | [t] |
| Total nodule submerged mass | 182.91 | [t] |
| Dry mass of the skip | 46.24 | [t] |
| Submerged mass of full skip | 223.12 | [t] |
| Mass of full skip in air | 518.97 | [t] |

Eventually there are only two situations that will occur; the lifting of a full skip and the lowering of an empty skip. All this information is used to determine the masses of a full and an empty skip, as summarized in table 5.6. With regards to the mass in air, it is assumed that the water will be contained in the skip. Therefore this is the mass of the wet nodules and the water that fills the void between them.

| **Characteristic** | **Full Skip Value** | **Empty Skip Value** | **Unit** |
|---|---|---|---|
| Mass in air | 518.97 | 46.24 | [t] |
| Submerged mass | 223.12 | 40.20 | [t] |

Table 5.6: Mass of full and empty skip

### Production Support Vessel

The Production Support Vessel will most probably be a bulk carrier vessel, modified to fit the specific needs of deep-sea mining with vertical transportation by means of mechanical lifting. A reference bulk carrier is used as an example, its main dimension are shown in Figure 5.7.

| Characteristic | Value | Unit |
|---|---|---|
| Length | 256.28 | [m] |
| Beam | 43 | [m] |
| Volume | 88196 | [$m^3$] |
| Mass | 90401 | [t] |

Table 5.7: Main dimensions PSV

A bulk carrier has large bulk capacity, so great volumes of nodules can be stored. It also needs a substantial deck space to fit all the fibre rope winches. As stated earlier, nine 6000+ meter rope and a 6000+ meter umbilical are needed and so is its storage and rope handling machinery. A possible arrangement for one rope is shown in Figure 5.4. It has a size of 21 x 9.1 meter. Nine of these installations of deck will take a considerable amount of deck space. Fibre rope has the tendency to, when spooled up under tension, cut in the lower layer on the drum. Begin under tension, the rope is now very hard to unspool. To mitigate this problem, the big sheaves are needed for torque and speed control. This results in a substantial winch size.

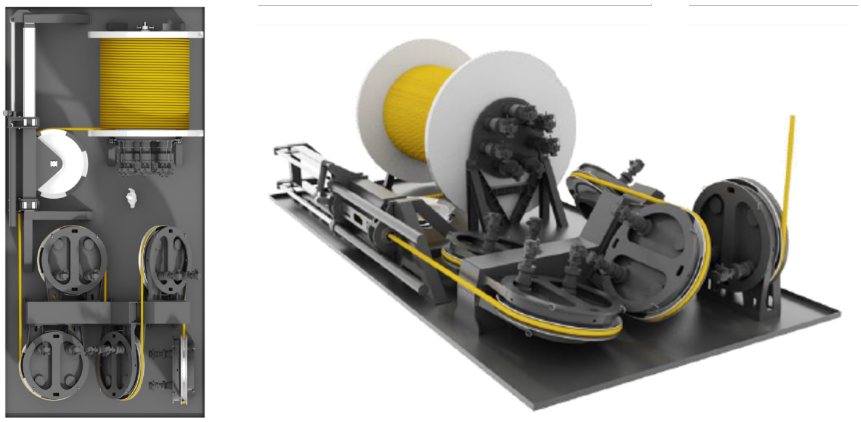

(a) Fibre rope winch; topview

(b) Fibre rope winch

Figure 5.4: Fibre rope winch by Rolls-Royce with a drum capacity of 8500m

## 5.2. Synthetic fibre rope properties

### Steel wire rope in deep water

Steel wire ropes are thoroughly understood as they have been used for many years in the offshore industry. However, they are limited in their application for deep water operations [9]. In Figure 5.5 the lift capacity as a proportion of the surface lift capacity over a varying depth in shown. As the deployment depth increases the lift capacity decreases, all due to the self weight of the steel wire rope. At the working depth that is considered in this thesis, 6000 meters, the safe working load of the majority of steel wire ropes would be completely used up by the self weight, leaving zero hoisting capability [9].

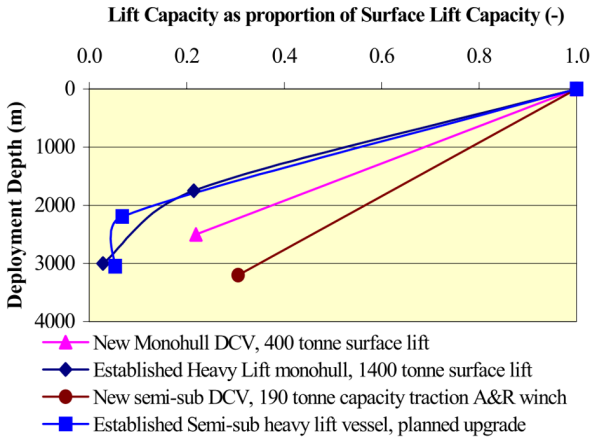


Figure 5.5: Degradation of lift capability with depth [72]

With the exploration of oil and gas fields in water depths beyond the 2000 meters, research has been done in the beginning of the year 2000 to explore the technology gaps that needed to be bridged in order to make these deepwater operations possible [72]. This research shows that , as stated above, self-weight will make conventional steel wire rope systems inefficient in ultra-deep water. Therefore, the industry must turn to deepwater fibre rope deployment systems, as fibre rope is naturally buoyant and therefore the crane capacity will be independent of the deployment depth. This thesis acknowledges this advice and it is assumed that synthetic fibre rope is used instead of the more commonly used steel wire rope.

### Dyneema

In consultation with Boskalis, it has been chosen that for this research a 12-strand braided 80mm Dyneema fibre rope will be used for both the guidance rope and the hoisting rope, as it is assumed to have a sufficient minimum breaking force. The 12-strand braided rope can be seen in Figure 5.6. Its characteristics are derived from the manufacturers catalogue and can be found in table 5.8. Dyneema is a high modulus polyethylene (HPME) fibre, which has a high strength to weight ratio, significantly higher compared to steel. Rope is made from individual fibers which are twisted into yarns. The yarns are twisted into strands where after the strands are braided into rope.

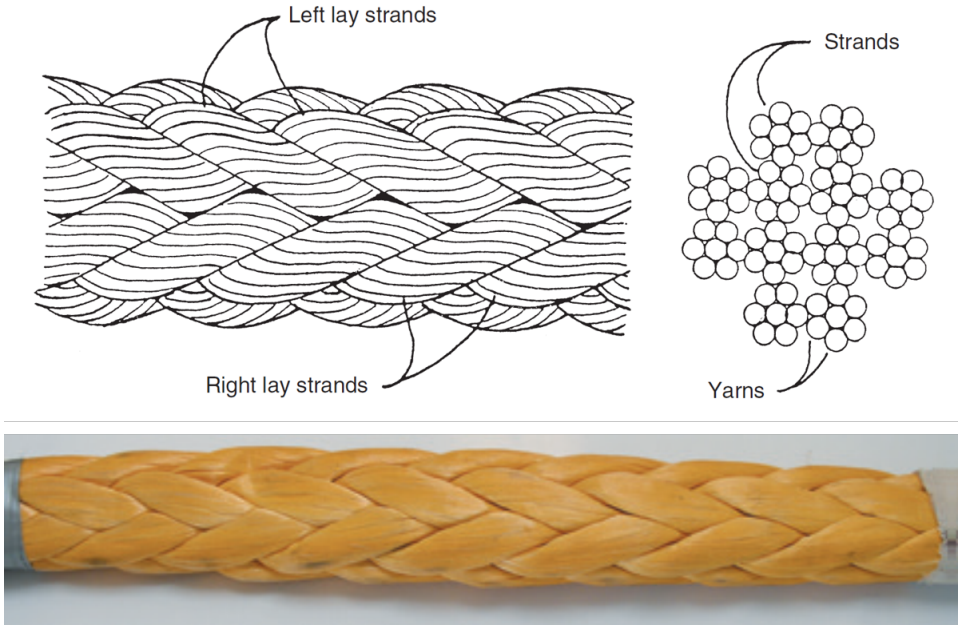


Figure 5.6: 12-strand braided, Dyneema fibre, 80mm diameter rope [24] [47]

| **Characteristics Dyneema** | | |
|---|---|---|
| Specific Gravity | 0.98 | |
| Density | 1.045 | kg/m^3 |
| Diameter | 0.08 | m |
| Weight | 3.58 | kg/m |
| Minimum breaking force | 4510 | kN |
| Elongation (of a new rope) at 100 % MBF | 3.5 | % |
| Melting point | ≈147 | °C |

Table 5.8: Dyneema Characteristics

### Strength and weight

Strength is important when considering rope properties, but fibre ropes would not nearly be so useful if their weight was not as low as it is. A comparison is made between a steel and HMPE rope with the same diameter in table 5.9. Dyneema is, like other HPME fibre rope, neutrally buoyant and has a specific gravity of 0.98. Specific gravity is the ratio between a material and water as given in equation 5.1.

$$SG_{Dyneema} = \frac{\rho_{Dyneema}}{\rho_{seawater}} \tag{5.1}$$

Here $SG_{Dyneema}$ is the specific gracity of Dyneema, $\rho_{Dyneema}$ is the density of Dyneema and $\rho_{seawater}$ the density of seawater.

| **Rope** | **Diameter [mm[** | **Minimum breaking load [kN]** | **Linear density in air [kg/m]** | **Linear density in water [kg/m]** | **Strength-to-weight ratio [kN/(kg/m)]** |
|---|---|---|---|---|---|
| **Steel wire** | 96 | 5591 | 44.10 | 38.4 | $1.267*10^2$ |
| **HMPE** | 96 | 5400 | 4.060 | floats | $1.330*10^3$ |

Table 5.9: Typical strength properties of steel and HPME rope [47]

### Stiffness

All fibre ropes have visco-elastic properties. This means that the material exhibits both viscous and elastic characteristics when undergoing deformation. Viscous materials have a strain rate that is dependent on time, where energy is dissipated (in the form of heat) when a load is applied. Elastic materials, however, do not dissipate energy when a load is applied and removed, which means that they will return to their original length once the applied stress is removed. This means that a visco-elastic rope will react differently when a load in applied fast (dynamic stiffness) or when the load is applied slowly (static stiffness). [8]. The stiffness and elongation of fibre ropes is strongly dependent on the macro-molecular structure of the material (or *morphology*), which is the way in which the molecules are organized when the fibre is produced. The morphology of fibre rope consists of crystalline and non-crystalline (amorphous) parts. HPME is produced by aligning up to 95% of the melted amorphous regular polyethylene and hereby maximising the crystalline part. The macro-molecular orientation of both HPME and PE are shown in Figure 5.7. The crystalline part has a high density, high strength and rigidity, whilst the non-crystalline part is weaker, looser and deforms easier [78]. These different characteristics play an important role in the stiffness characteristics of the rope [23].

- **Static Stiffness** is the stiffness of for instance a rope, when it is loaded slowly. This way it leaves time for both the non-crystalline and crystalline part to react to the load.
- **Dynamic Stiffness** is the stiffness response when it is cyclically loaded. The non-crystalline part does not have enough time to respond to the changing loading regime. Hence, the crystalline part takes on the load, resulting in a much stiffer response of the fibre. A rope is two to three times stiffer in dynamic loading conditions than in static loading conditions [22], [8] & [11].

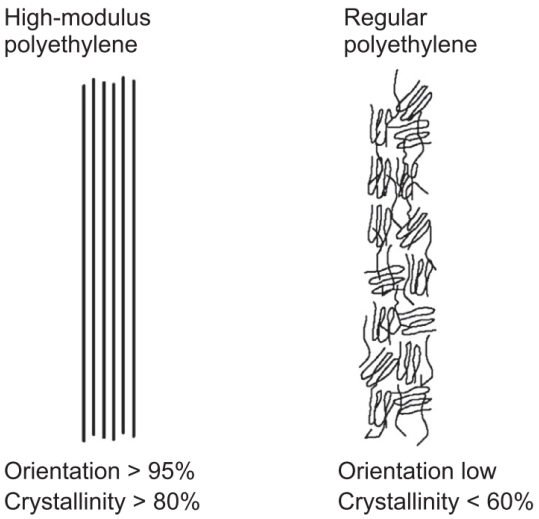


Figure 5.7: Macro-molecular orientation of HMPE and regular PE [78]

This complex behaviour of synthetic fibre ropes is subject of research within the offshore industry, mostly to be used as mooring lines [21]. As the mooring depth increases, the same incentives to use fibre ropes instead of steel wires are relevant as within deep-sea mining. For example, the disappearance of safe working load when using steel wires. With steel wires, the mooring system restoring force is partly due to its catenary weight. When using fibre ropes, the working principle of a mooring system is based on the tension versus the stretch characteristics of the rope [28]. There are many similarities between the loading of mooring lines and the ropes in this deep-sea mining concept, which allows the use of this knowledge in this thesis. J. Flory et al. [28] proposed a mechanical analog model of a typical fibre rope as seen in Figure 5.8. This model is oversimplified, as simple springs and dash-pots do not adequately represent the complex nonlinear and time dependent behaviour of the HPME ropes. Here it will be used as an illustration of the fibre rope, as it is a good representation and visualisation, which helps in the understanding of the rope behaviour. In this model it is possible to differentiate between the fibre material factors and constructional factors, contributing to the elongation. The structure of a new rope is relatively loose and uncompressed and the constructional factor is the elongation due to the first time(s) loading of this new rope.

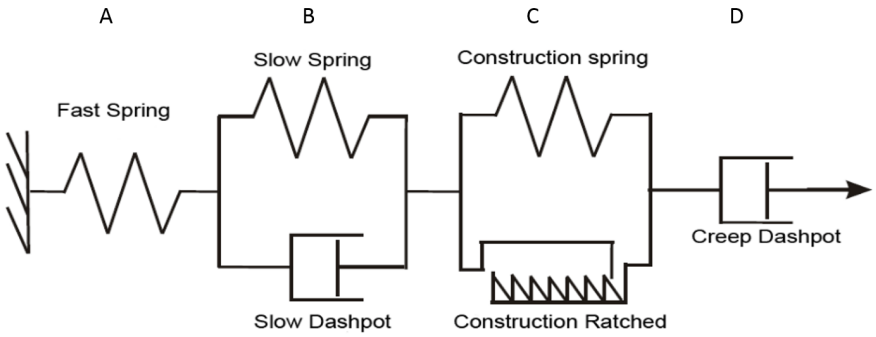


Figure 5.8: Spring-Dashpot model for prediction of HPME rope elongation [28]

- **A: Crystalline part** This spring represents the stiffness of the crystalline part, which acts when the rope is rapidly loaded. Its stiffness is dependent on multiple factors as the mean load level and the load amplitude.
- **B: Amorphous part** This parallel spring-dashpot system works when the rope is slowly tensioned and the amorphous part of the fibers have time to react. The total stretch of the rope is the summation of the fast and slow spring stretch. The delayed responses between the applied load and the resulting extension causes hysteresis. This is further discussed in Section 5.2

- **C: Rope construction stretch**The process of first tensioning a new rope, causing the various yarns and strands to compact and realign, is called bedding-in. As a result the rope elongates and this length increase is called constructional stretch in this model. It is represented by a ratcheting device. Once a the constructional stretch has taken place, this length increase can not be undone. Whenever a higher tension is applied, this spring-ratchet system stretches even further. This will be further discussed in Section 5.2.
- **D: Creep** is the extension of a rope under constant load. The creep is typically rapid at first but will become linear with time. It will be discussed in further detail in Section 5.2

Due to the visco-elastic properties, defining the stiffness of fibre ropes is much more complex than for steel wire ropes, as it depends on more parameters [22]. This includes the loading history, the mean load level, the load amplitude and the loading rate. In general, fibre ropes becomes stiffer when it experiences more load cycles. This can also be seen with the reference Dyneema rope in Figure 5.9.

Stiffness is defined as the resistance offered by an elastic body to deformation when a force is applied. For an elastic body with a single degree of freedom the stiffness is expressed by the following equation 5.2

$$k = \frac{F}{\Delta L} \tag{5.2}$$

where

- F is the applied force [N]
- $\Delta L$ is the elongation [m]

The stiffness, however, is depended on the material, cross section and length of the elastic body (rope in this case), as seen in equation 5.3

$$k = \frac{EA}{L_0} \tag{5.3}$$

where

- E is the elastic modulus [$kg \cdot m^{-1} \cdot s^{-2}$]
- A is the cross-sectional area [$m^2$]
- $L_0$ is the initial length of the rope [m]

With these two equations, the axial stiffness (EA) can be calculated, which is independent of the length of the rope, as is seen in equation 5.5. It is dependent on the dimensionless strain, which is the proportional deformation and can be calculated by dividing the change in length by the initial length, as seen in equation 5.4

$$\varepsilon = \frac{\Delta L}{L_0} \tag{5.4}$$

$$EA = \frac{F}{\varepsilon} \tag{5.5}$$

where

- $\varepsilon$ is the strain [-]
- EA is the axial stiffness [kN]

Figure 5.9 shows the Dyneema elongation as a function of the minimum breaking force as provided by the rope manufacturer [24]. These mechanical properties have been determined according to ISO 2307:2005, which means the rope has been tested on a tensile testing machine, slowly increasing the force until it breaks. The strain with the corresponding force has been measured to get the strain as a function of the MBF as shown in Figure 5.9. Due to the slow loading, the static stiffness is presented.

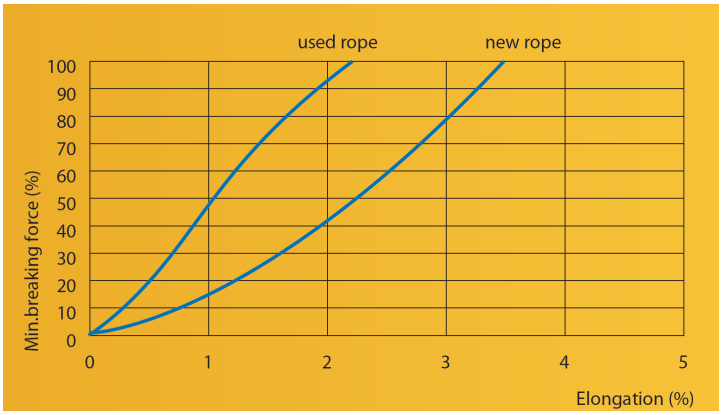


Figure 5.9: Dyneema elongation from the manufacturer catalogue [24]

The ropes during deep-sea mining operations will typically experience a steady mean load and dynamic loads around the mean load due to for example waves. The stiffness of the rope will react differently on the dynamic loads. As stated earlier, the stiffness of a dynamically loaded rope can be two to three times higher than a rope in static loading conditions. The dynamic stiffness is also subject to change in different loading conditions. In research [21], the influence of the loading parameters (mean load and load period) on dynamic stiffness is discussed. A HPME fibre rope is loaded with a period of 10s, to simulate the wave frequency. The mean load influence is shown in Figure 6.10(a) and Figure 6.10(b) shows the values normalized with respect to the 10% mean load value. This shows that an increase in the mean load up to 40% can load to an increase in dynamic stiffness of 25% for HPME.

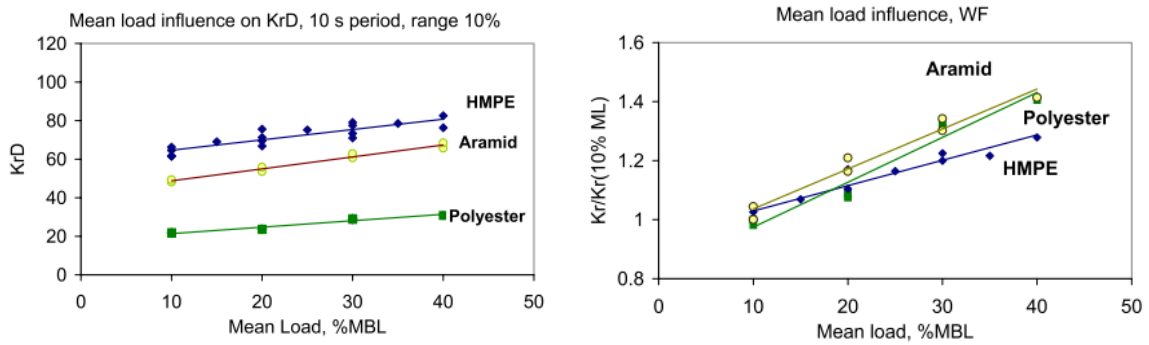


(a) Influence of mean load, wave frequency

(b) Influence of mean load, normalized with respect to 10% KrD value

Figure 5.10: Influence of mean load, results from tests done by Davies et al. [21]

## Elongation

As a result of a force on the rope, the rope will stretch. The elongation is provided by the manufacturer of the rope as a percentage of the MBF (minimum breaking force). For simplicity a constant EA is assumed. This is calculated using equation 5.5 and the 100 %MBF with the corresponding strain as in equation 5.6. This leads to a axial stiffness of $1.29 * 10^5 kN$.

$$EA = \frac{F_{100\%MBF}}{\varepsilon_{100\%MBF}} \tag{5.6}$$

As stated in Section 3.3 the weight of the skip will increase while loading. It is desirable to keep the docking unit as statically loaded as possible so it remains horizontal. This means that the two winch wires attached to the skip are responsible for the carrying of the increasing load, while keeping it at a constant elevation. The tension in the wires will increase and therefore the wires will elongate. To account for this elongation,

the wires need to spool in during the loading of the skip.

$$\Delta L = Ls - L_0 \tag{5.7}$$

where $\Delta L$ is the elongation, $L_s$ is the stretched length and $L_0$ the initial length. As the total length of the rope must remain the same, the initial length decreases as the weight and therefore the elongation increases.

$$L_0 = \frac{L_s}{\frac{F+w}{EA}+1} \tag{5.8}$$

Here $w$ is the submerged weight of the total rope. As the considered Dyneema rope is buoyant in water, the submerged weight of the rope is negative and the rope will experience an upward force (buoyancy). Dyneema is has a density that is a small portion lower than seawater, so this self weight is very small. The tension and elongation as a function of the filling rate can be seen in Figure 5.11. In this calculation a $L_s$ of 5960m is assumed. During the loading, the rope elongation increases from 9m (due to the weight of the empty skip) to 51m with a fully loaded skip, which is an increase of 0.87 % of the initial length.

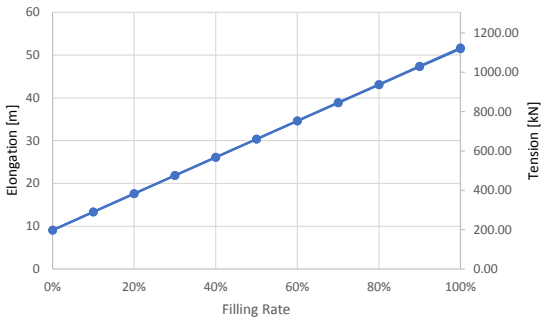


Figure 5.11: Elongation as function of fill rate skip

### Rope construction stretch

If a new rope is loaded for the first time, permanent extension of the rope occurs due to re-orientations of the crystallites in line with the stress direction , which can be thought of as a ratchet as shown in Figure 5.8 [79]. This re-orientation occurs at both molecular level and at rope construction level, as the fibers, yarns and strands re-align [22]. The permanent residual strain and the corresponding increased stiffness is known as bedding-in of the rope. This phenomena has been tested in laboratory tests to investigate the mechanical behaviour of HPME and aramid fibre ropes. Results are shown in Figure 5.12, where the distinction between fibre and rope construction re-alignment is clearly visible, as the strain within the rope is higher than with a individual fibre. Figure 5.13 shows a stabilisation of the stiffness after the ropes have been subjected to 100 cycles in the 10-30% MBF range. The strain in the x-axis is with respect to the new, elongated, length of the stretched rope. The hysteresis loop shown in this figure shows the damping of HPME and is further discussed in Section 5.2.

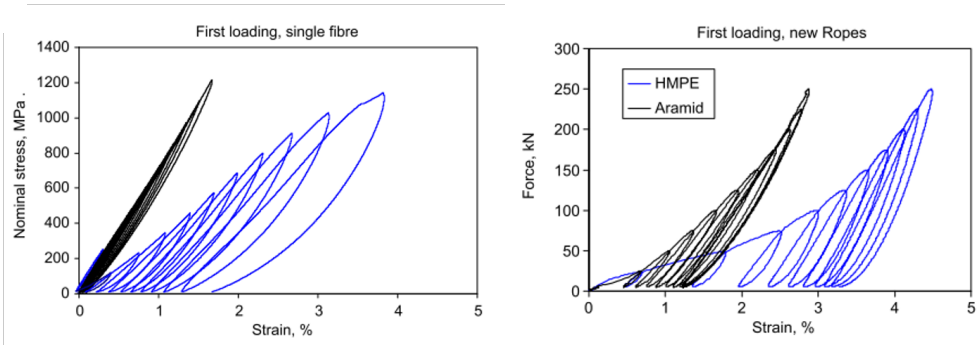


(a) First loading cycles of a single fibre

(b) First loading cycles of a new rope

Figure 5.12: First Loading cycles of HPME fibres and new rope [22]

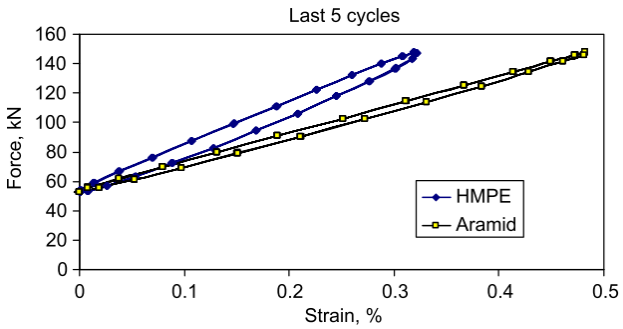


Figure 5.13: Cycling to stabilise rope stiffness at 10–30% MBL

### Damping

Due to the visco-elastic properties of the fibre in the rope damping will occur. Part of the energy is stored in strain due to the elastic properties and part of the energy is dissipated as heat due to the viscous properties. The amount of energy dissipated by the rope during one cycle of loading is called hysteresis. The damping of a fibre can be simplified by isolating the parallel spring-dashpot system from Figure 5.8 as seen in Figure 5.14(b). Again this is a highly simplified model that is only really accurate for linear visco-elastic materials [47], but even for more complex responses, the idealised model can be used to get insight in the behaviour of the fibres. The elastic element (modelled by the spring) gives an in-phase reaction to applied force F, while the viscous element (modelled by the dashpot) gives an out-of-phase reaction. During cyclic loading the load will change with $\Delta\sigma$ and elongation with $\Delta\epsilon$, as illustrated in Figure 5.14(a).

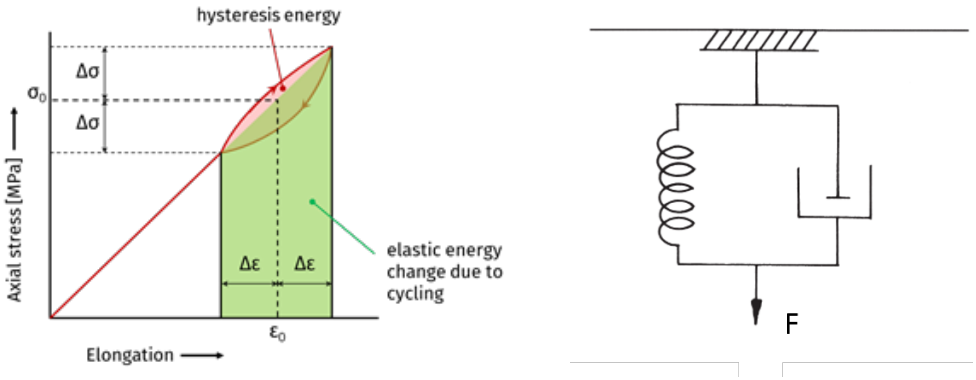


(a) Typical hysteresis graph [47]

(b) Parallel spring-dashpot model

Figure 5.14: Damping due to hysteresis

The dissipation of energy per cycle is given by the area in the top right of Figure 5.14(a) and is equalled by equation 5.9, which can be separated in elastic energy (equation 5.10 and relative energy loss per cycle (equation 5.11).

$$\Delta E_{hyst} = \pi k_{RS} \Delta x^2 \tan(\delta) \tag{5.9}$$

$$E_{\text{elast}} = \frac{k_{RS} \Delta x^2}{2} \tag{5.10}$$

$$\frac{\Delta E_{\text{hyst}}}{E_{\text{elast}}} = 2\pi \tan(\delta) \tag{5.11}$$

where

- $\Delta$ x is the rope elongation amplitude [m]
- $K_{RS}$ is the storage rope stiffness [N/m]
- $\delta$ is the loss angle [-]

To investigate what this means for the damping in the ropes in this deep-sea mining concept, calculations have been done with the dyneema characteristics in table **??**. In these calculations, linear visco-elastic behaviour in assumed, the effect of rope construction/internal friction and the air/drag resistance is neglected. To simulate the dissipation of energy of a free hanging skip, a decay test is set up as shown in Figure 5.15. A decay test means that a mass in suspended from a spring (rope), given an initial offset and elongating the spring, release the mass from its offset and see how long/how many cycles it takes to damp out. The energy that is dissipated per cycle is due to hysteresis.

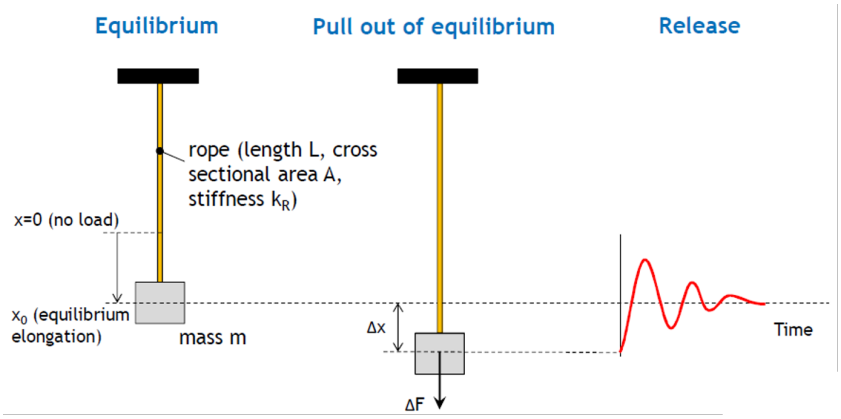


Figure 5.15: Decay test set-up: Vibration damping

An estimate of number of cycles required to dissipate 95% of the elastic energy can be made with equation 5.12. From equation 5.12 and 5.11, it can be seen that this dissipation of energy is only dependent on the loss angle and not on for instance the length of the rope or the mass, in this simplified situation. In table **??** it can be seen that the loss angle is highly depended on the temperature of the rope, ranging from 0.02 at 0°C to 0.1 at 60°C. The energy dissipation by hysteresis as a function of the temperature is shown in Figure **??**. The temperature of the deep seawater (and therefore the majority of the rope length) is very low (around the 1-2 °C), as is shown in Figure 5.20(b).

$$n = \frac{\ln(0.05)}{\ln(1-2\pi\tan(\delta))} \tag{5.12}$$

But as stated before, this only includes the hysteresis damping of the fibre and neglects the effect of rope construction and internal friction damping. After the rope has been loaded for the first time and the stiffness is stabilized as shown in Figure 5.12 and 5.13, the effects of rope construction are permanent and don't influence the damping anymore [22]. There is little in-field data on the internal damping of synthetic fibre ropes. Research has been done (Weller et al. [79] performed decay experiments on nylon ropes, which is not useful when focussing on HPME), but it is very scarce. As stated in *Handbook of fibre rope technology* by McKenna (2004) [47] when discussing the longitudinal axial damping factors: "Data is not currently available on the energy absorbed by the other modes of internal damping (bending, shearing and torsional) of fibre ropes, but these modes are considered to be the least significant." Presumably this data gap is due to the combination of complex nonlinear behaviour and the influence of the composition of the rope, which is different for every rope manufacturer.
However, to improve the understanding of damping behaviour of fibre ropes, a novel method is proposed by Yushun Lian et al. [43] for calculating the internal damping coefficient of fibre ropes, based on structural dynamics theory. By comparing damping values from experimental data (calculated with the 'indicator diagram' method, which utilizes the area of the hysteresis loop curve at the top of mooring line to describe the dissipated energy caused) to the proposed method, a relation between the internal damping coefficient and the dynamic stiffness is shown. They deem that a rope element can be modelled as a single degree of freedom (SDOF) system based on the theory of structural dynamics. By presenting normalised stress and strain, results of the tested samples can also be applied to larger sized ropes. For more information about this introduced method, the reader is referred to the paper by Lian et al. [43].

For this research the experimental results of the research by Lian et al. [43] are most interesting. The results of the experimental tests and the comparison with the theory of structural damping (TSD) are show in Figure 5.16. The mean tension of cyclic loads $L_m$ and the load amplitude $L_a$ are selected at relatively high loading ranges (60-70 % average breaking strength (ABS)), as the experimental set-up provides more stable and accurate results and to simulate high sea state conditions. The stiffness is given by $K_r$. The damping coefficient derived from the experiments is given by $\eta$(IDM) and is compared to the damping coefficient derived from the theory of strucutral dynamics $\eta$(TSD) In the deep-sea mining concept, with the chosen

Dyneema rope, the expected $L_m$ is lower, namely around the 25% for a full skip. The experimental results of HMPE ropes show that the internal damping coefficient increases with increasing mean load and decreases with increasing load amplitude and load periods of fiber ropes. This does not coincide with the earlier stated remark that the dissipation of energy is independent of the mass. That remark applied to the internal damping of single fibres, not the internal damping of rope consisting of Dyneema fibres. This means that to get a realistic value for the internal damping coefficient in the case of the deep-sea mining operations, experimental tests need to be done with relevant parameters such as mean load, load amplitude and periods.

| Case | $L_m$ (% ABS) | $L_a$ (% ABS) | Period (s) | $K_r$ | $\eta$(IDM) | $\eta$(TSD) | Relative error |
|---|---|---|---|---|---|---|---|
| 1 | 60 | 5.75 | 1.9288 | 83.52 | 9.84 | 10.12 | 2.81% |
| 2 | 65 | 5.75 | 1.9288 | 86.09 | 10.30 | 10.39 | 0.87% |
| 3 | 70 | 5.75 | 1.9288 | 89.22 | 10.43 | 10.66 | 2.24% |
| 4 | 60 | 11.50 | 1.9288 | 75.13 | 9.23 | 9.29 | 4.06% |
| 5 | 65 | 11.50 | 1.9288 | 79.14 | 9.37 | 9.31 | 0.57% |
| 6 | 70 | 11.50 | 1.9288 | 83.15 | 9.45 | 9.61 | 1.72% |
| 7 | 60 | 17.66 | 1.9288 | 73.71 | 8.90 | 9.21 | 3.48% |
| 8 | 60 | 17.66 | 2.8270 | 70.73 | 7.74 | 7.93 | 2.51% |
| 9 | 60 | 17.66 | 3.6880 | 69.41 | 6.78 | 7.12 | 5.01% |

Figure 5.16: Comparison results of internal damping coefficients with different method for HMPE ropes

## Creep

A major issue with HPME is its tendecy to creep [8]. Creep is the extension of a rope under constant load. The extension can potentially lead to failure, especially as HPME has a high creep rate. Figure 5.17 shows the typical HPME creep curve. Three regimes can clearly be distinguished in this curve, which all show a different behaviour [77].

- **Regime I: Primary Creep**: In this first regime the non-crystalline realignment takes place. It starts with a high creep rate that flattens to an almost constant strain at the end.
- **Regime II: Steady State Creep**: In this regime the sliding of molecular chains takes place. The elongation in this regime is irreversible and is called plastic creep. The creep rate slightly increases over time.
- **Regime III: Tertiary Creep**: In this regime molecular chains start to break. The strain rate will increase exponentially and these high strains will start to cause necking, tensile deformation, in the fibres. This will decrease the effective area of the rope while the tension remains. This will accelerate the creep deformation and eventually lead to material fracture.

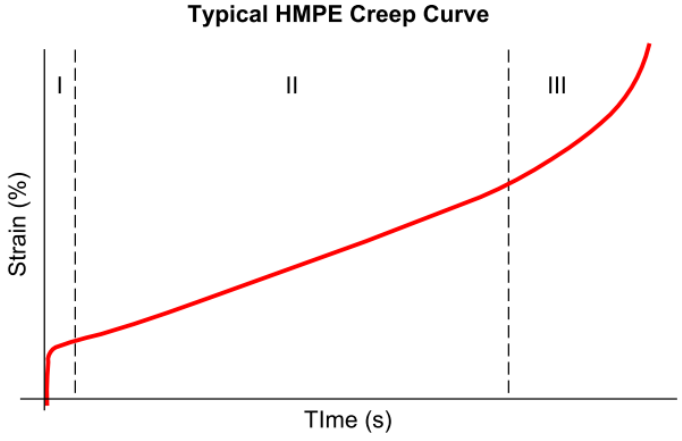


Figure 5.17: Typical HPME creep curve

In an article describing the mechanical behaviour of HPME fibre ropes in deep sea operations [22], creep tests were performed. Instead of measuring the creep over a time span of several days as is seen in most creep tests, here the tests were limited to a 6-hour constant load creep period followed by removing

the load and a 6-hour recovery period before increasing the creep load to the next level. This to simulate the deep-sea handling operations, which are mostly limited to a few hours. In this deep-sea mining concept the period of operation is about 5 hours for the hoisting and lowering of the skip and can be up to weeks for the guidance wires. Figure 5.18 shows the measured creep strain values for HPME and Aramid (another synthetic fibre rope material) defined as the total increase in strain between reaching the creep load and the start of the unloading [22]. It can be seen that the creep reaches values up to 0.5 %.

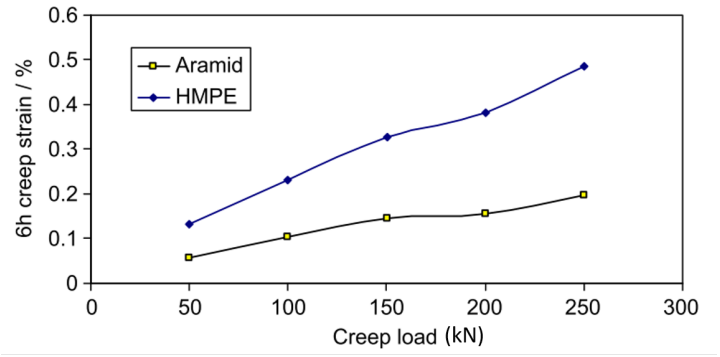


Figure 5.18: Creep strain values for 6 h periods at different load levels, 20 °C

Creep is especially a problem with long-term sustained loading, but in many applications it may not be a problem. Creep, elongation and fatigue of the ropes must be checked extensively during operations, to be able to guarantee a continuous operation. This can be done by visual checks of the ropes and comparing the elongated length of the ropes each cycle. Permanent elongation can also be a problem for the handling of the SPT. The skips need to be fitted in the docking unit with a decent amount of caution to prevent high clashing forces. This could happen if the rope length deviates from the expected length. In practice, these problems can be prevented with for instance a camera connection to the PSV or distance control sensors. As the work is done 6000 meters below the control room at the PSV, it is recommended to have adequate control support to sustain a controlled handling at the seabed.

## 5.3. Hydrodynamic Characteristics

Due to the velocity of the deep-sea mining system and the current that is present in the ocean, fluid will flow around the immersed bodies. Bodies above water are subject to (gaseous) fluids that flow around them, namely air. But the only focus will be on the hydrodynamic interaction and therefore the subsurface bodies.

### Reynolds Number

A parameter describing the viscous behaviour of a fluid stream around a cylinder is the dimensionless Reynolds number, which is given in equation 5.13 [80]. The second form can be derived due to the ratio between the dynamic viscocity $\mu$ and the density $\rho$, called kinematic viscocity $\nu$ as stated in equation 5.14.

$$\mathrm{Re} = \frac{\rho u L}{\mu} = \frac{uD}{\nu} \tag{5.13}$$

$$\nu = \frac{\mu}{\rho} \tag{5.14}$$

where

- $u$ is the speed of the fluid relative to the object [m/s]
- $D$ is the diameter of the cylinder [m]
- $\nu$ is the kinematic viscocity [$m^2/s$]
- $\mu$ is the dynamic viscocity [$kg \cdot m^1 \cdot s^1$]
- $\rho$ is the density of the fluid [$t/m^3$]

The Reynolds number contains information about the fluid flow around immersed bodies. In Figure 5.19 the flow regimes around a smooth cylinder as a function of the Reynolds number is shown. At very low Reynolds numbers, the flow follows the cylinder contours and join back together in the wake of the cylinder. This is called laminar flow. [80]. Many research and experiments have been done over the years to try and capture the flow around a cylinder and the Reynolds number at which it transitions to another flow regime, which is summarized in Figure 5.19 [57] [36]. In the low Reynolds number range, between 45 and 150, the flow separates at the back of the cylinder forming regular vortices. Between the Re = 150 and 300, the vortices that are breaking away from the cylinder become more turbulent, while the boundary layer on the cylinder remains laminar [69]. The Reynolds number range between 300 and $1.5*10^5$ is called the subcritical range. At a even higher Reynolds number, $1.5*10^5 < \mathrm{Re} < 1.5*10^6$ , the cylinder boundary layer becomes turbulent and the separation points move aft. This is called the transition range and here the cylinder drag coefficient, discussed in Section 5.3, drops significantly. At the supercritical range, $\mathrm{Re} > 1.5*10^6$, the vortex street is fully turbulent but regular vortex shedding is re-established.

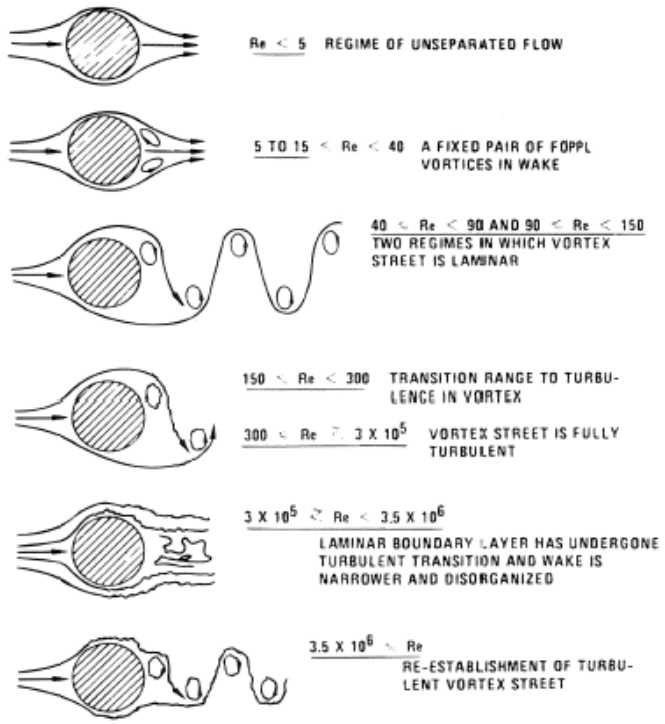


Figure 5.19: Regimes of fluid flow across smooth circular cylinders [12]

With equation 5.13, it is possible to determine the Reynolds number for multiple combinations of current velocity, diameter and viscocity. The Reynolds number is later on used to estimate drag coeffients (introduced in the next section) of different components of the mining system. As discussed in Section 4.1, the current is variable over the depth, ranging from 0.1 to 1 m/s. The diameter of the cylinder $D$ in equation 5.13 is the diameter of the skip or the diameter of the wires. The viscocity is depended on the temperature of the water and the salinity. In this case the vertical distribution of the salinity as given in Figure 4.6 is used as reference. It can be seen in Figure 5.20(a) that the viscocity is decreasing with an increasing temperature. As seen in Figure 4.6, the ocean water temperature in the CCZ will decrease rapidly to a constant 1-4 °C. The monthly mean temperature (2014-2018) from the reference location in the CCZ, extracted from a netCDF file (the same data file that was used for the current), can be seen in Figure 5.20(b). For further calculations of the Reynolds number, a constant temperature of 2.5 °C is assumed. This gives a kinematic viscocity of $1.71 * 10^{-6} m^2/s$.

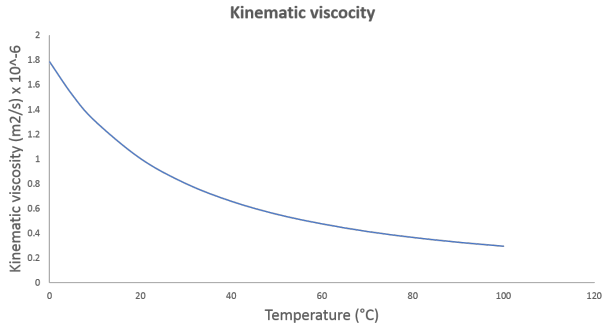


(a) Kinematic viscocity of salt water; it is dependent on temperature [62]

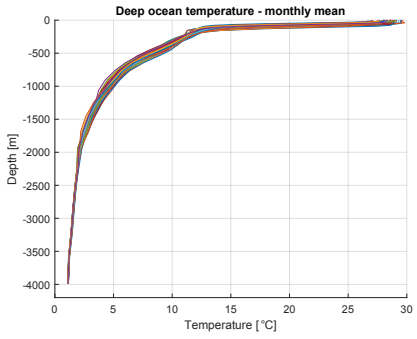


(b) Montly mean temperature in the Clarion clipperton zone

Figure 5.20: Temperature dependency of kinematic viscocity of seawater

## Drag

The flow disturbance as described in the previous section results in a drag force. It is by definition parallel to the direction of the flow direction. This drag force is given by the following equation 5.15.

$$F_D = \frac{1}{2}\rho u^2 C_D A \tag{5.15}$$

where

- $\rho$ is the density of the fluid $[t/m^3]$
- $u$ is the speed of the fluid relative to the object [m/s]
- $C_D$ is the drag coefficient [-]
- $A$ is the reference area $[m^2]$

The drag coefficient is a great uncertainty in this drag force calculation. Many research and experiments have been done over the years, which is normally summarized in lookup tables as found in DNV-RP-H103 [59], Hoerner's Fluid Dymamics [35] or Fluid Mechanics by Frank White [80] as seen in Figure 5.21. This figure shows the drag coefficient of a cone with different angles and a short smooth surface cylinder with different length/diameter ratios in laminar flow. The length/diameter ratio of the ropes is very large (small diameter, great length) so the drag coefficient of the ropes is assumed to be 1.2.

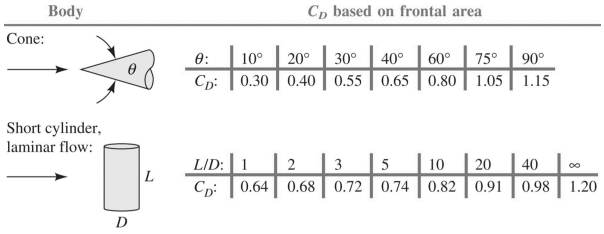


Figure 5.21: Drag coefficient for three-dimensional bodies at Re > $10^4$ [80]

The cylinder shape is an important one within the offshore sector, as many components are round (risers, wires, piles etc.). Also in this concept, most drag forms around cylinders, such as the skips and the ropes. In Figure 5.22 the empirical determined relationship between the Reynolds number and the drag coefficient of a smooth cylinder is shown. It can be seen that the earlier described *transition range*, $10^5 < Re < 10^6$, causes a halving of the drag coefficient. As stated earlier, the Reynolds number is depending on the relative current velocity. In Section 4.1, it is discussed that the current is not constant over the depth (and time), which means that the Reynolds number of the ropes is not constant over depth and that the Reynolds number of the skip is depended on the position of the skip in the waterline (typically the surface current velocity is a lot higher than the deep sea current). Assuming a current velocity between the 0.1 and 1 m/s, this results in a Reynolds number of a skip between the $3.4 * 10^5$ and $3.4 * 10^6$. As seen in Figure 5.22 this is within the transition range.

| | **Current Velocity** | | |
|---|---|---|---|
| **Component** | 0.1 | 1 | [m/s] |
| **Skip** | 3.45 E5 | 3.45 E6 | [-] |
| **Ropes** | 4.68 E3 | 4.68 E4 | [-] |

Table 5.10: Reynolds numbers

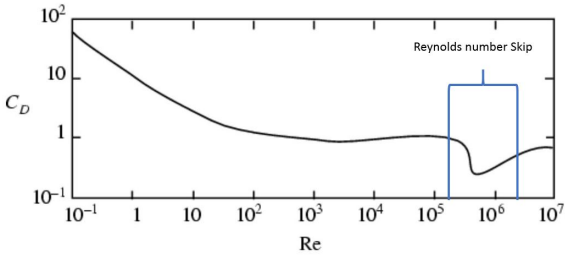


Figure 5.22: Drag coefficient for a smooth cylinder [80]

Clauss [17] suggests the drag coefficient $C_D$ and inertia coefficient $C_M$ of a smooth cylinder as seen in Figure 5.23.

| $Rn < 10^5$ | | $Rn > 10^5$ | |
|---|---|---|---|
| $C_D$ | $C_M$ | $C_D$ | $C_M$ |
| 1.2 | 2.0 | 0.6 | 2.0 |
| 1.2 | 1.5 | 0.6 | 1.5 |

Figure 5.23: Drag coefficient for a smooth cylinder as proposed by Claus [18]

In 2018 a numerical investigation on the drag coefficient of a finite length, circular cylinder with two free ends [29] has been done, from which a sketch is shown in Figure 5.24(a). The drag coefficient as a function of the Reynolds number of a 3D cylinder with a length/diameter ratio of 1.5 is shown in Figure 5.24(b). This shows great similarities with the skip in the deep-sea mining concept, as the skip has two free ends when being hoisted/lowered and has a length/diameter ratio of 10/6. This research agrees with the proposed drag coefficient of 0.6 by Clauss [17].

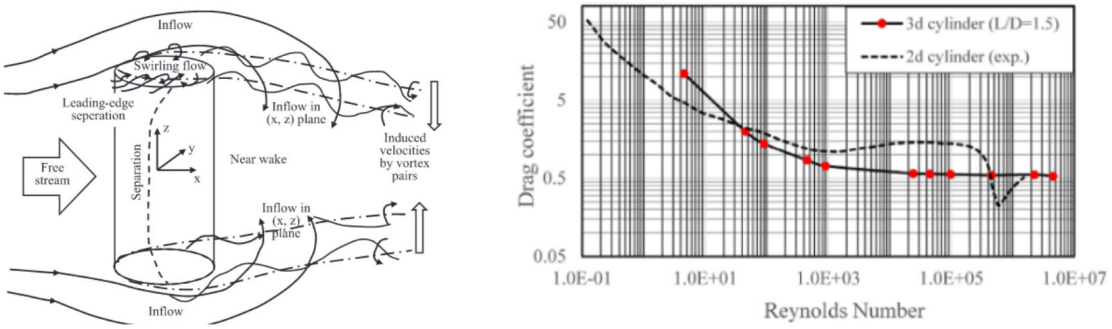


(a) Sketch of flow around a circular cylinder

(b) Drag coefficient of circular cylinder with two free ends as shown in Figure 5.24(a)

Figure 5.24: Drag around a 3D cylinder with two free ends [29]

Drag occurs to relative speed of the water around a body, which means that a skip that is lowered or hoisted also experiences drag. Lowering or hoisting of the skip gives a different drag coefficient, as it is depended on the shape. This difference in shape is illustrated in Figure 5.25(a) and the corresponding drag coefficients can be derived from Figure 5.25(b). The derived values can be found in table 5.11.

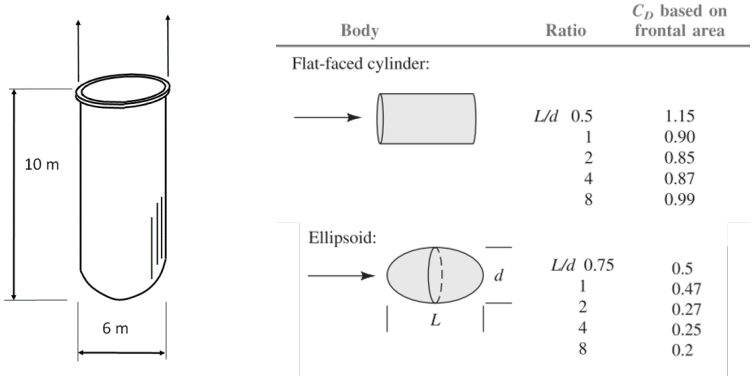


(a) Sketch of a skip

(b) Drag coefficient of different circular shapes [80]

Figure 5.25: Drag on different sides of the skip

This results in the following drag coefficients for the different components in the deep-sea mining concept. The drag coefficients for the harvester, ladder and docking unit are set to 1 in all directions, which is similar to the drag coefficient of a truck [80]. As the final design of these components is unknown, it is

redundant to get a more detailed drag coefficient. When the shape of these components is known, more research on the drag coefficient is recommended, for example with a CFD model or experiments. This also applies for the skip, as it won't be a smooth cylinder, as it will have attachments as the eyelets etc. In this stage educated approximations can be made and these are shown in the table below.

| **Component** | **Drag Coefficient** | | |
|---|---|---|---|
| | x | y | z |
| **Harvester** | 1 | 1 | 1 |
| **Ladder** | 1 | 1 | 1 |
| **Docking Unit** | 1 | 1 | 1 |
| **Lowering Skip** | 0.6 | 0.6 | 0.35 |
| **Hoisting Skip** | 0.6 | 0.6 | 0.87 |
| **Rope** | 1.2 | 1.2 | - |

Table 5.11: Drag coefficients of the components

### Drag on an inclined rope

Drag is calculated parallel to the direction of the relative velocity of the fluid. A rope will experience an inclination when offset occurs due to drag. This results in two relative current velocity vectors, one perpendicular to the rope and one parallel along the rope as seen in equation 5.16 and 5.17 and visualised in Figure 5.26.

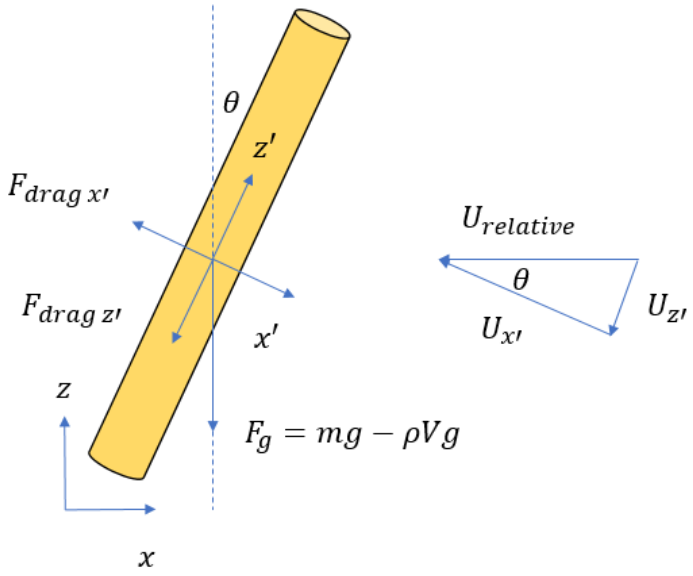


Figure 5.26: Forces on an inclined cylinder

$$U_{x'} = U_{\text{rel}} * \cos(\theta) \tag{5.16}$$

$$U_{z'} = U_{\text{rel}} * \sin(\theta) \tag{5.17}$$

This results in the following drag equations 5.18 and 5.19. As is shown in Figure 5.21, the perpendicular drag coefficient ($C_{D-x}$) for a cylinder that has a very high L/D ratio, like a rope, is 1.2. The parallel drag coefficient ($C_{D-z}$) is the skin friction coefficient, which is a about 0.01.

$$F_{\text{Drag } x'} = \frac{1}{2}\rho * C_{D-x} * A_{x'} * U_{x'}^2 \tag{5.18}$$

$$F_{\text{Drag } z'} = \frac{1}{2}\rho * C^*_{D-z} A_{z'} * U^2_{z'} \tag{5.19}$$

This results in the following equations 5.20 & 5.21 for the total force on a single rope element in $x$ and $z$ direction. The influence of the drag force along the rope is very low due to the low skin friction coefficient. Due to this, the drag on an inclined rope can get substantially lower.

$$F_x = -F_{\text{Drag } x'} * \cos(\theta) - F_{\text{Drag } z'} * \sin(\theta) \tag{5.20}$$

$$F_Z = +F_{\text{Drag } x'} * \sin(\theta) - F_{\text{Drag } z'} * \cos(\theta) - F_g \tag{5.21}$$

**Fall Velocity**

The fall velocity is a equilibrium between the submerged weight of a body and the drag force of the surrounding water on the body. This is captured in the following equation:

$$W_{\text{skip};e} = C_{Dz} A_{\text{skip;z}} \cdot \frac{1}{2}\rho V_f^2 \tag{5.22}$$

where

- $W_{\text{skip};e}$ is the submerged weight of the empty skip [N]
- $\rho$ is the density of the fluid $[t/m^3]$
- $A_{\text{skip;z}}$ is the surface of the skip $[m^2]$
- $C_{Dz}$ is the drag coefficient [-]
- $V_f$ is the fall velocity [m/s]

The maximum payout velocity of the winch for the lowering of the skip is equal to the fall velocity, as a higher pay out velocity will result in slack wires. This maximum velocity can be derived with equation 5.22.

$$V_f = \sqrt{\frac{W_{\text{skip};e}}{\frac{1}{2}\rho C_{Dz} A_{\text{skip;z}}}} \tag{5.23}$$

With the drag coefficient of the skip when lowering as determined in Section 5.3, the maximum lowering velocity becomes 5.57 $m/s$. As stated in Section 3.3, the lowering velcity will be 2 $m/s$, so no problems are expected. With regards to the fall velocity, the lowering velocity could even be increased if a shorter production cycle time is desired.

**Mass moment of Inertia**

To be able to simulate the behaviour of the different components, the extent to which the body is able to resist a rotational acceleration around a certain axis, the mass moment of inertia, needs to be determined.

The mass moment of inertia of the simplified skip is determined with the following formulas, where R is the radius of the skip (3m) and l is the height of the skip (10m) :

Thin walled hollow cylinder:

$$I_z = mR^2 \tag{5.24}$$

$$I_x = I_y = \frac{1}{12} m(6R^2 + l^2) \tag{5.25}$$

Solid cylinder:

$$I_z = \frac{1}{2} mR^2 \tag{5.26}$$

$$I_x = I_y = \frac{1}{12} m(3R^2 + l^2) \tag{5.27}$$

To determine the mass moment of inertia of a multi-body object, Steiner's theorem must be applied. This theorem can be used to determine the mass moment of inertia of a body about any given axis. This

is shown in equation 5.28, where $m$ is the mass of the body, $I_X$ is the mass moment of inertia around an axis and $d$ is the distance between this axis and the axis about which the mass moment of inertia $I_A$ is determined. It says that the total mass moment of inertia is the sum of the mass moments of inertia of the different bodies + the mass of the body times the distance squared of the center of the body to the centre of mass of the combined body and/or the point of rotation.

$$I_A = I_X + m * d^2 \tag{5.28}$$

The mass moment of inertia of the simplified skip can be approached by a combination of several bodies as can be seen in Figure 5.27, (1) the thin walled cylinder with mass $m_1$ (2) the bottom plate with mass $m_2$ and in case of the filled skip (3) the nodules with mass $m_3$ . For the calculation of the mass moment of inertia these are combined in the following way:

$$I_z\ emptyskip = m_1 R^2 + \frac{1}{2} m_2 R^2 \tag{5.29}$$

$$I_{x,y}\ emptyskip = \frac{1}{12} m_1 (6R^2 + l^2) + \frac{1}{2} m_2 R^2 + m_2 * d^2 \quad with \quad d = \frac{1}{2} l \tag{5.30}$$

$$I_z\ fullskip = m_1 R^2 + \frac{1}{2} m_2 R^2 + \frac{1}{2} m_3 R^2 \tag{5.31}$$

$$I_{x,y}\ fullskip = \frac{1}{12} m_1 (6R^2 + l^2) + \frac{1}{2} m_2 R^2 + m_2 * d^2 + \frac{1}{12} m_3 (3R^2 * l^2) \quad with \quad d = \frac{1}{2} l \tag{5.32}$$

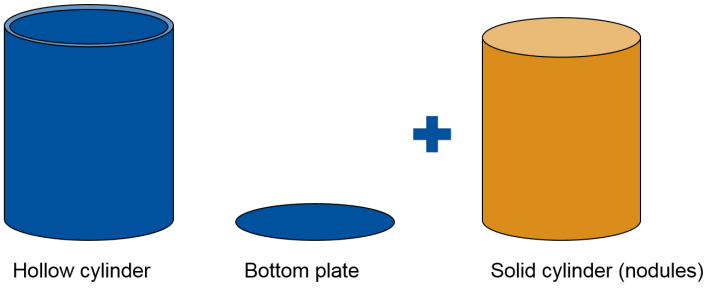


Figure 5.27: Visualization of mass moment of inertia build-up of a full skip

The harvester, ladder and docking unit will be simplified, again due to the fact that the final shape of these components is unknown. They will be considered as square boxes with the dimensions as given in Section 5.1. The mass moment of inertia around each axis is calculated with the following equations:

$$I_x = \frac{1}{12} m\left(y^2 + z^2\right) \tag{5.33}$$

$$I_y = \frac{1}{12} m\left(x^2 + z^2\right) \tag{5.34}$$

$$I_z = \frac{1}{12} m\left(x^2 + y^2\right) \tag{5.35}$$

### Added mass

Submerged bodies experience the surrounding fluid as an added mass when accelerated. Together with their own mass, the surrounding fluid' mass must also be moved. The added mass is given by the following equation 5.36 as provided by the DNV [59].

$$m_A = \rho \cdot C_A \cdot V_R \tag{5.36}$$

where

- $\rho$ is the density of the surrounding fluid [$kg/m^3$]
- $C_A$ is the added mass coefficient [-]
- $V_R$ is the reference volume [$m^3$]

Table 5.12 shows the added mass of the skip. For the full skip, the mass of the internal water is already included in the mass of the content in Section 5.1.

| **Component** | **Direction** | | | $C_a$ [-] | $V_r$ [$m_3$] | $M_a$ [t] | $M_a total$ [t] |
|---|---|---|---|---|---|---|---|
| Skip | x | Empty | Surface | 0.72 | $\pi r^2 l$ | 209.94 | |
| | | | Content | 1 | $\pi r^2 l$ | 282.74 | |
| | | | | | | | 492.68 |
| | | Full | Surface | 0.72 | $\pi r^2 l$ | 209.94 | |
| | | | Content | 0 | 0 | 0 | |
| | | | | | | | 209.94 |
| | z | Empty | Surface | $\frac{2}{\pi}$ | $\frac{4}{3}\pi r^3$ | 73.8 | |
| | | | Content | 1 | $\pi r^2 l$ | 282.74 | |
| | | | | | | | 356.54 |
| | | Full | Surface | $\frac{2}{\pi}$ | $\frac{4}{3}\pi r^3$ | 73.8 | |
| | | | Content | 0 | 0 | 0 | |
| | | | | | | | 73.8 |

Table 5.12: Added mass of the skip

Table 5.13 shows the added masses of the remaining components. As stated before, the final shape of the harvester, ladder and docking unit are unknown, so in this case they are simplified to a rectangular shape to approximate the added masses. The added masses are determined with the use of the DNV-RP-H103 [59].

| **Component** | $C_A$ **[-]** | | | $V_R[m^3]$ | | | $M_A$ **[t]** | | |
|---|---|---|---|---|---|---|---|---|---|
| | x | y | z | x | y | z | x | y | z |
| **Harvester** | 0.757 | 0.579 | 1 | 18 | 30 | 60 | 13.62 | 25.2 | 42.24 |
| **Ladder** | 0.84 | 1 | 1 | 4 | 200 | 200 | 2.316 | 200 | 200 |
| **Docking Unit** | 0.704 | 1 | 0.757 | 3.2 | 6 | 120 | 3.2 | 6 | 90.84 |
| **Rope** | 1 | 1 | - | $\pi r^2$ | $\pi r^2$ | - | 5.15 | 5.15 | [t/m] |

Table 5.13: Added mass of the harvester, ladder, docking unit and rope

### Viscous Damping

The damping of the rope has already been discussed in Section 5.2. However, a vibrating body in also damped by the surrounding viscous fluid [12]. This fluid damping occurs among other things due to the drag force that has been mentioned in Section 5.3. When considering the damping in the same axial direction as the rope damping the viscous damping due to drag is given by the following quadratic equation:

$$F_z = F_D = \frac{1}{2}\rho u^2 C_{D-z} A \tag{5.37}$$

However, the viscous damping does not only consists of the quadratic drag term, as this means that for low velocities almost no damping would occur. Therefore the following linear damping coefficient [kg/s] for motion of a lifted object is proposed by DNV: [59]:

$$\Sigma = \frac{4}{3\pi}\rho C_{Dz} A_p \omega \eta_L \tag{5.38}$$

where

- $\rho$ is the density of seawater [$kg/m^3$]
- $C_{Dz}$ is the vertical drag coefficient [-]

- $A_p$ is the vertical drag area of the lifted object [$m^2$]
- $\omega$ is the radial frequency of the movement [rad/s]
- $\eta$ is the motion of the lifted object [m]

# 6
# Model introduction

With the acquired information from Chapter 5, Orcaflex is used to model the deep-sea mining concept. All the different elements of the concept have been introduced and this chapter will make the translation from the real world to the software. First Orcaflex is introduced, where after it is described how the components are modelled in Orcaflex. Screenshots from the input in Orcaflex can be found in Appendix **??**.

## 6.1. Orcaflex

Orcaflex is a software package for the dynamic analysis of offshore marine systems. Orcaflex is much used within the offshore sector for the modelling of riser systems, transport, installation, decommissioning, pipelays etc. To analyse a real world system, which is described in Chapter 5, a mathematical model is build using the various modelling facilities provided by OrcaFlex. The model consists of two parts, the model objects which are bodies as configured by the user, and the environment to which the objects are subjected. The objects will be used to represent the deep-sea mining concept, while the environment will represent the current, waves and forward velocity of the system.

### Orcaflex objects

The objects that are used to model the deep-sea mining concept will be shortly summarized.

- **6D buoy** is a rigid body with 6 degrees of freedom. Three translational and three rotational degrees of freedom. Three different types of 6D buoy are available in Orcaflex and in this thesis mainly the lumped buoy version is used. It is shown in Figure 6.1. The shape is not defined by Orcaflex, which gives the freedom to implement the relevant characteristics of the modelled body.

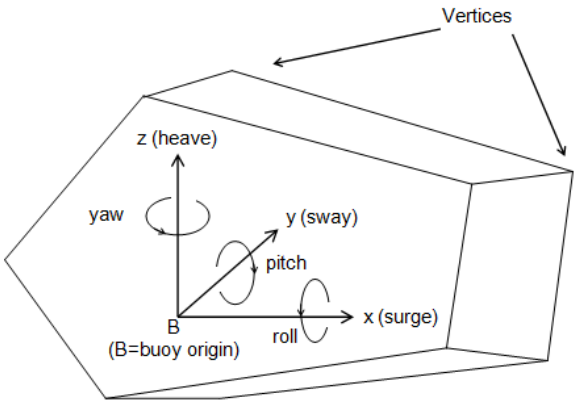


Figure 6.1: Lumped buoy

- **Vessel** are rigid bodies with motions as described by the user, to model ships, production platforms or any floating object. In this thesis it will be used to model the PSV.
- **Lines** are used in this concept to model the rope. In Orcaflex, lines are represented by a lumped mass model, as seen in Figure 6.2. The line is modelled as a series of masses joined together by massless springs. Each spring is called a segment which join the different lumped masses, which are called nodes. The node contains the properties of that line segment.

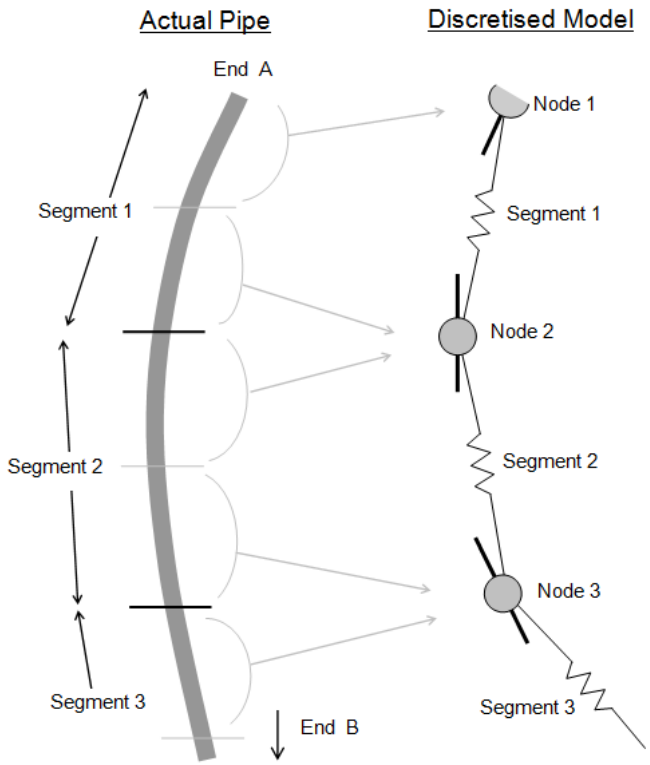


Figure 6.2: Orcaflex line model

- **Winches** are massless connections between two objects in the model. The winch has no surface or volume itself. It is used to simulate pay-in or pay-out at a user specified rate or tension.
- **Constraints** are massless and intended for connections between objects. They can be given certain constraints, for example the translational or rotational displacements.

### Orcaflex Environment

The expected environment is discussed in Section 4.1. In this section it is discussed how this is implemented in Orcaflex.

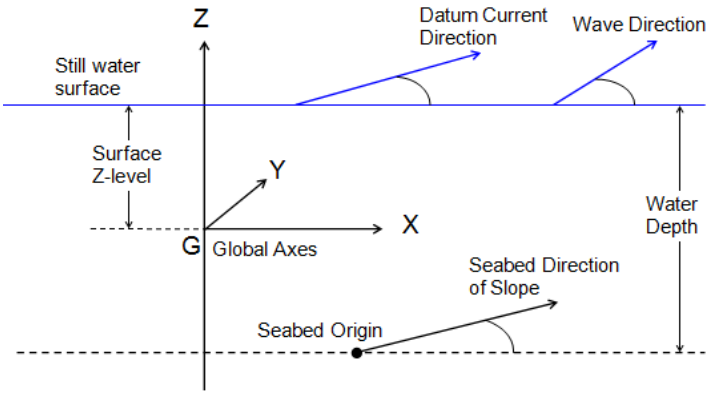


Figure 6.3: Orcaflex environment and axes

- **Current** The current variation as discussed in Section 4.1 can be given as input in Orcaflex. Horizontal current is specified as a 2D profile, variable in magnitude and direction, at different depth levels. This means no current is present in $z$ direction.
  The situation where the forward velocity of the deep-sea mining system is also simulated, this forward velocity is added as extra current. The focus in these simulations is the interaction of the different components of the VTS due to extra hydrodymamic forces. The ground interaction of the harvester is not in the scope

of this thesis, therefore the implementing of the forward velocity in the current is considered as sufficient.
- **Waves** As discussed in Section 4.3, a fully develop sea-state is expected. A modified Pierson-Moskowitz spectrum can be selected in Orcaflex where the $H_s$ and the $T_P$ need to be provided as input.

### Deep-sea mining concept components in Orcaflex

In this section the modelling of different components of the deep-sea mining concept in Orcaflex are discussed. A screenshot from an Orcaflex model is shown in Figure 6.4

#### Harvester

The harvester is modelled as a 6D buoy with the characteristics as described in Chapter 5. The decision has been made to fixate the harvester to the seabed. The modelling of the ground interaction is complicated and is not within the scope of this thesis. Interesting input for the ground interaction like force on the harvester in x- and y-direction, can still be derived out of the simulations this way. Approximations of the harvesters traction can be tested with this information.

#### Ladder

The ladder is modelled as a 6D buoy with the characteristics as described in Chapter 5. The connection between the harvester and the ladder and the docking unit and the ladder is made with a hinge. This hinge modelled with a constraint. As stated, a constraint is able to fixate individual degrees of freedom. In this hinge, the only degree of freedom the connection has, is the rotation around the y-axis. This constraint models the hinges that will allow the system to manoeuvre over hills while keeping the docking unit horizontal.

#### Docking Unit

The docking unit is modelled as a 6D buoy with the characteristics as described in Chapter 5. It is connected to the ladder by means of a hinge, allowing it to freely pitch. The docking unit is hanging from the four guidance ropes, keeping it in place and horizontal, 20 meters above the seabed.

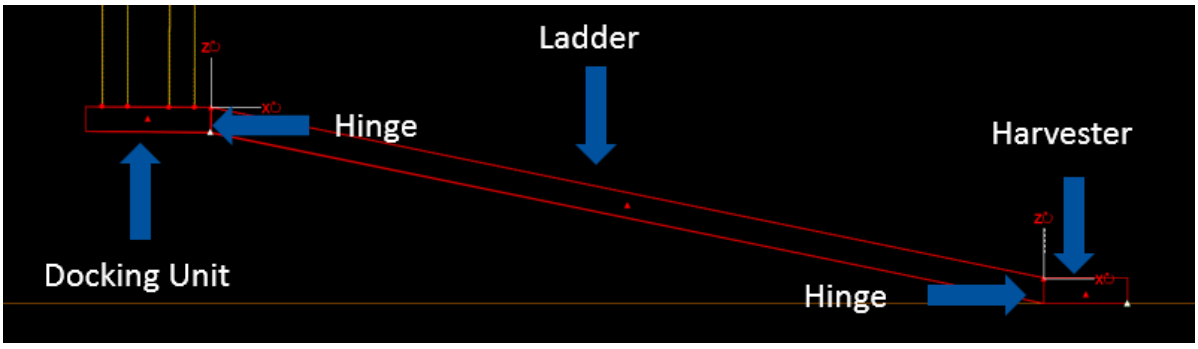


Figure 6.4: Seafloor production tool components as modelled in Orcaflex

To allow easy entry and departure of the skip from the docking unit, it is desired to keep the docking unit horizontal during operations. Due to the hinges between the harvest, ladder and docking unit, the tension distribution of the guidance wires is asymmetrical, as illustrated in Figure 6.5.

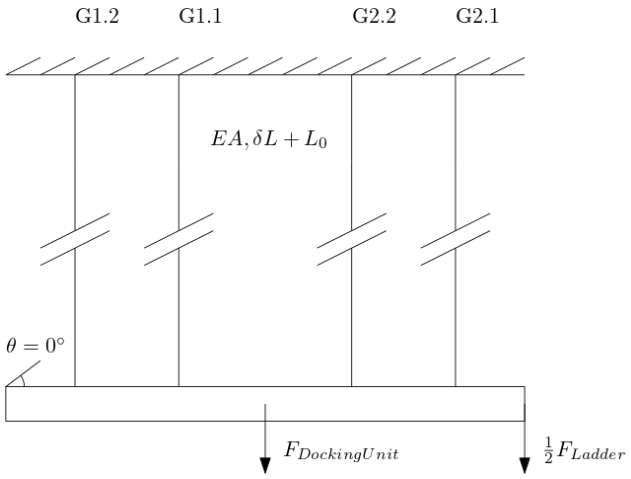


Figure 6.5: Asymmetrical loading of the docking unit

The weight of the docking unit is divided evenly over the four ropes, but the weight of the ladder is connected to the front of the docking unit. It is assumed that the weight of the ladder is evenly divided between the harvester and the docking unit. This gives the situation as seen in Figure 6.6.

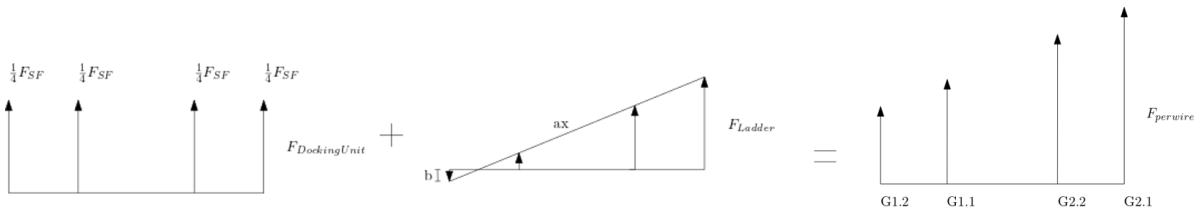


Figure 6.6: Tension distribution over the guidance wires to enable a horizontal docking unit

As the docking unit is horizontal, the ropes all have the same stretched length. But as the tension is different in the ropes, the unstretched length will be different. This can be calculated with the Tension distribution in the guidance wires with the horizontal docking unit 20 meter above the seabed (so at 5980 meters depth) is shown in table 6.1.

$$L_0 = \frac{L_s}{\frac{F+w}{EA}+1} \tag{6.1}$$

| | **Guidance wires** | | | | |
|---|---|---|---|---|---|
| **Characteristic** | **1.2** | **1.1** | **2.2** | **2.1** | **Unit** |
| **Tension** | 336.9 | 475.5 | 706.6 | 845.2 | [kN] |
| **Initial length** | 5964.4 | 5958.0 | 5947.4 | 5941.1 | [m] |
| **Elongation** | 15.6 | 22.0 | 32.6 | 38.9 | [m] |

Table 6.1: Tension distribution in the guidance wires at Docking Unit inclination = $0^oC$

### Skips

The skips are modelled as a 6D buoy with the characteristics as described in Chapter 5. The skip is lifted by two hoisting wires and guided by two guidance wires that run through the eyelets on the side of the skip, modelled by two line segments fixed to the 6D buoy. The mass and volume must be adjusted to account for a full or empty skip.

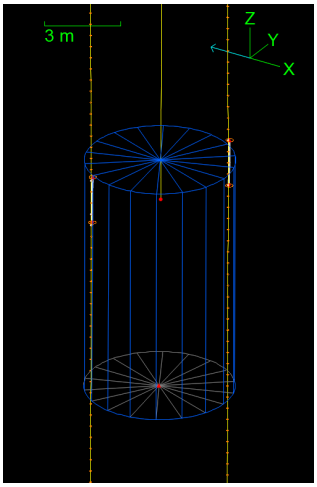


Figure 6.7: Skip in Orcaflex

### Ropes

In the concept there are hoisting wires and guidance wires as introduced earlier. For both it is assumed that the same synthetic fibre rope is used, as introduced in Section 5.2. These are modelled in Orcaflex as lines. The guidance wire is used by the skip as *guidance*. Orcaflex enables it to model contact between lines and is able to model one line contained within another. This way the eyelets of the skip are modelled. As can be seen in Figure 6.7, two line segments have been placed on the sides of the skip, parallel to the direction of the skip, vertical. These line segments consists of two meter long, single piece segments. This means that only on the ends, nodes are placed. The guidance wire is the *penetrating* line, while the eyelet line segment is the *splined* line. The way this is modelled is illustrated in Figure 6.8. The contained guidance wire is represented by the penetrating line, and the containing eyelet is represented by the splined line. When the penetrating line nodes are within the length of the containing line, their penetrators will contact the inner surface of the containing line. The contained line nodes can not escape the containing line inner surface other than running of the open end. Due to this modelling, the eyelet line segment is chosen to be two meters, as the line segment length of the contained line must be lower than the container. When hoisting the skip along the guidance lines, the line segments of this guidance line must be smaller than two meter. With a water depth of 6000 meter, this has a great influence on the simulation run time. To mitigate this, the hoisting or lowering of the skip is not simulate over the whole length, but only a part. This way only the depth-level where the skip will be needs to be with a fine mesh.

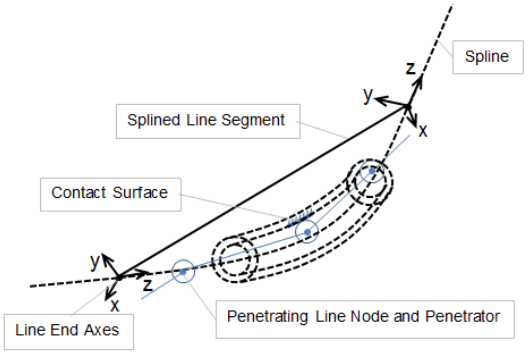


Figure 6.8: Line contact modelling

In the deep-sea mining concept, the eyelets will probably not be two meter long pipes on the side of the skip. Simplicity is the reason that the choice has been made to model it this way. The desired output of the model is a single interaction force between the eyelet of the skip. The given output of this model

is a connection force in both of the nodes, as seen in Figure 6.9. This connection force is given in kN/m. The total connection force can be derived by integrating these two connection forces over the length of the segment, as seen in equation 6.2.

$$F_{interaction} = F_A l + \frac{|F_B - F_A|) l}{2} \tag{6.2}$$

as l = 2 m this can be simplified to equation 6.3

$$F_{interaction} = F_A + F_B \tag{6.3}$$

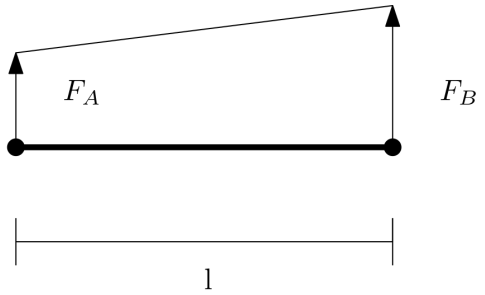


Figure 6.9: Connection force modelling

Four guidance wires are connected to the docking unit, four hoisting wires are connected to the skips. These hoisting wires will be payed-in and out during operations by winches, in the model the line can be given a fixed pay-in or out velocity. The spooled up line, which would be on the drum in the concept, plays no part in the model whatsoever and does not exist for the purposes of simulation. The line appears from or disappears in the upper end.

**Production Support Vessel**

The The vessel is modelled according to the characteristics mentioned in Chapter 5. The Production Support Vessel will experience motions due to the environment it is situated in. Its response on this environment will be translated to responses of the ropes, which are translated to responses of the skips and the SPT. The environment is introduced in Section 4.3. Orcaflex is able to calculate the vessel motion based on the implemented RAO's, as seen in Figure 6.11. The software package AQWA is used to derive the vessel RAO's. With this input Orcaflex can determine the motion of suspension points of the ropes. The ropes are assumed to be located on starboard side, 60 meters front of the aft of the ship. The wave heading is set to $30^o$, as it is assumed that during operation the ship can maintain its heading with the use of the dynamic positioning system. It might be possible for the vessel heading to differ from the heading of the mining operation. This means that for instance when the wave direction changes, but the mining operation continues in the same direction, the vessel can alter its heading so the wave are approached head-on. In most cases this will lead to less heave movement of the top of the ropes. A disadvantages is that distance between the ropes might decrease, increasing the chance for clashing and entanglement. It is recommended to research this in the future.

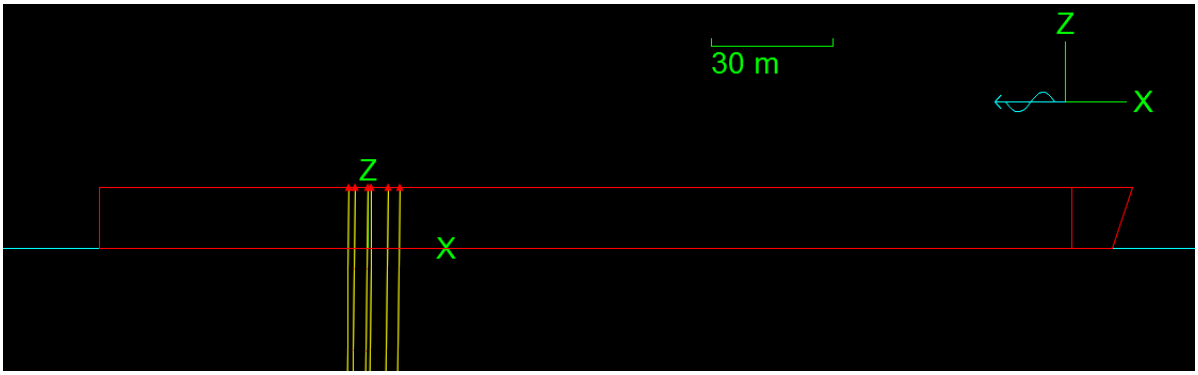


(a) Side-view vessel in Orcaflex

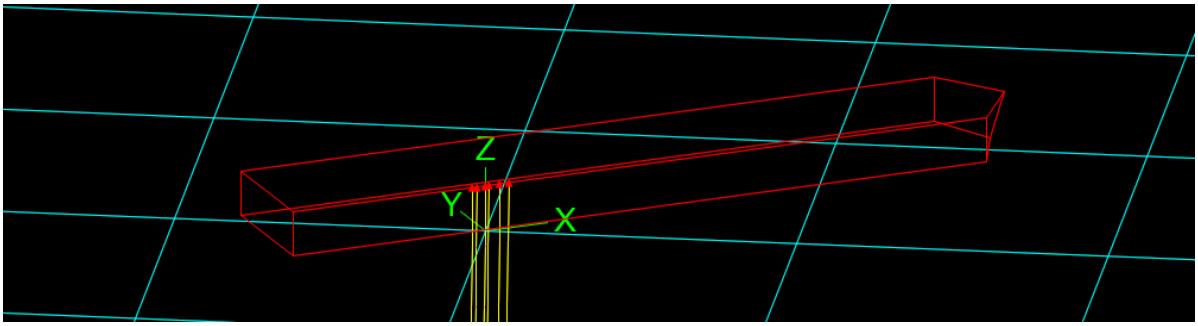


(b) 3D view vessel in Orcaflex

Figure 6.10: Production Support Vessel in Orcaflex

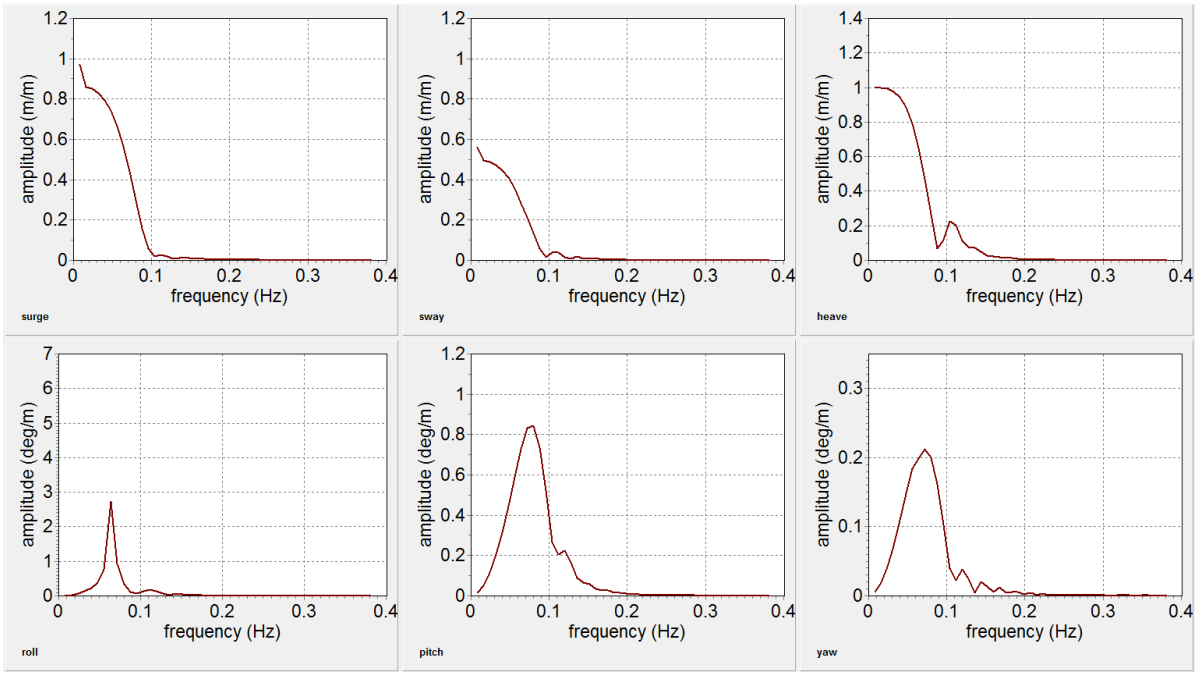


Figure 6.11: Vessel RAO's for a $30^o$ heading

# 7
# Model analysis

The aim of this chapter is to discuss the different models that have been created in order to analyse the deep-sea mining system. In the models, all the information gathered during this thesis is brought together. The subjects that will be discussed in this chapter are the following:

- Current analysis
- Forward Velocity analysis and the modification in the mining method
- Production Cycle
- Rope Entanglement
- Dynamic Analysis which consists of the modelling of the damping, heave motion of the skips and the docking unit
- Vortex Induced Vibrations

## 7.1. Current Analysis

In this section the behaviour of the ropes is investigated. The docking unit, with a weight representative of the whole SPT (240 tonnes submerged), and two empty skips are suspended from the vessel, which is fixed in space. This set-up is shown in Figure 7.1(b). Three different situations are tested and the results are shown in table 7.1. The current profile for the Clarion-Clipperton Zone is introduced in Chapter 4 and for clarification shown again here in Figure 7.1(a). This current profile is the standard current profile that will be used in the other models. This current profile is chosen to be opposite of the vessel heading, as this will result in the maximum relative velocity and therefore the maximum drag. The two other current profiles that are assessed, have a direction that is not $180^o$ with respect to the heading of the vessel. One is transverse, so 90 degrees with respect to the heading of the vessel. The second is a current that changes in direction over the depth, as was shown in Section 4.1 to be the most realistic current profile. Drag from different sides cancels each other out which results in a lower total drag force on the ropes. It results in a variable x- and y position of the rope over depth, as seen in Figure 7.2.

| **Situation** | **Standard** | **Transverse** | **Changing direction** | **Unit** |
|---|---|---|---|---|
| **Direction** | 180 | 90 | 90 - 270 | $^o$ |
| **Surface Current** | 1 | 1 | 1 | m/s |
| **Benthic Current** | 0.1 | 0.1 | 0.1 | m/s |
| **X-Force on vessel** | -117.48 | 0 | -17.28 | kN |
| **Y-Force on vessel** | 0 | 117.48 | 112.52 | kN |
| **X-Offset Docking Unit** | -30.54 | 0 | -9.76 | m |
| **Y-Offset Docking Unit** | 0 | 30.56 | -11.59 | m |

Table 7.1: Results of the different current profiles

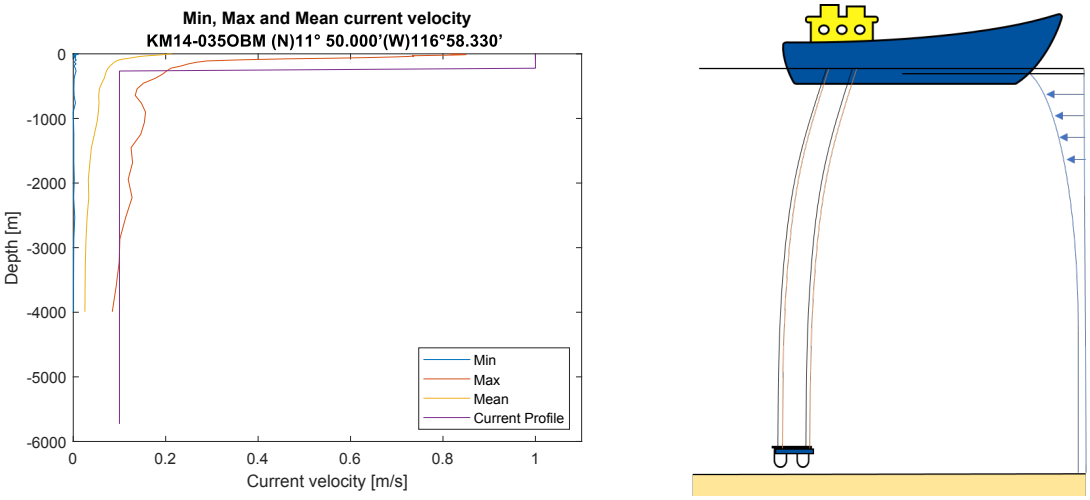


(a) Min, max, mean and "standard" current profiles

(b) Current analysis set-up

Figure 7.1: Current analysis

The rope shape of the three analysed current profiles is shown in Figure 7.2. The $x$ position is shown in blue and the $y$ position is shown in orange, as shown in the legend in the right bottom corner.

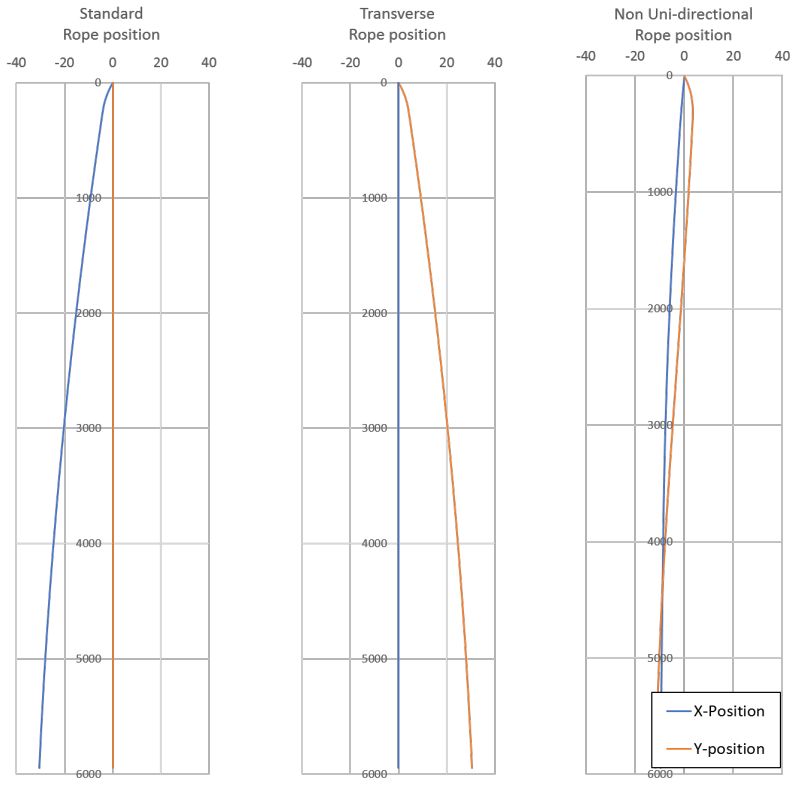


(a) Standard current

(b) Transverse current profile

(c) Changing over depth

Figure 7.2: Rope shape in different current

Changing the direction of the same current profile does not make a difference in the total drag on VTS, as all its components are symmetric. A topview of the head-on and transverse current is shown in Figure 7.3. It does change the total resistance and requirements of the vessels dynamic positioning system.

A transverse current will result in a much higher drag force on the ship, which is not taken into account in the results in table 7.1. Besides the higher ship resistance, the transverse drag force must be accounted for by the side thrusters of the ship, whereas the head-on current position keeping can be regulated with the main power system. This won't be further discussed in this thesis, but is recommended to be taken into account for further operational research.

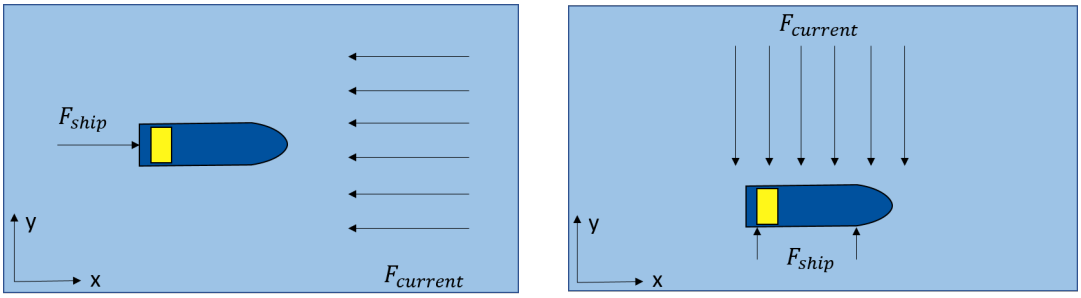


(a) Ship in head-on current

(b) Ship in transverse current

Figure 7.3: Topview of the ship in head-on and transverse current

## 7.2. Offset introduction

The model has two boundary conditions, the vessel and seabed. The vessel is fixed in space in the model, as the position is maintained with a dynamic positioning system in real-life. The harvester is the connection to the seabed of the deep-sea mining system. These two connections must account for all the drag force on the system, as seen in Figure 7.4.

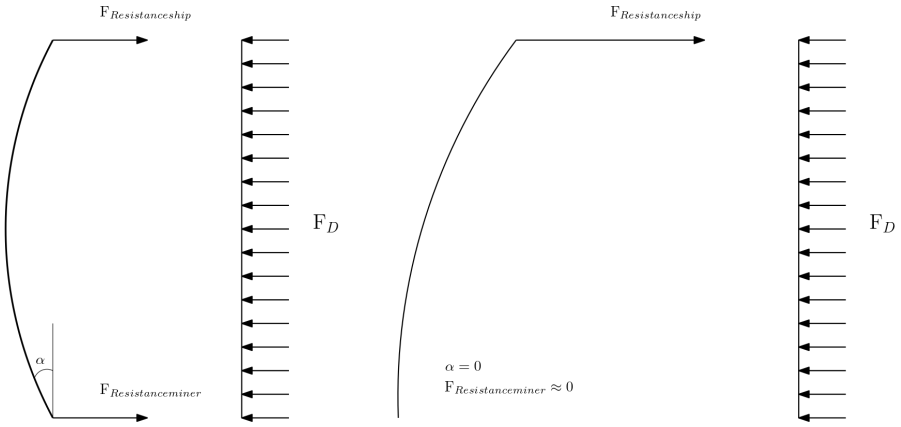


(a) No offset, large force on the harvester

(b) No drag force experienced by the harvester

Figure 7.4: Drag force distribution

Ropes can only exert force in axial direction. This means, that when a rope is vertical, no horizontal force is exerted on the object they are attached to. This can be seen in Figure 7.4(a). In these models, one of the requirements is the horizontal force exerted on the harvester to be as low as possible. The harvester has its own propulsion to be able to manoeuvre over the seabed. When exerting no horizontal force on the harvester, the control and traction are assumed to be optimal. It could be substantiated that a positive horizontal force on the harvester (working like a plough) could "ease" the required propulsion power, but this is not the starting-point in these models. The horizontal difference between the connection points of the wires at the docking unit with respect to their suspension points at the PSV is called offset. This is illustrated in Figure 7.5. The importance of offset is introduced to discuss the forward velocity in the next section and will be further analysed in Section 7.4.

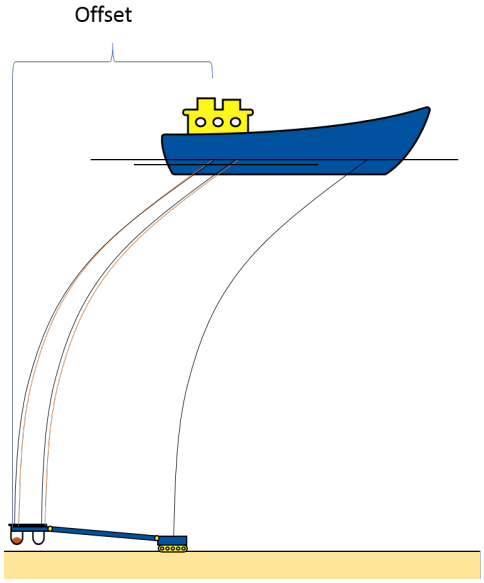


Figure 7.5: Offset visualization

## 7.3. Forward Velocity analysis

In this section the forward velocity of the system is analysed. The forward velocity is modelled by adding it as a constant-over-depth to the current profile in Orcaflex. To illustrate the influence of the forward velocity, a constant current velocity over depth is introduced, which results in two current profiles as seen in Figure 7.6.

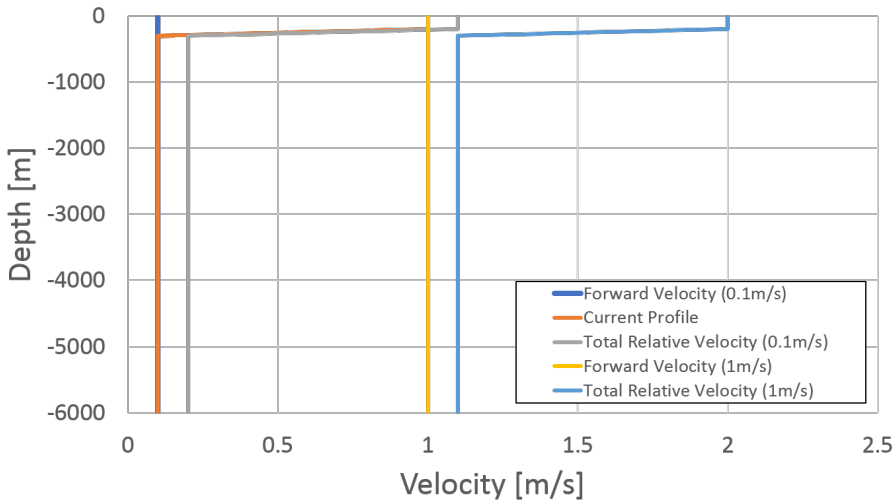


Figure 7.6: The different forward velocities added to the current profile as constant velocity

The production cycle is described in Section 3.3, where the design choice of a forward velocity to get the desired production rate is introduced. In this analysis the influence of the forward velocity on the system is elaborated.
To get acquainted with the rope shape and behaviour of the system, first a full and an empty single skip suspended from two hoist wires with different forward velocities are modelled, as shown in Figure 7.7. The values of the offset are shown in table 7.2, showing the great difference in offset between the two forward velocities. Besides the differences in forward velocity, the difference in mass also results in different offsets. The figure represents the logical situation of the heavier full skip having less offset than an empty skip.

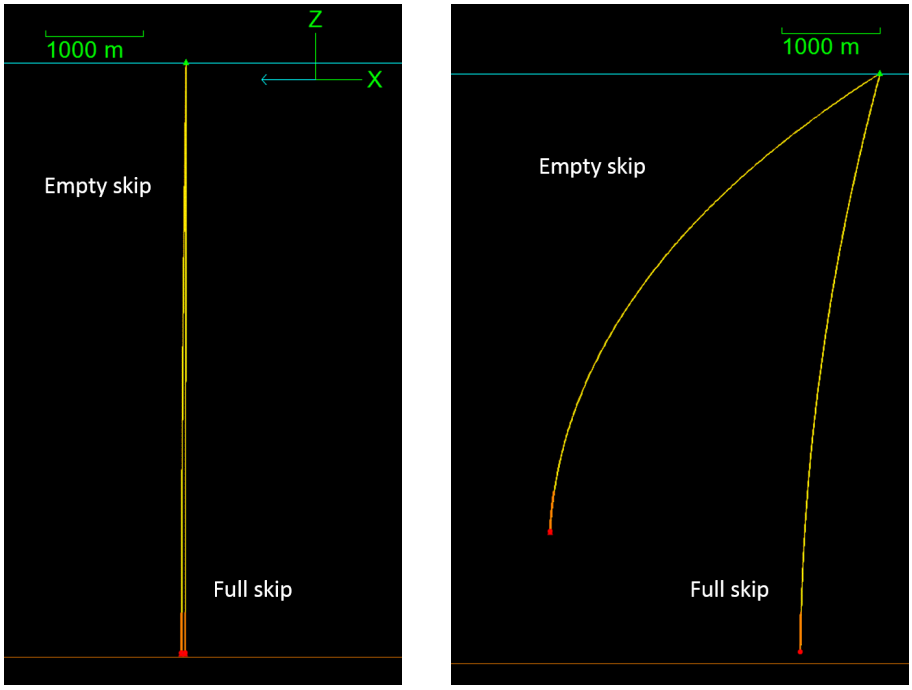


(a) Production velocity 0.1 m/s (b) [Production velocity 1 m/s

Figure 7.7: Single skip suspended from on two hoisting wires in a constant current

| | **Production Velocity** | | **Unit** |
|---|---|---|---|
| | 0.1 | 1 | m/s |
| **Empty skip** | -198.68 | -3346.03 | m |
| **Full skip** | -10.01 | -807.39 | m |

Table 7.2: The position of the skip

To analyse the influence of the forward velocity the same model composition is used as in the current analysis. The docking unit, with a weight representative of the whole SPT (240 tonnes submerged), and two empty skips are hanged from the vessel, which is fixed in space. Figure 7.8 and table 7.3 show the results of this simulation. The pink lines are the hoisting wires and the yellow lines are the guidance wires. The hoisting wires have a wider shape than the guidance wires, as the tension in the hoisting wires is lower. The ropes come together as the skip is attached to the guidance wires by means of the eyelets. The interaction force between the eyelet and the rope is much higher in the 1 m/s forward velocity case, just like the offset and the horizontal force on the vessel. The drag has a quadratic dependency on the velocity, so a reduction of the velocity with a factor 10 is expected to result in a reduction of the drag by a factor of 100. As can be seen in table 7.3, this is not the case in these simulations. This is due to the effect as discussed in Section 5.3. The drag force is perpendicular to the rope, so for an inclined rope with a horizontal current the drag force is split in a perpendicular and parallel force. This parallel force depends on the skin friction, which is generally much lower than the drag coefficient. Due to the high inclination of the 1 m/s case, part of the energy of the current is "lost" to this low skin friction, resulting in a lower horizontal drag force increase-factor on the vessel. It is chosen to compare the horizontal reaction forces as this force needs to be accounted for by the vessel's dynamic positioning system.

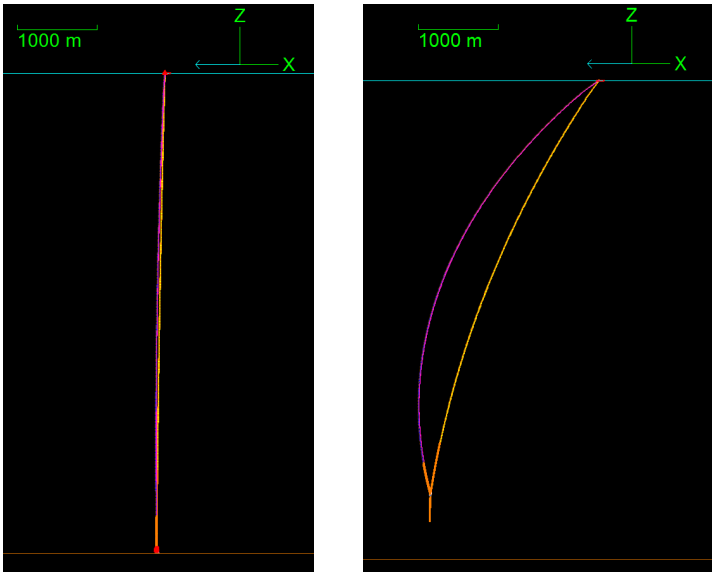


(a) Production velocity 0.1 m/s (b) [Production velocity 1 m/s

Figure 7.8: Docking Unit and two skips suspended from the vessel

| | **Production Velocity** | | **Unit** |
|---|---|---|---|
| | **0.1** | **1** | m/s |
| **Position of the Docking Unit** | -104.26 | -2112.64 | m |
| **X-Force on vessel** | -208.01 | -2113.13 | kN |
| **Connection force Eyelet-Rope** | 3 | 66 | kN |

Table 7.3: Results of the forward velocity analysis

To compensate for the high drag forces, the vessel would need to have enough power to maintain a 1 m/s forward velocity, while keeping the SPT free of horizontal forces. It can be seen in table 7.3 that this would require at least 200 tonnes constant propulsion force during operations. Therefor another harvesting solution is further elaborated in Section **??**. This solution enables the system to have a forward velocity of 0.1 m/s. This results in a current profile that will be used the rest of the simulations (unless mentioned otherwise) as seen in Figure 7.9.

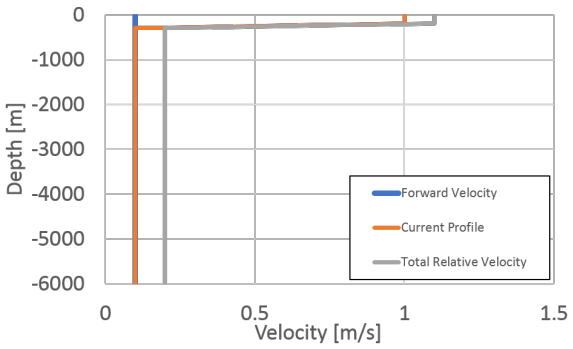


Figure 7.9: Current profile

## 7.4. Production Cycle

### Base Case

Especially during operations, the offset is desired to be equal to the natural position of the combined SPT and VTS in the current + forward velocity. This way, the harvester will experience the least amount of reaction forces. This position can be derived from table 7.3: ~ 104 meter offset. This offset will be used as a base case. The vessel is a fixed boundary condition and so is the harvester at the seafloor. The 104 meter offset is the horizontal distance between the suspension points of the ropes at the top and bottom. It is expected that the elevation and the mass of the skips will influence the horizontal force on the harvester.

#### Vertical transportation with the skips

To investigate the interaction between the skip's eyelets and the guidance wires and the horizontal force, this base case will be subject of several simulations. A single full and empty skip are simulated at different elevations. The influence of elevation on the horizontal force on the harvester is shown in Figure 7.10.

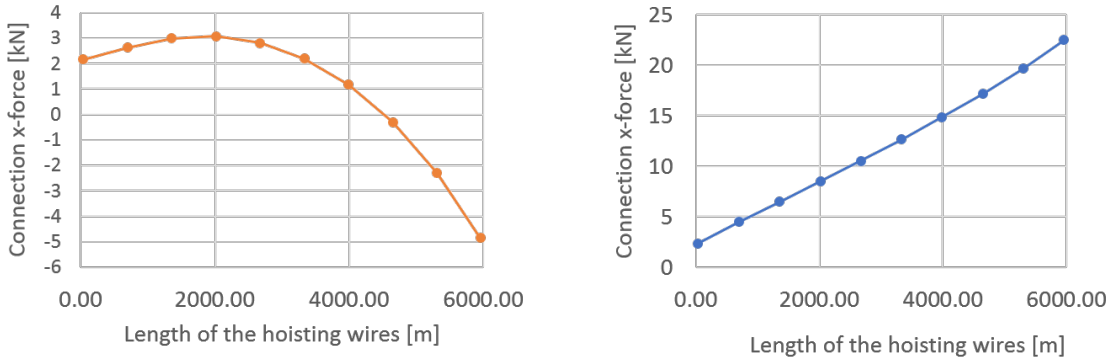


(a) Empty skip

(b) [Full skip

Figure 7.10: Force on the harvester in x direction

Preliminary investigation showed that the interaction force between the eyelets and the guidance wires is largest when the skip enter the 1 m/s current profile, at around 250 meter water depth. Both skips are simulated to be lifted or lowered through this water depth, results in the interaction forces as shown in Figure 7.11

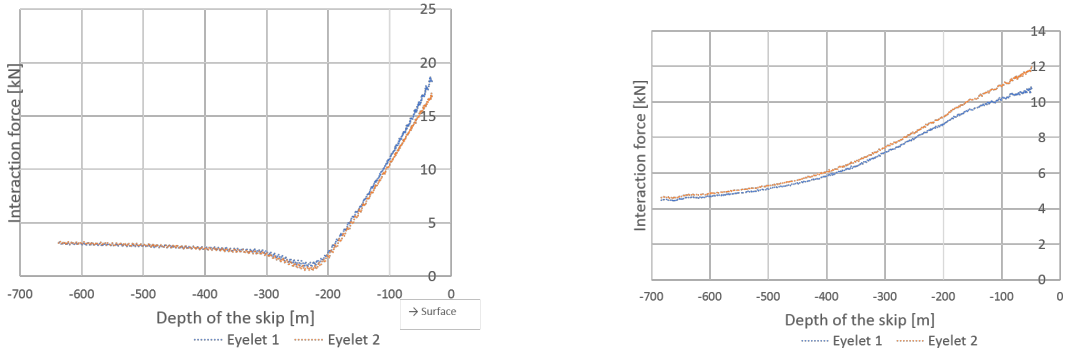


(a) Empty skip

(b) [Full skip

Figure 7.11: Interaction force

### Filling of the skip

During production, the mass of the skip will increase with a constant rate. As stated in Section 3.3, an empty skip has a submerged weight of 394.39 kN which will increase to a submerged weight of 2248.01 kN when the

skip is completely filled. It is desired that the hoisting wires account for this increase in weight, making sure the guidance wires are as statically loaded as possible. Due to the increasing weight of the skip the hoisting wires will elongate, resulting in the need to haul in the wires at the PSV during production to evade the transfer of forces to the guidance wires. This increase in tension and elongation as a function of the fill rate is shown in table 7.12. Every skip is suspended from two ropes, explaining a maximum tension in the ropes of ~ 1100 kN.

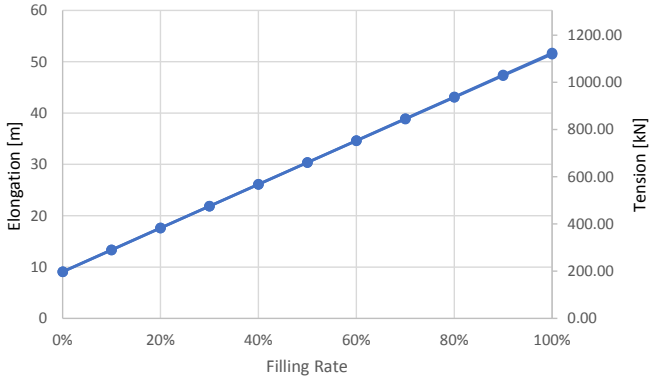


Figure 7.12: Fill cycle of the skip

Another effect of the filling of the skip is the decreased offset. This offset is the equilibrium between the horizontal drag force and the gravity working upon the system. Increasing the weight whilst the current environment stays the same results in a smaller offset. This can be seen in Figure 7.13(a). An empty skip has an offset that is much larger than the offset of the base case, whilst the full skip has an offset that is much closer to the suspension point than in the base case. This difference in natural offset is the reason the guidance wires are in place. However, it results in a horizontal force exerted on the harvester, as seen in Figure 7.13(b). At a filling rate of 20 % the natural offset of the skip equals the offset of the base case, resulting in ~0 horizontal force on the harvester. The skip at higher filling rates will "push" against the docking unit resulting in a horizontal force on the harvester in positive x direction. The skip at lower filling rates will "pull" the docking unit backwards, resulting in a horizontal force on the harvester in negative x direction.

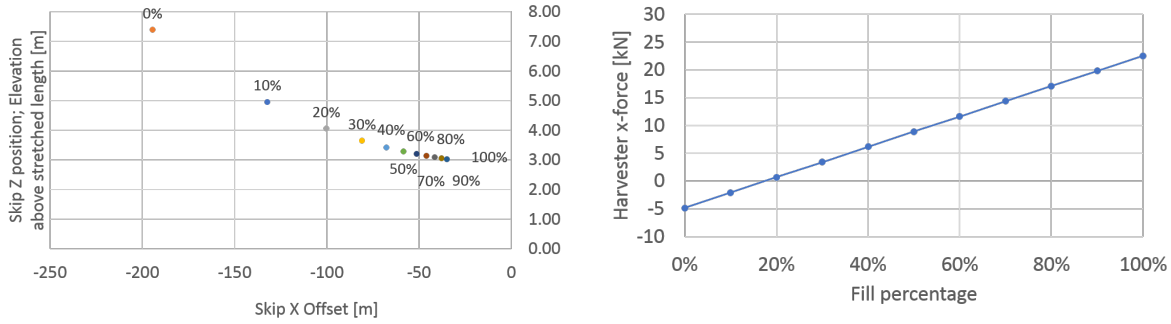


(a) Position of a single skip in the current, with increasing weight

(b) Force on the harvester due to the filling of the skip

Figure 7.13: Skip - Docking Unit interaction

It can be concluded that the maximum force variation on the harvester due to the filling of the skip is 30 kN. The maximum force is related to the maximum natural offset difference. During operations, these horizontal forces on the harvester can be mitigated by changing the position of the harvester. This way the forces can be minimized.

### Offset Analysis

As stated, the deep-sea mining system has two boundary conditions, the harvester at the seabed and the PSV at the surface. During operations, the forward velocity is determined by the collection speed of the

harvester. The PSV must remain in position with respect to the docking unit and the harvester by using its propulsion and the dynamic positioning system. In this section it is analysed what happens if the dynamic positioning system is not able to keep up or if the vessel sails on, while keeping the same rope length, by changing the position of the vessel with steps of 100 meter. The harvester is still fixed to the seafloor and the horizontal force on the harvester due to the offset is analysed and shown in Figure 7.14(a). Again, the base case is used to model the offset analysis, leading to horizontal force on the harvester = 0 at a 104 meter offset. The position of the vessel is varied from about 700 meters aft of base case position to 600 meters ahead of the base case position. The highest horizontal force is correlated with the highest offset, which results in a maximum force of 400 kN. This is in the situation that the vessel is 700 meters behind the base case position, which is a very unlikely scenario to happen during operations. Also, the tension in the ropes and therefore the horizontal force on the harvester can be controlled by handling of the ropes. Paying out of the rope or hauling in changes the length and the tension, allowing for control of the forces during normal operations.

As can be expected when keeping the ropes at a constant length while increasing the offset, the docking unit will be elevated, as shown in Figure 7.14(b). Within a 250 meters radius around the base case position the docking unit elevation will be below the 10 meters, which illustrates the relative low influence of the vessel offset on the vertical elevation of the docking unit. During operations, the height of the docking unit with respect to the harvester and the ground can be controlled by handling of the ropes.

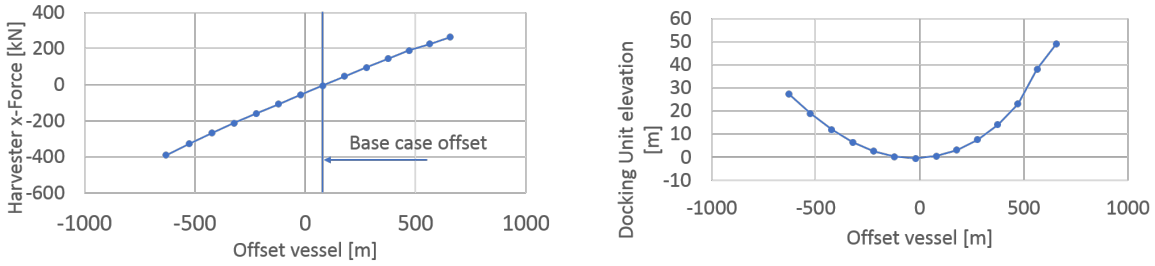


(a) Horizontal force on the harvester

(b) [Docking Unit Elevation

Figure 7.14: Offset analysis

## 7.5. Rope Entanglement

One of the main concerns when utilizing mechanical lifting for the vertical transportation of the nodules is rope entanglement. Moving skips amidst a bundle of ropes causes many possible problems. For instance the clashing of ropes that might induce damage. An even more severe case is a skip, that won't be as smooth in real-life as assumed in this thesis, that gets stuck behind ropes and in its lift ruptures the rope. This will cause major downtime of the system.
The eyelets on the skips account for the handling of the guidance wires associated with that skip. However, it can move freely with respect to the other guidance wires. This can be seen in Figure 7.17. Figure 7.15(a) shows the skip relatively close the surface while the current is acting upon the system. The empty skip is pushed into the guidance wires that are assigned to the other skip. Whilst being lifting unto the surface, one of the ropes can get stuck and damage might occur. To further illustrate this difference in position of the ropes and the skips, loaded or unloaded, the 1 m/s case is also shown in Figure 7.15(b). There is a big difference between the offset of the full skip and the guidance wires, allowing possible entanglement during operations to possibly occur. A close-up of a full skip being hoisted during 0.1 m/s forward velocity is shown in Figure 7.18.

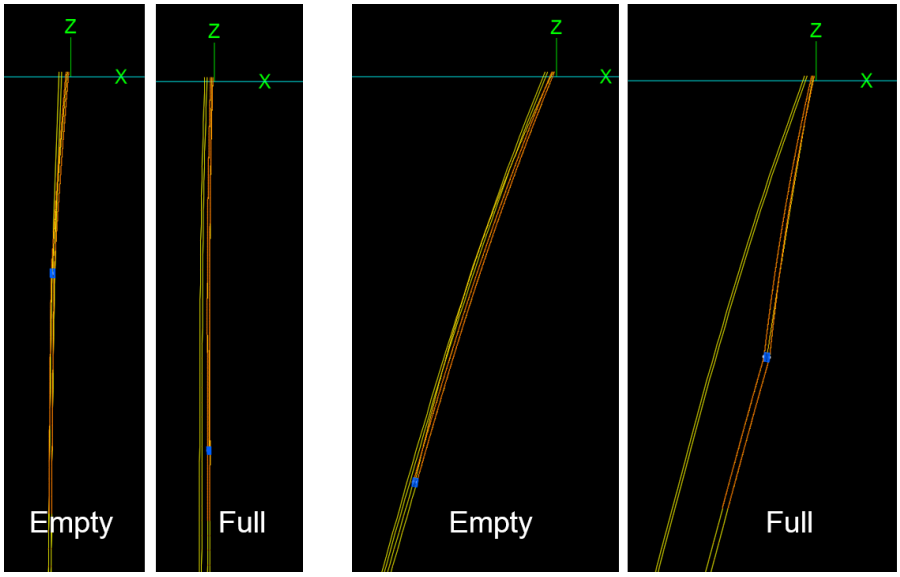


(a) Production velocity 0.1 m/s (b) [Production velocity 1 m/s

Figure 7.15: Full skip being hoisted in different forward velocities

To account for this possible entanglement, a wire frame is introduced. This wire frame extends the amount of eyelets on a skip from two to six. This wire frame makes sure that it is no longer possible for the skip to get stuck behind a rope of some kind. A side view of the wire frame is shown in Figure 7.16(a), where the guidance wires are presented in yellow and the hoisting wires are presented in blue. When the wire frame is used during operations it is attached to the travelling skip, while the other skip is down at the SPT. Therefore it also needs to include the hoisting wires of the other skip. When arriving at the production location, the wire frame is lowered with the empty skips. Once the first skip is full, it will be hoisted to the PSV together with the wire frame. The wire frame will travel down with the empty skip to the docking unit. Once the skip is docked, the wire frame will detached from the empty skip and attach itself to the full skip. Figure 7.16(b) shows a simplified sketch of the topview of the wire frame, which has a comparable size to the docking unit.

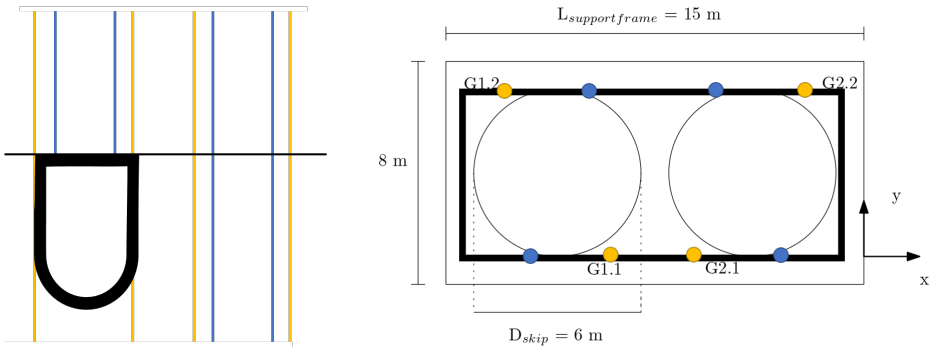


(a) Wire frame side view (b) [Wire frame top view

Figure 7.16: Wire frame sketch

In Figure 7.17(a), the position of a full skip with respect to the surrounding ropes is shown. The ropes cross and when lifted the skip can get stuck and break a rope. Figure 7.17(b) shows the influence of the wire frame. When the skip passes, the wire frame makes sure that the ropes all are in the right position and snagging is not possible.

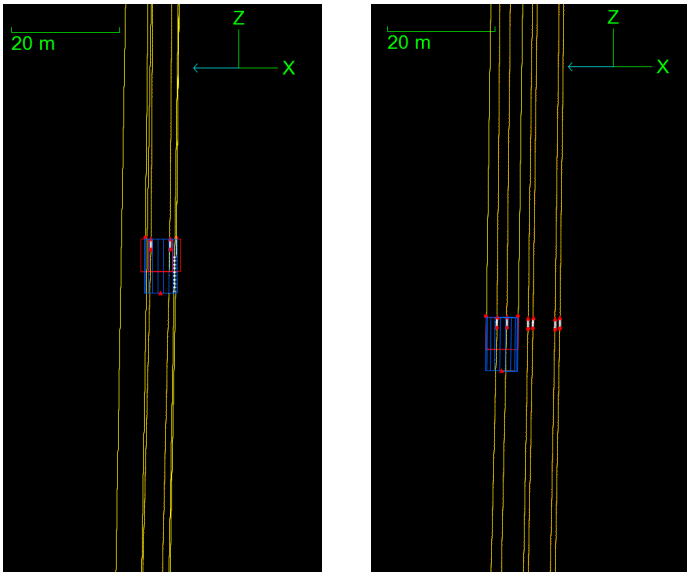


(a) No wire frame (b) Wire frame

Figure 7.17: The influence of a wire frame

A close-up of this comparison of a full skip with and without wire frame is shown in Figure 7.18. Here the eyelets are shown in red, the corresponding guidance wires are shown in green, the hoisting wires are shown in green and the guidance wires of the other skip are shown in yellow. Figure 7.18(a) shows that the full skip is enclosed by the guidance wires associated with the other skip. Figure (7.18(b)) shows the impact of the wire frame, as it neatly arranges the ropes.

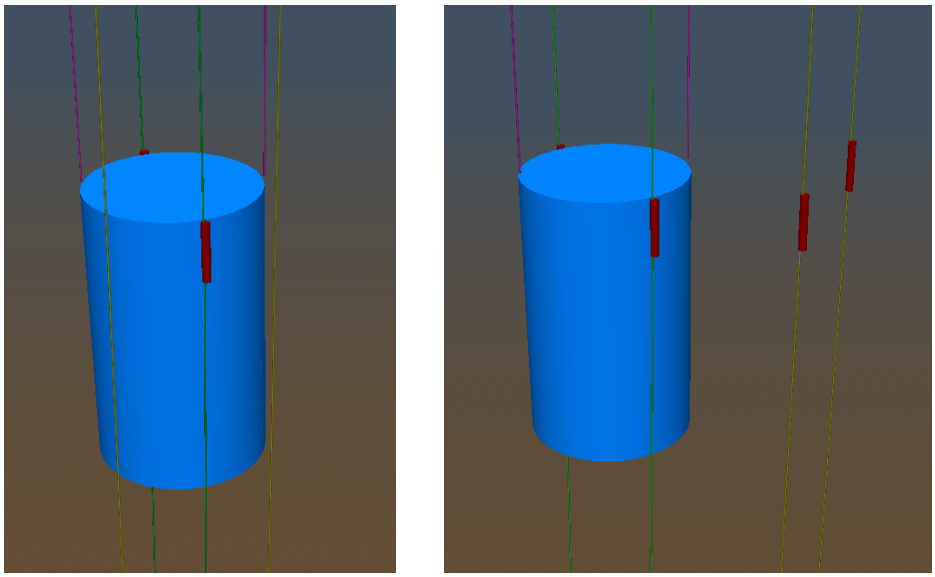

(a) No wire frame (b) Wire frame

Figure 7.18: The influence of a wire frame

A consequence of the wire frame is that friction forces will be exerted on all the ropes every cycle, instead of only the guidance wires associated with the travelling skip. The interaction force that results in a friction force is due to the difference in natural offset and drag differences. The advantage of more connection points is that this force will be divided over all these eyelets. The total interaction force will stay the same, making the friction force between the single eyelets and ropes less. In this thesis the wire

frame is only introduced as a solution to prevent possible entanglement, but no further research is done with regards to the design of the wire frame or the wear of the ropes. The connection points of the wire frame to contain the ropes should be designed to exerted as little friction as possible, but also the wear and fatigue properties of the synthetic fibre rope to be further investigated. Besides, the wire frame introduces more smart engineering, as it needs to be (dis)connected after every round trip and possibly also when emptied at the PSV. It adds a submerged unit that needs power, which decreases the simplicity of the concept. The introduction of the wire frame will results in asymmetrical drag forces while hoisting and lowering the combined skip/wire frame through the water column. Further research on the stability of this combined system during vertical transportation is recommended.

## 7.6. Dynamic analysis

When the system is deeply submerged and the skip is lifted from the vessel in waves, the vertical motion of the skip is governed by the motion of the top of the rope, which is fixed to the vessel. To estimate the expected vertical motion of the skip and the SPT a dynamic analysis is done. The dynamic behaviour of the system is determined by the vessel motions, which occur based on the vessel's RAOs and the wave environment it is subjected to. The Pierson-Moskowitz spectrum that is used in this analysis is introduced in Section 4.3. The vessel's specifications are introduced in Section 6.1. For the dynamic analysis modelling: the full and empty skips will be suspended from the vessel on seven different depths. This leads to 14 different situations, that are all subjected to a 3-hour sea state. From this three hours simulation, the highest amplitude of the skip and highest tension in the wires will be compared.

### Time Series Vessel

Implementing the wave spectrum and the obtained vessel RAOs in Orcaflex, results in the following vertical top of the rope motion, which is called heave. In deep water operations only this vertical motion is of interest [59]. As stated above, the model will simulate three hours. This results in the heave motion of the top of the rope as seen in Figure 7.19.

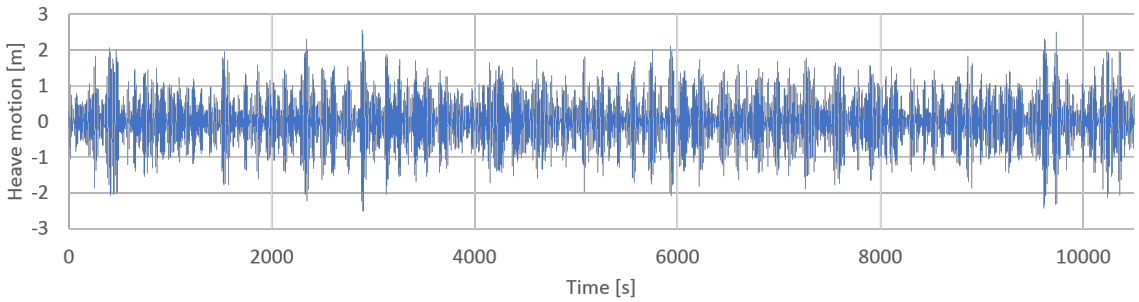


Figure 7.19: Heave motion of the top of the ropes

To further analyse the heave motion of the top of the rope, a spectral density graph is created, as shown in Figure 7.20. The energy of the heave can mainly be found between the dashed green lines, whereas it is mostly concentrated between a frequency of 0.06 and 0.09 Hz, indicated by the dashed red lines.

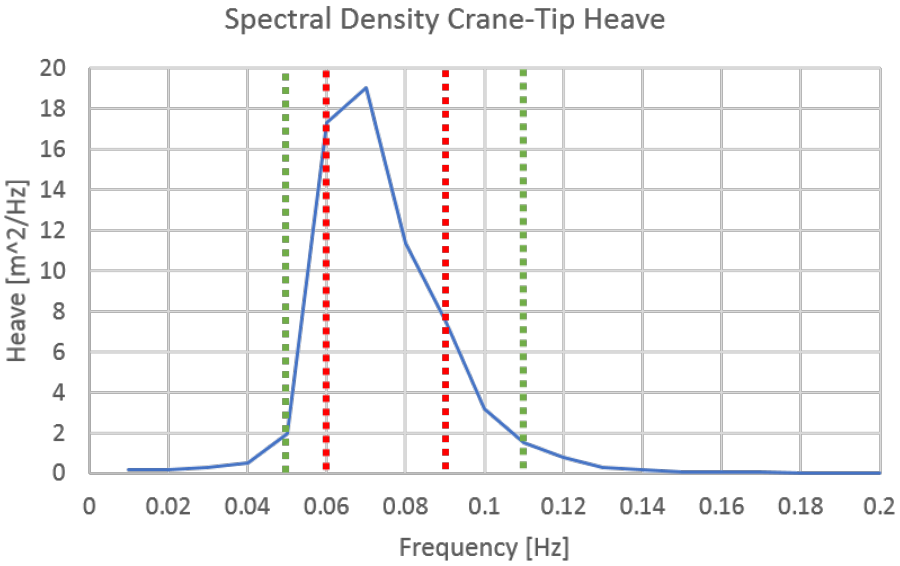


Figure 7.20: Top of the rope heave spectrum

### Natural Frequency Analysis Skips

The motion of the skips and the system is governed by the heave motion of the top of the ropes, attached to the oscillating vessel. The resulting vertical motion however also depends on the natural heave frequency of the skips. If an overlap between the energy concentration of the heave motion of the top of the rope and the natural period of the skips is seen, resonance can be expected.

The natural frequency of a lifted object suspended from a rope (the skip) is given by equation 7.1. Table 7.4 gives the masses that are required for the natural frequency calculation. $M$ and $A_{33}$ are constant for the skips on different levels, $m$ and $k$ depend on the length of the rope. $k$ is multiplied by two in equation 7.1, as the skip is hoisted by two ropes.

$$T_0 = \frac{2\pi}{\omega_0} = 2\pi\sqrt{\frac{M + A_{33} + mL}{2 \cdot k}} \tag{7.1}$$

$$k = \frac{EA}{L_0} \tag{7.2}$$

where

- M is the mass of the skip [kg]
- $A_{33}$ is the added mas in vertical direction [kg]
- m is the unit mass of the rope [kg/m]
- k is the stiffness of the rope [N/m]
- E is the elastic modulus $[kg \cdot m^{-1} \cdot s^{-2}]$
- A is the cross-sectional area $[m^2]$
- $L_0$ is the initial length of the rope [m]

| Characteristic | Full Skip | Empty Skip | Unit |
|---|---|---|---|
| M | 518.97 | 46.24 | te |
| $A_{33}$ | 73.8 | 356.54 | te |
| m | 0.358 | 0.358 | kg/m |

Table 7.4: Total mass of the skips

Equation 7.2 shows that an increase of length results in a decrease of the rope's stiffness. This results in a higher natural period for a deeper deployed skip. The natural periods of the full and empty skip systems a variable wire length is shown in Figure 7.21.

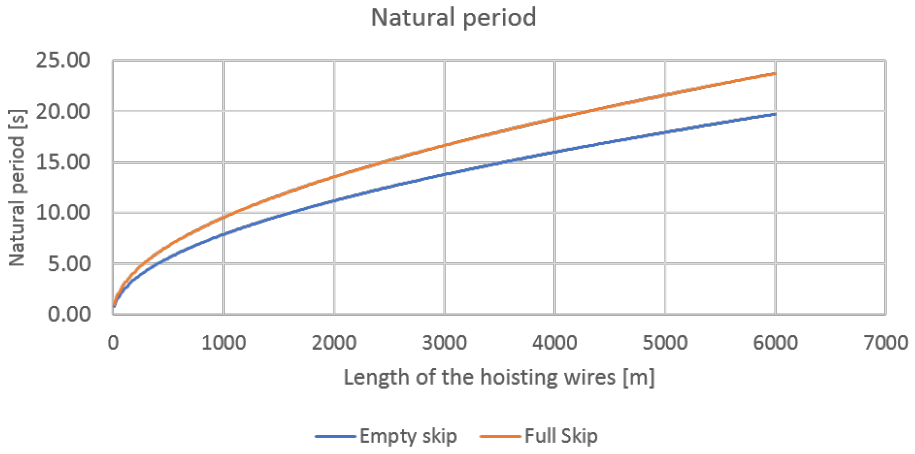


Figure 7.21: Natural period of the skips

To be able to predict the response of the skips on different elevations the natural period is converted to the eigenfrequency, so it can be compared to the heave motion in the frequency domain. This is shown in Figure 7.22. The outer limits of the heave energy frequency is given by the dashed green lines and the limits of the highest concentration of heave energy is given by the dashed red lines, corresponding with the dashed lines in Figure 7.20. This shows an overlay, which is a reason to assume that the skips will be exited within their natural frequency and resonance can occur.

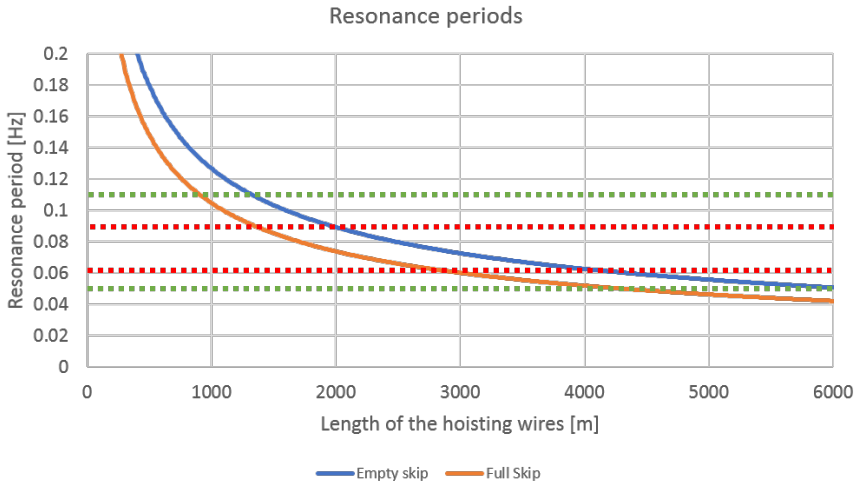


Figure 7.22: Eigenfrequency of the skips and the resonance periods

## Forced oscillation of a submerged body

The vertical motion of the skips occur due to the heave motion of the top of the rope, denoted by $\eta$ in Figure 7.23(a). The frequency of this heave motion is important because if it matches the natural frequency of the system it can result in high amplitudes of the skip. This results in dynamic tensions, which can be much higher than the static tension. The dynamic tension can also go to zero, causing slack ropes. The skip will "fall" back into the rope, causing snap loads. The response of the skip is depended on the *normalized frequency* as seen in Figure 7.23(b). The normalised frequency is the forced oscillation frequency divided by the natural frequency of the system. When the normalised frequency is one, the oscillation and the natural

frequency are the same and high amplitudes can occur.

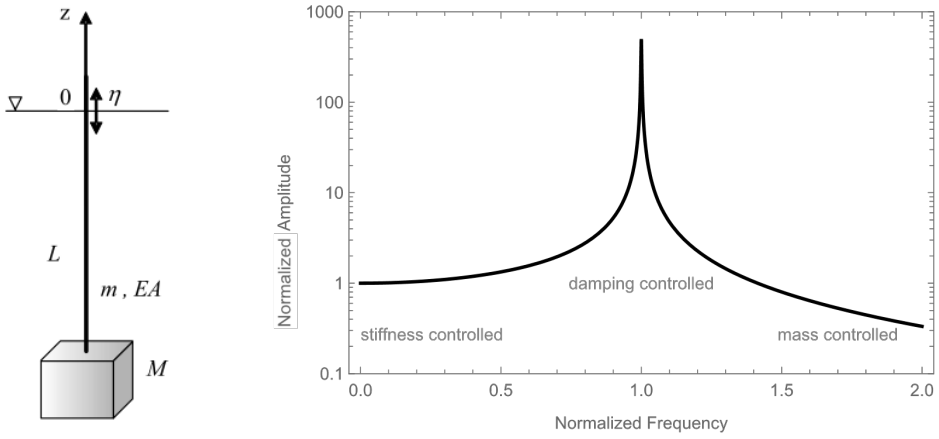


(a) Forced oscillation of a submerged lifted object in rope [59]

(b) Undamped resonance regions

Figure 7.23: Response of a submerged object in forced oscillation

This heave motion is introduced earlier and the natural frequency of the skips on different levels have been determined in the previous section. However, to get a realistic response of the skip due to the heave motion, a correct damping value is needed.

## Modelling of the damping

Structural damping is discussed in Section 5.2 and the viscous damping is discussed in Section 5.3. Together they account for the damping of the system. In this section it is discussed how these characteristics are modelled.

### Viscous Damping

The structural damping is only part of the damping that a submerged oscillating object will experience. The fluid that surrounds the object causes viscous damping and is of great significance. The viscous damping is introduced in Section 5.3, dividing it in quadratic and linear damping. Orcaflex simulates the quadratic damping by calculating the drag force each time step using the drag equation 7.3. The amount of drag in influenced by the drag coefficient. As stated in Section 5.3, the exact value of the drag coefficient is an uncertainty. The influence of the drag coefficient is shown in Figure 7.24. The vertical drag coefficient of the skip is assumed to be 0.87, as shown in Section 5.3.

$$F_z = F_D = \frac{1}{2}\rho u^2 C_{D-z} A \tag{7.3}$$

where

- u is the velocity of the skip relative to the fluid [m/s]
- $C_{D-z}$ is the vertical drag coefficient
- A is the reference area [$m^2$]

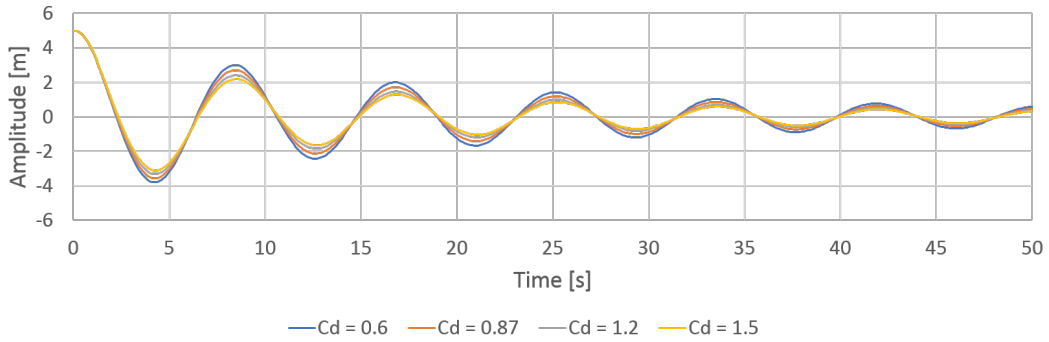


Figure 7.24: Decay tests; comparison of the drag coefficient

The linear damping is approximated with the proposed equation by DNV [59] and is added to the damping due to the drag force in vertical direction:

$$\Sigma = \frac{4}{3\pi}\rho C_{Dz} A_p \omega \eta_L \tag{7.4}$$

where

- $\rho$ is the density of seawater $[kg/m^3]$
- $C_{Dz}$ is the vertical drag coefficient [-]
- $A_p$ is the vertical drag area of the lifted object $[m^2]$
- $\omega$ is the radial frequency of the movement [rad/s]
- $\eta$ is the motion of the lifted object [m]

For both the skips, full and empty, and with a radial frequency of 0.483 rad/s (for simplicity it is assumed to be equal to the peak wave frequency $T_P = 13s$, $\omega = \frac{2\phi}{T_P}$), this gives a linear damping coefficient of 51 kN/s. Combining all these damping terms (structural, viscous quadratic and viscous linear) leads to the total damping of the system. This results in the decay test in Figure **??**. These are the damping settings that will be used for the dynamic analysis of the skips.

### Motion Analysis Skips

With all the characteristics of the system approximated to the best ability, the motion analysis of the skips can be done. It is of interest to see if the skips will resonate in the expected areas and what the resulting amplitudes and dynamic tensions will be. A full and an empty skip are simulated to be suspended from the vessel, subjected to the wave spectrum, by two reference synthetic fibre ropes, on 7 different water depths. As recommended by DNV [59], a three hour simulation period has been chosen. From these 14 different simulations, the maximum amplitude of the heave motion of the skip is derived and presented in Figure 7.35(a). This motion is normalized with respect to the heave motion of the top of the rope leading to the amplitude magnification factor, as shown in Figure 7.35(b).

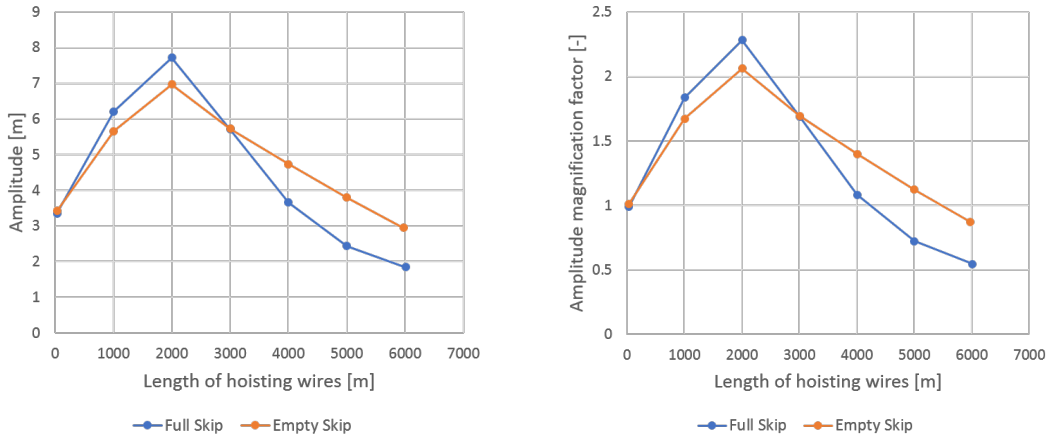


(a) Dynamic elevation of the skips

(b) Amplitude magnification factor of the skips

Figure 7.25: Dynamic response of the skips

These graphs are analyzed and compared with the expected theoretical behaviour of a forced mass-spring system as presented in Figure 7.22. This graph shows the undamped response, with a high peak if the system is excited in its natural frequency. The graph 7.26 shows the comparison of the full and empty skip that are suspended from ropes with the same length. The graph shows the normalized amplitude on the y-axis and the normalized frequency on the x-axis. The normalized frequency is determined by dividing the forced frequency on the system by the natural frequency of the system $\omega/\omega_n$. The length of the ropes determine the stiffness of the system and as linear stiffness is assumed for the simulations, both systems have the same stiffness. The damping is determined by the structural damping of the rope and the viscous damping. The structural damping was shown to be influenced by mean load and load amplitude, which will result in a difference in structural damping for the full and empty skip. The linear viscous damping is for both skips similar, as the drag coefficient is based on the shape. Quadratic damping due to drag is different for the two systems as it is also depending on the velocity of the mass, which will be different due to the difference in mass. For this example however, they are assumed to be similar. The total mass + the added mass of the full skip is about 20% more than the mass of the empty skip, resulting in a lower natural frequency, denoted in graph 7.26 by the shift to the left.
If the natural frequency of the skip is much higher than the frequency of the system $\omega < \omega_n$, the system is stiffness controlled and the amplitude will be about the same as the amplitude of the forced excitation. This is seen in Figure 7.35(b) at very low depth of the skip. As the full skip has a lower natural period for the same rope length as the empty skip, it will experience resonance at an lower depth than the empty skip. Both skip are expected to have the same maximum amplitude, but at 2000 meter water depth the full skip is excited closer to its own natural frequency than the empty skip, resulting in a higher amplitude and amplitude magnification factor. When looking at Figure 7.22, showing the overlap in spectral density of the heave motion of the top of the rope and the natural periods of the full and empty skip, the resonance peak of the full skip is expected to be around 2000 meters, while the resonance peak of the empty skip is expected to be around 2500 meters. After the resonance peak, the amplitude is mass controlled and the full skip will show a lower amplitude than the empty skip for the same rope length. This results in a maximum amplitude for the empty skip of 3 meters at the docking unit and a maximum amplitude of 1.5 meters for the full skip. This is desirable, as the skip will be at the docking unit for a considerable amount of time and here clashing with the docking unit could occur. It must be kept in mind that the 6000 meter water depth was used in this thesis as it will be the deepest working depth encountered. However, from the dynamic analysis it can be concluded that shallower water can be a bigger problem as resonance of the skips can occur whilst begin at the seafloor.

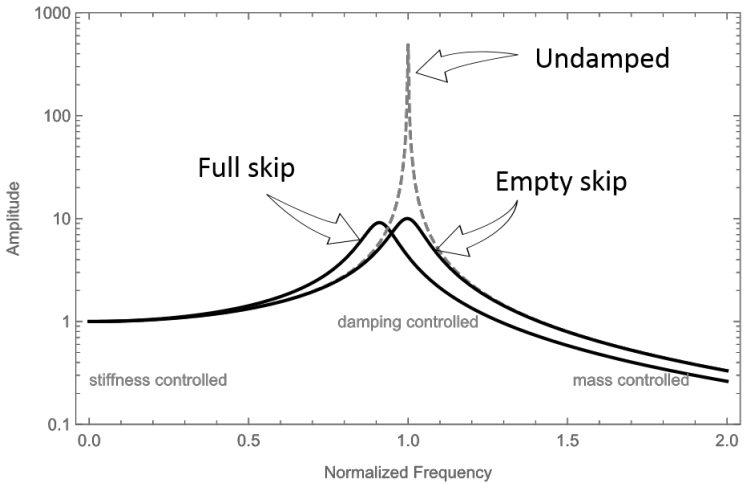


Figure 7.26: Resonance regions of the skips

Due to the amplitudes of the skips, the ropes will experience dynamic tensions. Damages to the ropes could occur if these tension get to high, therefore the maximum and minimum dynamic tension and static tension are analysed and the results are shown in Figure 7.27. Although the highest excitation of the skips is seen around 2000 meters, the highest dynamic tension in the ropes is experienced at a lower depth, around 1000 meters. The tension is a function of the stiffness and the elongation. While the elongation of the ropes is higher at 2000 meters for both skips, the ropes are twice as soft with respect to the ropes at 1000 meters. The dynamic tension shows a peak around the 1000 meters, but it can be concluded that the Minimum Breaking Force of the rope is not reached. This is visualised in Figure 7.28.
Figure 7.27(b) shows that the empty skip has a minimum dynamic tension of zero at 1000, 2000 and 3000 meters water depth (at 4000 meters it is almost 3 kN). This is due to the dynamic tension amplitude being higher than the relatively low static tension in the ropes, resulting in slack rope conditions. Here the total tension is removed from the rope due to the upward movement of the mass. This can result in snap loads and possible entanglement. The snap loads do not seem problematic from this analysis as the dynamic tension is not close to the MBF, but slack rope conditions are undesirable and are recommended to avoid. As simple solution would be to increase the mass of the skips, increasing the static tension, but it must be analysed in further design if this is a reasonable option.

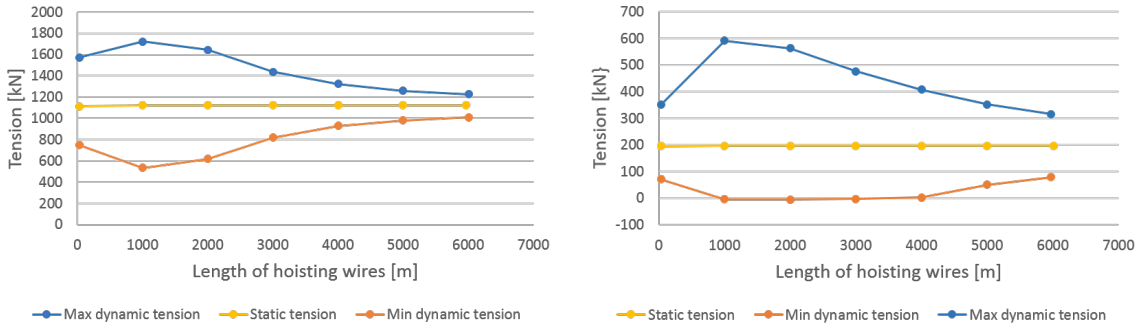


(a) Full skip

(b) Empty skip

Figure 7.27: The maximum, minimum and static tension of in the ropes

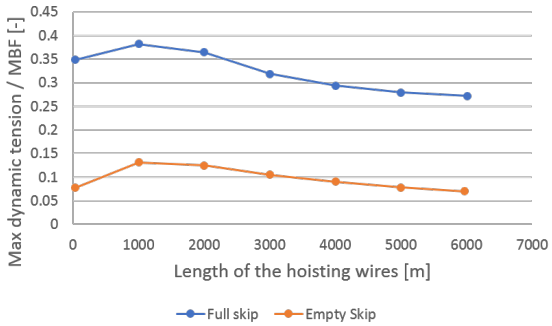


Figure 7.28: Dynamic tension with respect to the MBF

Also, the increase of damping by increasing the drag coefficient or drag area will result in lower amplitudes. This is shown in Figure 7.29. Here, a part of the time series of the dynamic tension of the empty skip at 4000 meters is shown. At 9732 seconds the ropes of the empty skip with the standard characteristics experiences the minimal tension, which value is used in Figure 7.27(b). The dynamic tension of the ropes of the same skip but with a vertical drag coefficient ($C_{D-z}$) that is three times as large (0.87 $\Rightarrow$ 2.61) is shown in Figure 7.29. Due to this increase in the drag coefficient, the minimum tension is increased from 3 kN to 32 kN. The same test has been done for the empty skip suspended from 1000 meters of rope, as shown in Figure 7.30, which has a higher tension amplitude. Theincrease of the drag coefficient shows a decrease of the tension amplitude, but not sufficient to prevent slack rope conditions.

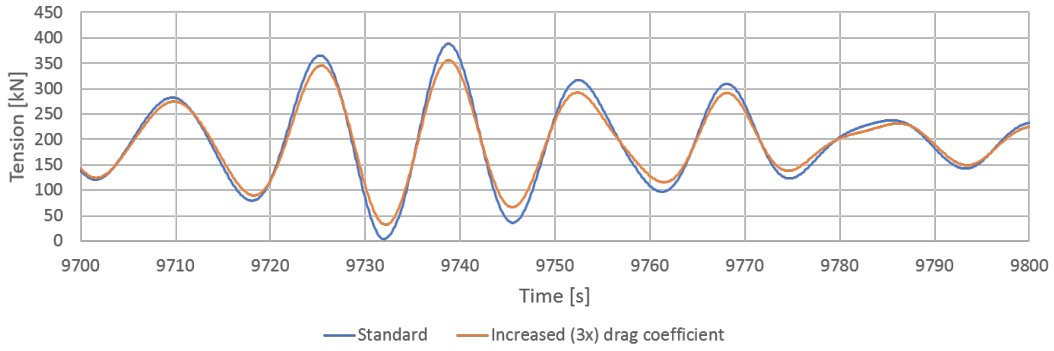


Figure 7.29: Dynamic tension of an empty skip at 4000 meters with different drag coefficients

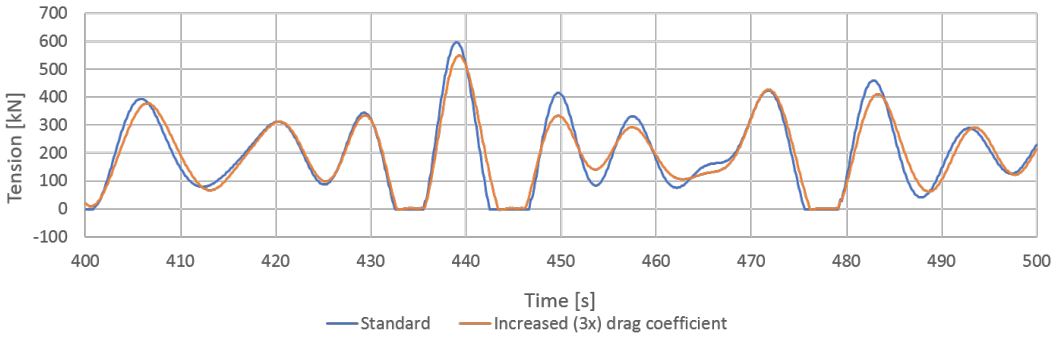


Figure 7.30: Dynamic tension of an empty skip at 1000 meters with different drag coefficients

During normal operations, the skips will never be at the same water depth for three hours. A full skip is hoisted from the SPT to the surface with a speed of 2 m/s and the empty skip is lowered back to the SPT with the same speed. This is simulated in Orcaflex, resulting in the dynamic tension in the hoisting wires as seen in Figure 7.31. This shows that the full and empty skip are mostly excited in the upper half of the water column.

The hoisting wires of the empty skip experience slack conditions at various places along the way down.

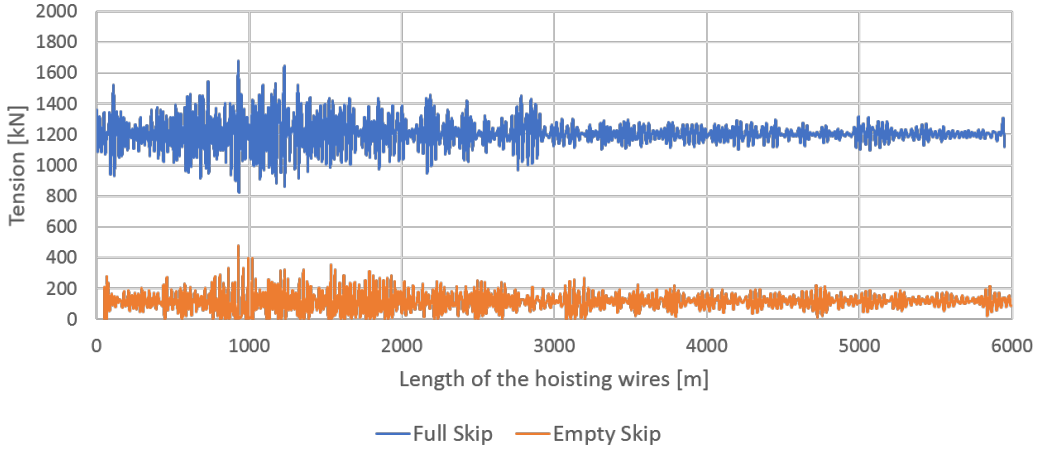


Figure 7.31: Dynamic tension of the skips during lowering and hoisting

Increasing the weight of an empty skip will increase the static tension resulting in slack rope conditions less likely to occur. The weight can be increased by increasing the steel thickness of the skip. This will also result in a higher tension in the ropes of the full skip. The weight of the skip has been increased to a level where slack rope conditions no longer occur during the lowering of the empty skip. The values of these heavier skips are shown in Table 7.5. The dynamic tension in the hoisting wires of the skip with increased weight is shown in Figure 7.32. The maximum dynamic tension of the full skip is also increased but still less than half of the MBF. This makes increasing the weight of the empty skip a promising solution.

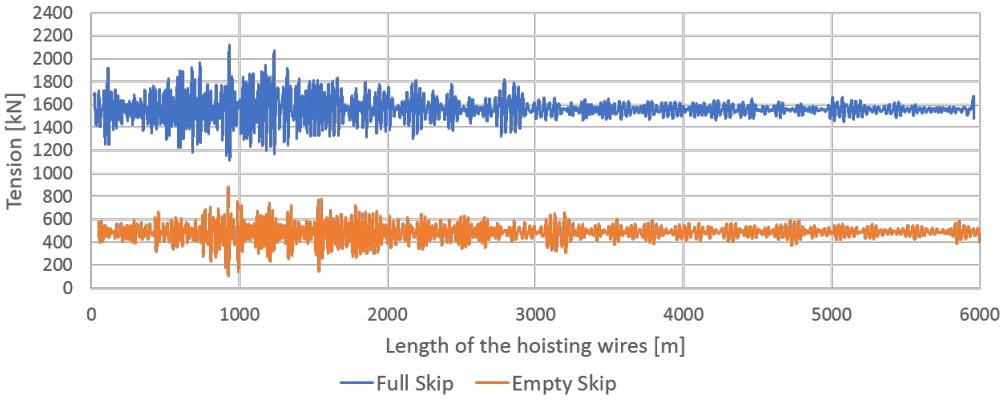


Figure 7.32: Dynamic tension of the heavier skips during lowering and hoisting

*Initial values*

| Characteristic | Value | Value | Unit |
|---|---|---|---|
| | **Full Skip** | **Empty Skip** | |
| Average steel thickness | 0.025 | 0.025 | [m] |
| Mass in air | 518.97 | 46.24 | [t] |
| Submerged mass | 223.12 | 40.20 | [t] |

*Increased weight values*

| | **Full Skip** | **Empty Skip** | |
|---|---|---|---|
| Average steel thickness | 0.065 | 0.065 | [m] |
| Mass in air | 592.97 | 122.07 | [t] |
| Submerged mass | 288.78 | 106.46 | [t] |

Table 7.5: The effect on the skip mass of increasing the steel thickness

### Motion Analysis Docking Unit

In Section 6.1 the asymmetrical loading of the guidance wires is introduced. Due to a hinge between the harvester and the ladder and a hinge between the ladder and the docking unit, the front guidance wires have higher tension than the aft wires when the vessel is not moving. In this section the motion of the SPT due to the vessel motions will be analysed. The same time series and rope characteristics are used. For simplicity the skips have been kept out of this model. The damping of the SPT is split in quadratic damping and linear damping. The quadratic damping is again calculated by Orcaflex with the values presented in Section 6.1 and the linear damping is calculated with equation 7.4. It differs with the skip due to the drag coefficient and the reference area.

The motion analysis of the docking unit shows a high inclination of the docking unit whilst in a high simulated sea state, as shown in Figure 7.33. It shows an amplitude of more than $25^o$ at max. A high inclination of the docking unit is undesired during operations, as the skips can't leave / enter the docking unit if it is inclined above a certain angle. In addition, clashing of the docking unit into the skips could occur and frequent motions of the docking unit can lead to fatigue damage. Figure 7.34 shows a smaller time-frame (indicated in Figure 7.33 with the red box) and gives the elevation of the front and the aft of the docking unit. It can be seen that the aft of the docking unit has a much higher amplitude with respect to the equilibrium position. The ladder is attached to the front of the docking unit with a hinge, giving the front more inertia and initial tension in the wires. This leads to the high inclination of the docking unit.

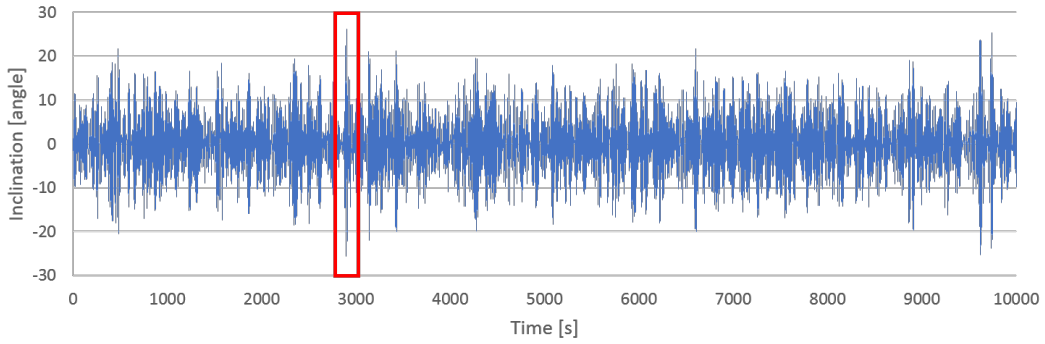


Figure 7.33: Inclination of the docking unit

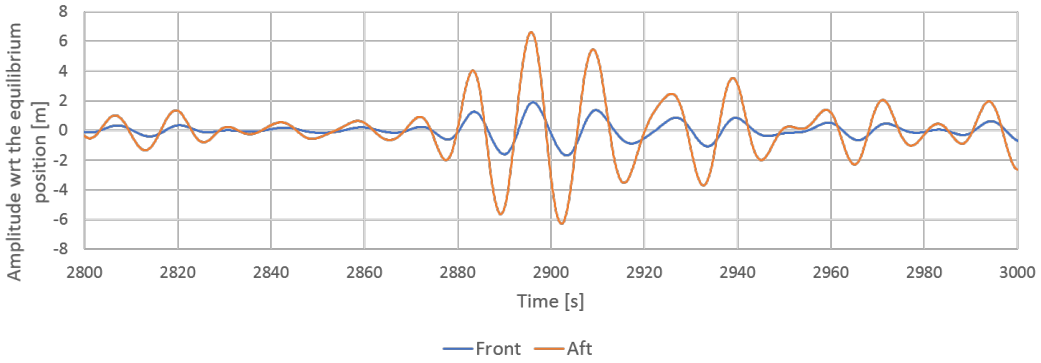


Figure 7.34: $Z$-position of the front and aft of the docking unit

From this analysis it can be concluded that the docking unit can be subjected to large motions due to the vessel motions and the initial asymmetrical loading, despite having a large submerged surface and inertia. It is recommended to research the possibilities to prevent these large pitch motions. Symmetrical loading by attaching the ladder to the middle of the docking unit could be option. A visualisation of such a concept is shown in Figure 7.35.

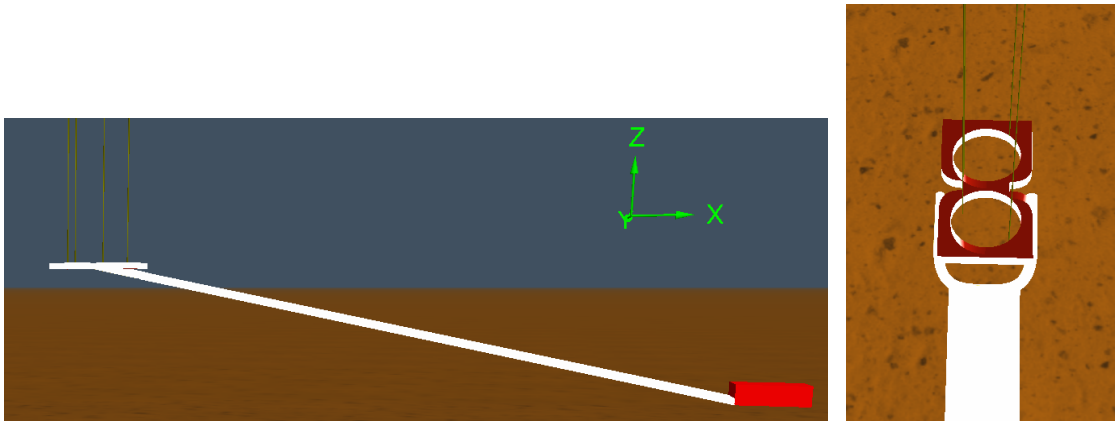


(a) Side view of the SPT

(b) Topview of the docking unit

Figure 7.35: Symmtrical loading of the docking unit

### Vortex Induced Vibrations

VIV ordinarily occurs over a specific velocity range, which can be expressed with an empirical relation including the reduced velocity $V_R$ as seen in equation 7.5 and 7.6 [59]:

$$3 < V_R < 16 \tag{7.5}$$

$$V_R = \frac{U}{f_n D} \tag{7.6}$$

where

- U is the relative velocity between forward velocity and current [m/s]
- $f_n$ is natural frequency [Hz]
- D is the rope diameter [m]

The different eigenmodes of the wires are calculated with Orcaflex and compared to the reduced velocity range where vortex induced vibrations can occur. This is shown in Figure 7.36. It can be seen that a part of the eigenfrequencies of all of the ropes in the system will meet the requirements for vortex-induced-vibrations.

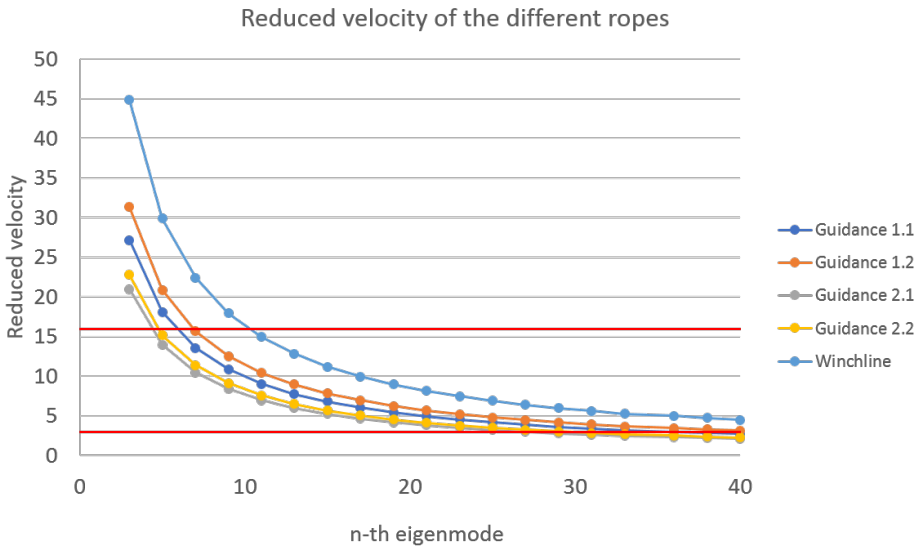


Figure 7.36: Vortex Induced Vibration ranges

There are several effects that VIV can have on flexible ropes [25]:

- The system may experience fatigue damage do to resonance vibrations
- Drag amplification: Increased mean drag coefficient of the rope increasing the drag force on the system. In literature several expressions are given for the increase in drag coefficient, based on the estimated VIV amplitude and the diameter of the member [58]. From these expressions it can be concluded that with the right circumstances the drag coefficient $C_D$ can double from 1.2 to 2.4. This leads to an increase in the offset and an increase in the horizontal force on the ship, as seen in Figure 7.6.
- Possible rope clashing. The maximum VIV displacement of a rope can be in the order of one diameter for each rope. Therefore, to avoid collision, the minimum spacing between the ropes needs to be twice the diameter (0.16 m in this concept). As can be seen in Figure 5.1, are connected to the docking unit with at least 2.76 meters space between them. However, due to current and operations the ropes can get closer.

| | Drag Coefficient | | Unit |
|---|---|---|---|
| | **1.2** | **2.4** | [-] |
| **Position of the Docking Unit** | -104.26 | -197.62 | m |
| **X-Force on vessel** | -208.01 | -407.38 | kN |

Table 7.6: Results of drag amplification due to VIV

VIV of the skip could also occur, although the skip will not be a smooth cylinder, due to attachments like the eyelets. This prevents the fluid to flow freely around the skip, decreasing the likeliness of VIV to occur. Besides the horizontal flow of fluid due to the forward velocity and current flow, a vertical flow of fluid is present as the skips are hoisted and lowered. This could also lead to VIV, but is not researched in this thesis. Only a preliminary investigation of possible vortex induced vibrations has been done. It can be concluded that VIV might occur, but to what extent and what will be the effect is unclear. Therefore it is recommended to thoroughly assess the whole system.

# 8

# Conclusions and Recommendations

## 8.1. Conclusions

The objective of this research project is to provide preliminary look into the behaviour of the mechanical lifting system, consisting of skips hoisted and lowered by synthetic fibre ropes, for the vertical transportation of polymetallic nodules in a water depth of 6000m.Where most deep-sea mining developments are considering hydraulic vertical transport with a riser, Boskalis introduces a concept that utilizes mechanical lifting for the vertical transport. The mechanical lifting system is relatively simple and uses mostly proven technologies, except from the fact that lifting operations have never taken place in this water depth. Besides simplicity, Boskalis came up with this concept due to promising efficiency and the advantage to have most of the power units above water. This way, more problems and failures can be assessed without retrieving the whole system from the seabed and achieve a higher workability.
The system consists of the Seafloor Production Tool (SPT), which collects the polymetallic nodules, the Vertical Transport System (VTS), which transports the nodules up to the Production Support Vessel (PSV). The main interest in this thesis is the VTS, which consists out of two skips and eight wires. Each skip is hoisted by two hoisting wires and has eyelet through which the guidance wires run. These guidance wires are in place to control the position of the docking unit and the location of the skip with respects to the docking unit and the vessel. Knowledge on the subject of vertical transport by means of mechanical lifting in deep-sea mining is very scarce, but there is overlap with other operations to retrieve information from, like the expected dynamics from deep-sea lifting and synthetic fibre rope characteristics from mooring systems. The system is assessed using Orcaflex, a hydrodynamic analysis software program.

#### Preliminary Research

The deep-sea mineral of interest is the polymetallic or manganese nodule. High concentrations are found on abyssal planes of the Pacific Ocean. The location of interest in this research is the Clarion-Clipperton Zone. The water depths reach from 3000 to 6000 meters. Assuming the deepest water results in the most extreme conditions, the 6000 meter case is taken as the starting position in this research. Mining at these undiscovered depths raises questions about the possible environmental impact. From the preliminary research it is concluded that the impact of deep-sea mining may possibly be a looming showstopper. Therefore it is expected that reducing of the environmental impact will be an important part of further deep-sea mining engineering. However, the environmental matters are versatile and complex and are not considered part of this study.

#### Environmental Data

The system is exposed to the environmental forces due to current and waves. The current at the Clarion-Clipperton Zone is characterised by surface currents (0-200 meter depth) of about 1 m/s. Below this surface current a constant current of 0.1 m/s is assumed. Different current directions exist at different water levels, but an unidirectional current profile is assumed, as it will generated most drag. The drag on the system (which has eight 6000 meter long ropes through the water column) was thought to be of great influence, but calculations on the stationairy system have shown that it results in relatively low forces and offset of the system. As high workability is desired, a Pierson-Moskowitz wave spectrum with a significant wave height of 3.5 meters and a peak period of 13 seconds is taken as reference for the Clarion-Clipperton Zone.

#### Forward Velocity

The initial forward velocity of 1 m/s however, proved itself unrealistically high. The drag forces would reach above the 2000 kN that should be accounted for by the vessel. More important, the offset of the SPT would be more than 2000 meters, making reliable position handling impossible. Therefore it is decided to reduce the forward velocity to 0.1 m/s.

#### Wire Frame

Although the reduction of forward velocity improves the circumstances for the Vertical Transport System, entanglement of the ropes is still a feasible problem. It is shown that the full skip has less natural offset than the SPT, which is in some situations resulting in the full skip "falling" through the guidance wires associated with the other skip. This can result in entanglement and snapping of the ropes when the skip is continued to be lifted. Therefore the wire frame is brought into this concept, spreading the guidance wires as it is lifted together with the skip. Although now all the wires interact with an eyelet every cycle, the force per eyelet is less, as the total force is divided by the eyelets. This system eliminates the possibility of entanglement, but increases the lift drag and mechanical complexity of the system.

#### Synthetic Fibre Rope

It is concluded that steel wires are inefficient for the vertical transport by means of mechanical lifting, as they have no safe working load at the working depth in this thesis. Therefore the applicability and characteristics of synthetic fibre rope, more specifically Dyneema, is analysed. Synthetic fibre rope looks very promising, but more understanding about wear, fatigue, damping, internal heating and handling is needed to confidentially use it in these operations. This is discussed in more detail in Section 8.2.2.

#### Dynamic Analysis

It is assumed that the PSV will keep position using a dynamic positioning system and is able to keep the bow within 30 degrees of the wave direction. The calculated vessel motion due to the wave spectrum ($H_S$=3.5 m and $T_P$=13s) will result in crane-tip heave motion. During the lowering/lifting of a skip, the eigenfrequency of the isolated mass-spring system (skip suspended from the ropes) changes due to changing length of the ropes. It can be seen from the dynamic analysis results that the skip will be excited not only at its natural frequency, but experiences resonance in the upper half of the water column. Both skips systems, full and empty, have a very low stiffness at the full 6000 meter water depth, due to the long rope length. This results in a lower heave amplitude of the skip than the heave amplitude of the top of the rope. Low heave motion of the skip is desired mostly at the seabed, because of possible interaction with the SPT. The hoisting wires of the empty skip become slack frequently due to resonance in the upper half of the water column, resulting in undesired snaploads. Although dynamic tensions are experienced, the maximum tension is only 40% of the MBF, ensuring the integrity of the ropes.
The docking unit is situated at 20 meters above the seabed and is kept at this location by the four guidance wires. The docking unit is loaded asymmetrical due to the hinged connection of the ladder. This leads to a difference in tension in the guidance wires in order to keep the docking unit horizontal. However, when the top of these guidance wires are experiencing heave motion, the tensioning of the guidance wires is no longer proportional to the equilibrium state that was attained in a more static situation. From the simulations it is concluded that the docking unit in the current setup will experience pitch movements, which is undesirable during operations. A possible solution is to load the docking unit symmetrical by attaching the transport to the center of the docking unit.

**Summary**

In this thesis a broad analysis of the vertical transportation by means of mechanical lifting for deep-sea polymetallic nodules is done. Some improvements have been made to the concept. It is a very broad subject, in which many interesting research subjects are left. This thesis is an early engagement with this concept and therefore the choice has been made to give a broad overview of the whole system instead of performing detailed engineering of a single subject. From this thesis it can be concluded that the concept shows to be promising, but that a lot of work still has to be done. This will be discussed in the next section, Recommendations.

## 8.2. Recommendations

### 8.2.1. Seabed Interaction

Values are derived for the horizontal force on the harvester, but no reference is made to the traction it might have. Research should be done to see if it is expected if the harvester will be able to stay on track with the forces it experiences during operations. The upper layer of the seabed is known to be very aqueous, which can results in problems with track keeping.

### 8.2.2. Synthetic fibre rope experiments

Synthetic fibre ropes have been introduced in the offshore industry, but there are knowledge gaps (regarding wear, fatigue, damping, internal heating and handling) for the purpose as proposed in this thesis. In a later stage, it is recommended to collaborate with the rope manufacturer for a combination of rope experiments.

**Decay test with regards to the damping**

Synthetic fibre ropes have been used and tested, but mostly as mooring lines. Synthetic fibre ropes used for deep-sea lift operations are not common and good test results are absent. One of the problems of the non-linear behaviour of the synthetic fibre ropes is its dependence on many input parameters. To get insight in the behaviour of the 80 mm Dyneema rope that is used in this thesis, experiments are recommended. One of these experiments should be a decay test, to derive a value for the energy dissipation of the rope per oscillation. Experiments with comparable rope lengths and weights are costly and inconvenient. However, experiments on a smaller scale could be performed, as long as the normalized mean load and normalized amplitude are the same. The 80 mm Dyneema rope that is used as reference in this thesis, is also fabricated in a much smaller diameter. The smallest diameter it is fabricated in is 6mm. This ropes has a MBF of 35 kN, leading to a representative load of 350 and 900 kilograms for the experiments. With this set-up the structural damping can be investigated. The influence of the length of the ropes can be tested and although 100's of meters of rope is still inconvenient, the effect on damping and stiffness by increasing the rope length can be tested.

| | **Normalised mean load [%]** | **MBF 6 mm [kN]** | **Experiment load [kg]** |
|---|---|---|---|
| **Empty Skip** | 10 | 35 | 356.78 |
| **Full skip** | 25 | 35 | 891.95 |

Table 8.1: Decay test experiment set-up

**Fatigue due to the eyelet - rope interaction**

The interaction force between the eyelet of the skip and the guidance wire is retrieved from the Orcaflex simulations, but no reference to the corresponding fatigue is included in this thesis. The eyelet - rope interaction force should be used as input in the wear tests of the rope that will be used during operations. Besides these tests, there are many options with regards to the eyelet for improving the friction coefficient. This way the impact of the interaction force can be reduced. Solutions that can be thought of are a smooth bellmouth shaped eyelets or a rope container with roller bearings to guide the rope.

#### Heat generation with in the ropes during the handling

Dyneema is known to have a low melting temperature. The fibre rope may fail if it is bent and straitened repeatedly for a significant duration. This failure mode is a combination of material degradation due to tension fluctuations and internal heating up of the fibre rope during handling at the PSV. Research has been done in this area, but this is not assessed in this thesis. To grasp the whole picture of this deep-sea mining system this will need to be included and possibly further researched. For this subject also applies that the non-lineair behavior of the synthetic fibre rope makes it unpredicable. Therefore it is recommended to test the specific rope type that will be used to exclude unexpected issues.

### 8.2.3. Dynamics

The dynamics of the skips and the docking unit due to the vessel motion have been simulated, but further research is recommended on several subjects.

#### Docking Unit - Skip interaction

The dynamic behaviour of the docking unit and the full and empty skips have been assessed separately in this thesis. The docking unit shows considerable pitch movement while the skips at 6000 meters depth also have a heave amplitude of 1.5 meters. It is recommended for further research to assess the possible clashing of the docking unit and the skips entering or leaving. Besides that, the combined motion of a docked skip in the docking unit is recommended to be assessed. It has been stated that the hoisting wires should carry most of the increasing weight of the skips being filled, ensuring the least amount of dynamic tension on the guidance wires. But it is likely that a certain amount of weight of the skip is resting on the docking unit, creating a connection that is less easy to neutralize and thereby preventing "bouncing" of the skip in the docking unit.

#### Splash Zone

Every production cycle a skip is lifted through the waterline, emptied at the vessel and lowered through the waterline again. The focus in this research is the submerged behaviour, but the splash zone is an area of interest. The splash zone is defined as the zone were the transition from water to air and air to water is made during the vertical transport. The buoyancy is no longer constant, but depending on the part of the body (skip) that is still submerged. The tension in the hoisting wires will increase when lifting the skip out of the water, due to the disappearing of this buoyant force.

#### Lifting and Lowering of the whole VTS and SPT

When arriving at or leaving from the mining location, the whole subsea equipment will be suspended from the ship, as seen in Figure 8.1. The effects of the drag due to current is recommended to be investigated, as rotating of the system, also due to changing current direction over depth is present, could occur.

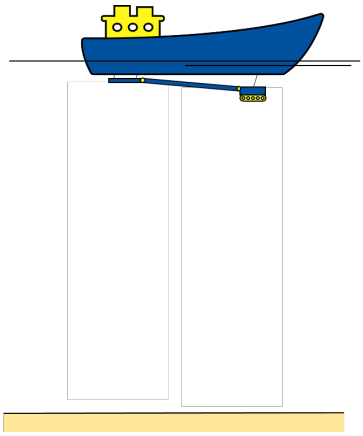

Figure 8.1: Lowering subsea equipment

#### Reduce the sensitivity of the docking unit

The docking unit will experience pitch movement due to dynamic loading. It is recommended to investigated different set-ups of the docking unit connection to decrease this undesired movement, A more symmetrical loading is proposed, by connection the ladder to the middle of the docking unit instead of the most forward side. An investigation of the natural frequency of the SPT can be done. Using a different type of synthetic fibre rope could than be used to alter the natural frequency (probably to make the system even softer) to decrease the motions of the docking unit

### 8.2.4. Operations

Whilst this deep-sea mining system is still in the conceptual phase, detailed operations have not been part of the scope of this thesis. However, ideas about the operations have come up during the project and are discussed here.

#### SPT control

The SPT will be operating 6000 meters below the surface, but controlled from the PSV. In a way, it does not matter how far below the surface the SPT is, as soon it in out of sight it needs to be remotely observed and controlled. Observation can be done with cameras, for which also artificial light is needed as no sunlight reaches the bottom of the sea. Cameras on the docking unit could monitor the SPT and the skips, providing guidance when for instance docking the skips. A good addition to cameras could be distance sensors on the docking unit and the harvester, to measure the distance to for example the seafloor.

#### Docking of the skips

A crucial part of the cycle is the docking of the skip at the docking unit. The skip must land and leave the docking unit with ease, as high, cyclic interaction forces due to clashing should be prevented. Control support systems like the stated cameras and sensors could come in handy with regards to the landing of the skips as well.

#### Deck capacity

As mentioned in chapter 5, the extremely long ropes require substantial winch installations. Eventually further engineering is needed to investigate these winch systems and see if it is manageable to get all these systems on the ship.

#### Seafloor mapping

In this thesis, a flat seabed is assumed. In reality, the seafloor consists of flat-floored abysses, but separated by hills, seamount and ridges. Before operations can commence, surveys need to be done to assess the seafloor. Effort should be made to create the most efficient harvesting path, based on bathymetry and abundance of nodules.

### 8.2.5. Environmental Impact

It is without doubt that the seabed has rich resources of minerals and that companies can come up with the technology needed to retrieve them to the surface. It will be the environmental impact of deep-sea mining that can eventually put a hold on the liveability of the deep-sea mining industry. Research must be done to minimize the environmental impact due to turbidity and the removing of the upper layer of the seafloor.

# A

# Vessel Data

**Geometrical Hullform Data**

| | | | |
|---|---|---|---|
| | Actual Midship Draft (T) | 10 | m |
| | Actual Trim By Stern | 0 | m |
| | | | |
| | Length Between Perpendiculars | 249.999 | m |
| | Rear Section To A.P.P | 6.297 | m |
| | | | |
| **Waterline** | Length (Lwl) | 256.284 | m |
| | Beam (B) | 43 | m |
| | Area | 9185 | m2 |
| | Area Coefficient (Lpp) | 0.8544 | |
| | Area Coefficient (Lwl) | 0.8335 | |
| | Centroid To A.P.P. | 130.326 | m |
| | Centroid To Rear Section | 136.624 | m |
| | | | |
| **Displacement** | Volume | 88196 | m3 |
| | Mass | 90401 | ton |
| | Blockcoefficient (Lpp) | 0.8204 | |
| | Blockcoefficient (Lwl) | 0.8003 | |
| | Centroid To A.P.P. | 131.817 | m |
| | Centroid To Rear Section | 138.115 | m |
| | Centroid To Waterline | 4.885 | m |
| | Centroid To Keelline | 5.115 | m |
| | Midship Section Coefficient | 0.9907 | |
| | Long. Prismatic Coefficient | 0.8282 | |
| | Vert. Prismatic Coefficient | 0.9602 | |
| | Ratio Lpp/B | 5.814 | |
| | Ratio Lwl/B | 5.96 | |
| | Ratio B/T | 4.3 | |
| | Wetted Surface Hull | 12975 | m2 |

| **Stability Parameter** | | |
|---|---|---|
| KB | 5.115 | m |
| KG | 15 | m |
| OG | 5 | m |
| KM-Transverse | 19.384 | m |
| BM-Transverse | 14.269 | m |
| GM-Transverse | 4.384 | m |
| KM-Longitudinal | 419.691 | m |
| BM-Longitudinal | 414.576 | m |
| GM-Longitudinal | 404.691 | m |

# Bibliography


[1] Major Oceanic Gyres and Sea Currents | The Geography of Transport Systems. URL https://transportgeography.org/?page_id=360.

[2] World Population Prospects The 2017 Revision. Technical report. URL https://esa.un.org/unpd/wpp/Publications/Files/WPP2017_KeyFindings.pdf.

[3] Chapter 4 Deep-water bottom currents. *Handbook of Petroleum Exploration and Production*, 2006. ISSN 15678032. doi: 10.1016/S1567-8032(06)80023-6.

[4] Deep-sea Mining: The Basics Overview. Technical report, 2018.

[5] "Why the Rush? Seabed Mining in the Pacific Ocean". *Deep Sea Mining Campaign, London Mining Network, Mining Watch Canada,,* July:22, 2019. URL http://www.deepseaminingoutofourdepth.org/wp-content/uploads/Why-the-Rush.pdf%0A%0A.

[6] B Agarwal, P Hu, M Placidi, H Santo, and J J Zhou. *Feasibility Study on Manganese Nodules Recovery in the Clarion-Clipperton Zone*. ISBN 9780854329496.

[7] Donald W. Allen. Vortex-induced vibration of deepwater risers. In *Proceedings of the Annual Offshore Technology Conference*, volume 2, pages 209–216. Offshore Technol Conf, 1 1998. doi: 10.4043/8703-ms.

[8] American Bureau of Shipping. GUIDANCE NOTES ON THE APPLICATION OF FIBER ROPE FOR OFFSHORE MOORING. 2011(February), 2014.

[9] Yong Bai and Qiang Bai. Chapter 10 - Subsea Risk and Reliability BT - Subsea Engineering Handbook. pages 267–291. Gulf Professional Publishing, Boston, 2010. ISBN 978-1-85617-689-7. doi: http://dx.doi.org/10.1016/B978-1-85617-689-7.10010-X. URL http://www.sciencedirect.com/science/article/pii/B978185617689710010X.

[10] Helen Bailey, Bridget Senior, Dave Simmons, Jan Rusin, Gordon Picken, and Paul M. Thompson. Assessing underwater noise levels during pile-driving at an offshore windfarm and its potential effects on marine mammals. *Marine Pollution Bulletin*, 60(6):888–897, 6 2010. ISSN 0025-326X. doi: 10.1016/J.MARPOLBUL.2010.01.003. URL https://www.sciencedirect.com/science/article/pii/S0025326X10000044.

[11] Kenneth R. Bitting. DYNAMIC MODELING OF NYLON AND POLVESTER DOUBLE BRAID LINE. *Journal of Chemical Information and Modeling*, 53(9):1689–1699, 1985. ISSN 1098-6596. doi: 10.1017/CBO9781107415324.004.

[12] Robert D. (Van Nostrand Reinhold) Blevins. Flow-Induced Vibration, 1990.

[13] Bluemining. Breakthrough Solutions for Mineral Extraction and Processing in Extreme Environments. 2018.

[14] Fernando P. Carvalho. Mining industry and sustainable development: Time for change. *Food and Energy Security*, 6(2):61–77, 2017. ISSN 20483694. doi: 10.1002/fes3.109.

[15] Bernd Christiansen, Anneke Denda, and Sabine Christiansen. Potential effects of deep seabed mining on pelagic and benthopelagic biota. *Marine Policy*, 2 2019. ISSN 0308-597X. doi: 10.1016/J.MARPOL.2019.02.014. URL https://www.sciencedirect.com/science/article/pii/S0308597X18306407.

[16] Jin S. Chung. Advance in Deep-Ocean Mining Systems Research. *The International Society of Offshore and Polar Engineers*, 1994. ISSN 03015629. doi: 10.1016/j.ultrasmedbio.2006.02.1052.

[17] G. F. Clauss, H. Weede, and T. Riekert. Offshore pipe laying operations - Interaction of vessel motions and pipeline dynamic stresses. *Applied Ocean Research*, 14(3):175–190, 1992. ISSN 01411187. doi: 10.1016/0141-1187(92)90013-A.

[18] Günther Clauss. Offshore Structures: Volume I: Conceptual Design and Hydromechanics.

[19] Patrick Colman Collins, Peter Croot, Jens Carlsson, Ana Colaço, Anthony Grehan, Kiseong Hyeong, Robert Kennedy, Christian Mohn, Samantha Smith, Hiroyuki Yamamoto, and Ashley Rowden. A primer for the Environmental Impact Assessment of mining at seafloor massive sulfide deposits. *Marine Policy*, 42:198–209, 2013. ISSN 0308597X. doi: 10.1016/j.marpol.2013.01.020.

[20] D. S. (David Spencer) Cronan. *Handbook of marine mineral deposits*. CRC Press, 2000. ISBN 084938429X. URL `http://www.vliz.be/en/imis?module=ref&refid=9079&printversion=1&dropIMIStitle=1`.

[21] Peter Davies, Michel François, Francois Grosjean, Patrice Baron, Karine Salomon, and Damien Trassoudaine. Synthetic Mooring Lines for Depths to 3000 Meters. *Proceedings of the Annual Offshore Technology Conference*, (May 2016):2225–2233, 2002. ISSN 01603663. doi: 10.4043/14246-ms.

[22] Peter Davies, Yvan Reaud, Loic Dussud, and Patrice Woerther. Mechanical behaviour of HMPE and aramid fibre ropes for deep sea handling operations. *Ocean Engineering*, 38(17-18):2208–2214, 12 2011. ISSN 00298018. doi: 10.1016/j.oceaneng.2011.10.010. URL `https://linkinghub.elsevier.com/retrieve/pii/S0029801811002411`.

[23] Karel Devos, Carina De Plukker, and Peter Van Den Berghe. Experiences in rope design for offshore renewable energy projects. *Proceedings of the 16th Offshore Symposium - Energy from the Oceans*, pages 75–83, 2010.

[24] Maritime Division. Lankhorst Ropes Maritime Catalogue.

[25] DNV-RP-F203. Det Norske Veritas - Riser Interference. (April), 2009.

[26] Ivo Dreiseitl and Roman Bednarek. Physical Properties of Polymetallic Nodules and Deep Sea Sediments , as Determined with Different Analytical Techniques Physical Properties of Polymetallic Nodules and Deep Sea Sediments , as Determined with Different Analytical Techniques. (June 2011), 2011.

[27] ECORYS Nederland BV. Study to investigate state of knowledge of Deep Sea Mining. (March):1–272, 2014.

[28] John F. Flory, Stephen P. Banfield, and David J. Petruska. Defining, measuring, and calculating the properties of fiber rope deepwater mooring lines. *Proceedings of the Annual Offshore Technology Conference*, 1(April 2015):151–164, 2004. ISSN 01603663. doi: 10.4043/16151-ms.

[29] Wenjun Gao, Daniel Nelias, Yaguo Lyu, and Nicolas Boisson. Numerical investigations on drag coefficient of circular cylinder with two free ends in roller bearings. *Tribology International*, 2018. ISSN 0301679X. doi: 10.1016/j.triboint.2018.02.044.

[30] Sabine Gollner, Stefanie Kaiser, Lena Menzel, Daniel O.B. Jones, Alastair Brown, Nelia C. Mestre, Dick van Oevelen, Lenaick Menot, Ana Colaço, Miquel Canals, Daphne Cuvelier, Jennifer M. Durden, Andrey Gebruk, Great A. Egho, Matthias Haeckel, Yann Marcon, Lisa Mevenkamp, Telmo Morato, Christopher K. Pham, Autun Purser, Anna Sanchez-Vidal, Ann Vanreusel, Annemiek Vink, and Pedro Martinez Arbizu. Resilience of benthic deep-sea fauna to mining activities, 8 2017. ISSN 18790291. URL `http://www.ncbi.nlm.nih.gov/pubmed/28487161`.

[31] Matthias
Haeckel. Mining Impact; Environmental Impacts and Risks of Deep-Sea Mining. (October), 2018.

[32] James R. Hein, Kira Mizell, Andrea Koschinsky, and Tracey A. Conrad.
Deep-ocean mineral deposits as a source of critical metals for high- and green-technology applications: Comparison with land-based resources. *Ore Geology Reviews*, 51:1–14, 2013. ISSN 01691368. doi: 10.1016/j.oregeorev.2012.12.001. URL http://dx.doi.org/10.1016/j.oregeorev.2012.12.001.

[33] J.R. Hein and A. Koschinsky. Deep-Ocean Ferromanganese Crusts and Nodules. *Treatise on Geochemistry*, pages 273–291, 1 2014. doi: 10.1016/B978-0-08-095975-7.01111-6. URL https://www.sciencedirect.com/science/article/pii/B9780080959757011116?via%3Dihub.

[34] David
Heydon. Exploration for and Pre-feasibility of mining study Nautilus Minerals Ltd. (September), 2004.

[35] HOERNER and S. F. FLUID-DYNAMIC DRAG. *Hoerner Fluid Dynamics*, 1965.

[36] Patrick Huerre and Peter Monkewitz. Local and global instabilities in spatially developing flows. 1990.

[37] International Seabed Authority. Clarion Clipperton
Fracture Zone, . URL https://www.isa.org.jm/map/clarion-clipperton-fracture-zone.

[38] International Seabed Authority. Development of geological models for the Clarion-Clipperton Zone polymetallic nodule deposits; ISA Technical Report No.6. *Technical Report No.6*, .

[39] International Seabed Authority. International Seabed Authority ISBA/17/LTC/7 Legal and Technical Commission Environmental Management Plan for the Clarion-Clipperton Zone. Technical report, 2011.

[40] ISA. Proposed Technologies for Deep Seabed Mining of Polymetallic Nodules, 2001.

[41] Thomas Kuhn. RV SONNE SO240 Cruise Report / Fahrtbericht. page 185, 2015. doi: 10.2312/cr{_}so240.

[42] Lisa A. Levin, Kathryn Mengerink, Kristina M. Gjerde,
Ashley A. Rowden, Cindy Lee Van Dover, Malcolm R. Clark, Eva Ramirez-Llodra, Bronwen Currie, Craig R. Smith, Kirk N. Sato, Natalya Gallo, Andrew K. Sweetman, Hannah Lily, Claire W. Armstrong, and Joseph Brider. Defining "serious harm" to the marine environment in the context of deep-seabed mining. *Marine Policy*, 74:245–259, 12 2016. ISSN 0308-597X. doi: 10.1016/J.MARPOL.2016.09.032. URL https://www.sciencedirect.com/science/article/pii/S0308597X1630495X.

[43] Yushun Lian, Haixiao Liu, Solomon C. Yim, Jinhai Zheng, and Pengfei Xu. An investigation on internal damping behavior of fiber rope. *Ocean Engineering*, 182(December 2018):512–526, 2019. ISSN 00298018. doi: 10.1016/j.oceaneng.2019.04.087. URL https://doi.org/10.1016/j.oceaneng.2019.04.087.

[44] William Martin, John Baross, Deborah Kelley, and Michael J.
Russell. Hydrothermal vents and the origin of life. *Nature Reviews Microbiology*, 6(11):805–814, 11 2008. ISSN 1740-1526. doi: 10.1038/nrmicro1991. URL http://www.nature.com/articles/nrmicro1991.

[45] Y Masuda, Ocean Resources, The Pacific, and Michael J Cruickshank.
OTC 8278 Review of Understanding of Continuous Line Bucket System for Deep Seabed Mining. 1997.

[46] Yoshio Masuda, Michael J. Cruickshank,
and John L. Mero. Continuous bucket-line dredging at 12,000 feet. *Proceedings of the Annual Offshore Technology Conference*, 1971-April:837–841, 1971. ISSN 01603663. doi: 10.4043/1410-ms.

[47] J. W. S. McKenna. *Handbook of fibre rope technology*. ISBN 0849325889.

[48] John L. Mero. *The mineral resources of the sea*. Elsevier Pub. Co, 1965. ISBN 9780080870373. URL https://books.google.nl/books?hl=nl&lr=&id=LbTDLa_2opsC&oi=fnd&pg=PP1&ots=ceHRKsKBK1&sig=YkA5uF67ldDqWiy429f4AeX35ZI&redir_esc=y#v=onepage&q&f=false.

[49] Michael W. Lodge. New Interest in Seafloor Mining Revives Calls for Conservation – National Geographic Society Newsroom, 2013. URL https://blog.nationalgeographic.org/2013/12/11/new-interest-in-seafloor-mining-revives-calls-for-conservation-2/.

[50] Dmitry M. Miljutin, Maria A. Miljutina, Pedro Martínez Arbizu, and Joëlle Galéron. Deep-sea nematode assemblage has not recovered 26 years after experimental mining of polymetallic nodules (Clarion-Clipperton Fracture Zone, Tropical Eastern Pacific). *Deep Sea Research Part I: Oceanographic Research Papers*, 58(8):885–897, 8 2011. ISSN 09670637. doi: 10.1016/j.dsr.2011.06.003. URL https://linkinghub.elsevier.com/retrieve/pii/S0967063711001063.

[51] Kathryn A. Miller, Kirsten F. Thompson, Paul Johnston, and David Santillo. An Overview of Seabed Mining Including the Current State of Development, Environmental Impacts, and Knowledge Gaps. *Frontiers in Marine Science*, 4:418, 1 2018. ISSN 2296-7745. doi: 10.3389/fmars.2017.00418. URL http://journal.frontiersin.org/article/10.3389/fmars.2017.00418/full.

[52] Ranadhir Mukhopadhyay and Y. V. Ramana. Acoustic properties of Indian Ocean manganese nodules in relation to physical constitution and chemical composition. *Deep Sea Research Part A, Oceanographic Research Papers*, 1990. ISSN 01980149. doi: 10.1016/0198-0149(90)90131-E.

[53] Ranadhir Mukhopadhyay, Anil K. Ghosh, and Sridhar D. Iyer. Deep-Sea Economy. *The Indian Ocean Nodule Field*, pages 349–367, 2018. doi: 10.1016/b978-0-12-805474-1.00009-9.

[54] John Murray and A F Renard. Report on the deep-sea deposits based on the specimens collected during the voyage of HMS Challenger in the years 1872 to 1876. *EPIC3Bremerhaven, PANGAEA*, 1891.

[55] Nautilus. ENVIRONMENTAL IMPACT STATEMENT.

[56] Marie Navarre and Héloise Lammens. Opportunities of deep-sea mining and esg risks. *Amundi Discussion Papers Series*, 24(August):48, 2017.

[57] Michio Nishioka and Hiroshi Sato. Measurements of velocity distributions in the wake of a circular cylinder at low Reynolds numbers. *Journal of Fluid Mechanics*, 65(1):97–112, 1974. ISSN 14697645. doi: 10.1017/S0022112074001273.

[58] Det Norske Veritas. RECOMMENDED PRACTICE ENVIRONMENTAL CONDITIONS AND ENVIRONMENTAL LOADS. Technical report, 2010. URL http://www.dnv.com.

[59] Det Norske Veritas. RECOMMENDED PRACTICE MODELLING AND ANALYSIS OF MARINE OPERATIONS. Technical report, 2011. URL http://www.dnv.com.

[60] Hirokuni Oda, Yoshio Nakasato, and Akira Usui. Characterization of marine ferromanganese crust from the Pacific using residues of selective chemical leaching: identification of fossil magnetotactic bacteria with FE-SEM and rock magnetic methods. *Earth, Planets and Space*, 70(1):165, 12 2018. ISSN 1880-5981. doi: 10.1186/s40623-018-0924-3. URL https://earth-planets-space.springeropen.com/articles/10.1186/s40623-018-0924-3.

[61] Horst U. Oebius, Hermann J. Becker, Susanne Rolinski, and Jacek A. Jankowski. Parametrization and evaluation of marine environmental impacts produced by deep-sea manganese nodule mining. *Deep-Sea Research Part II: Topical Studies in Oceanography*, 48(17-18):3453–3467, 2001. ISSN 09670645. doi: 10.1016/S0967-0645(01)00052-2.

[62] Joel T Park and Angelo Olivieri. ITTC-Recommended Procedures Fresh Water and Seawater Properties. Technical report.

[63] S. Petersen, A. Krätschell, N. Augustin,
J. Jamieson, J. R. Hein, and M. D. Hannington. News from the seabed – Geological characteristics and resource potential of deep-sea mineral resources. *Marine Policy*, 70:175–187, 2016. ISSN 0308597X. doi: 10.1016/j.marpol.2016.03.012. URL http://dx.doi.org/10.1016/j.marpol.2016.03.012.

[64] Willard J. Pierson and Lionel Moskowitz. A proposed spectral
form for fully developed wind seas based on the similarity theory of S. A. Kitaigorodskii. *Journal of Geophysical Research*, 69(24):5181–5190, 12 1964. ISSN 0148-0227. doi: 10.1029/jz069i024p05181.

[65] Pope Alexander VI. The Bull Inter Caetera. 1493. URL http://rvbeypublications.com/sitebuildercontent/sitebuilderfiles/bullintercaetera.pub.pdf.

[66] T. Prior, D. Giurco, G. Mudd, L. Mason, and J. Behrisch.
Resource depletion, peak minerals and the implications for sustainable resource management. *Global Environmental Change*, 22(3):577–587, 8 2012. ISSN 09593780. doi: 10.1016/j.gloenvcha.2011.08.009.

[67] Eva Ramirez-Llodra, Paul A. Tyler, Maria C. Baker, Odd Aksel Bergstad, Malcolm R. Clark, Elva Escobar, Lisa A. Levin, Lenaick Menot, Ashley A. Rowden, Craig R. Smith, and Cindy L. Van Dover. Man and the Last Great Wilderness: Human Impact on the Deep Sea. *PLoS ONE*, 6(8):e22588, 8 2011. ISSN 1932-6203. doi: 10.1371/journal.pone.0022588. URL https://dx.plos.org/10.1371/journal.pone.0022588.

[68] Joseph L. Reid. On the total geostrophic
circulation of the Pacific Ocean: Flow patterns, tracers, and transports, 1997. ISSN 00796611.

[69] Anatol (National Advisory Committee for Aeronautics)
Roshko. On the development of tubulent wakes from vortex sheets. 1954. ISSN 00177768.

[70] Stephen J Rowe, Brian Mackenzie, and
Richard Snell. Deepwater Installation of Subsea Hardware. *10th Offshore Symposium*, pages 1–9, 2001.

[71] Craig R Smith, Steven Gaines, Les Watling, Alan Friedlander, Charles Morgan, and Andreas Thurnherr. Areas of Particular Environmental Interest. *Workshop - Design Marine Protected Areas for Seamounts and the Abyssal Nodule Province in Pacific High Seas*, 2007. URL https://ran-s3.s3.amazonaws.com/isa.org.jm/s3fs-public/documents/EN/Workshops/2010/Pres/SMITH.pdf.

[72] Robert G Standing, B M T Fluid, Mechanics Limited, Brian Mackenzie, and Offshore Technology. OTC 14180 Enhancing the Technology for Deepwater Installation of Subsea Hardware. 2002.

[73] Virginie Tilot. *Biodiversity and Distribution
ofthe Megafauna, Vol. 69*. 2006. URL https://unesdoc.unesco.org/ark:/48223/pf0000149556.

[74] Rikard Tornqvist, Martin Strande, David Cannell, Peter Gledhill, Paul Smeets, and Justin Gilmore. Deployment of Subsea Equipment: Qualification of Large Diameter Fibre Rope for Deepwater Construction Applications. In *Offshore Technology Conference*. Offshore Technology Conference, 4 2011. ISBN 978-1-61399-117-6. doi: 10.4043/21588-MS. URL http://www.onepetro.org/doi/10.4043/21588-MS.

[75] UN Environment Programme. *Decoupling natural
resource use and environmental impacts from economic growth*. 2011. ISBN 9789280731675. URL http://www.unep.org/resourcepanel/Portals/24102/PDFs/DecouplingENGSummary.pdf%5Cnpapers2://publication/uuid/E74B39E8-2ECE-40EB-B447-C245B77DF785.

[76] United Nations. Agreement relating to the implementation
of Part XI of the United Nations Convention on the Law of the Sea of 10 December 1982. URL https://www.un.org/Depts/los/convention_agreements/convention_overview_part_xi.htm.

[77] M. P. Vlasblom and R. L M Bosman. Predicting the creep lifetime
of HMPE mooring rope applications. *Oceans 2006*, (figure 3), 2006. doi: 10.1109/OCEANS.2006.307013.

[78] Martin Vlasblom. The manufacture, properties,
and applications of high-strength, high-modulus polyethylene fibers. In *Handbook of Properties of Textile and Technical Fibres*. 2018. ISBN 9780081012727. doi: 10.1016/b978-0-08-101272-7.00018-3.

[79] Sam Weller and Exeter Lars Johanning.
Guidance on the use of synthetic fibre ropes for marine energy devices. (September):1–19, 2013.

[80] Frank White. *Fluid mechanics*. 2011. ISBN 9781420091229. doi: 10.2478/jtam-2013-0011.

# List of Figures

# List of Tables